REHVA COMMUNITY OF YOUNG PROFESSIONALS

BOOK OF PAPERS

2023

BRUSSELS, BELGIUM

HVAC WORLD STUDENT COMPETITION 2023

REHVA STUDENT COMPETITION 2023

Our Sponsors

BOOK OF PAPERS
2023

Brussels, Belgium

Table of content

Introduction

The Book of papers is presented by RCYP (REHVA Community of Young Professionals). The RCYP aims to facilitate professional activities and knowledge exchange between young professionals (below 35 years) in the fields of indoor climate, HVAC, building physics, and building services. In the current book, the papers written by the participants of the REHVA Student Competition and the ones from the HVAC World Student Competition are presented. The winners of each competition are also shown at the beginning. At the end of the book, the photos of the events can be found.

REHVA Student Competition

Ever since 2005, REHVA has been organizing a yearly international competition to award the best HVAC students in Europe. REHVA member associations nominate one entry per country to the competition after having organized their national level competitions. The submitted works are based on a Master or Bachelor work and can cover any topic in the fields related to REHVA. The Student competitions are organized during the REHVA Annual Meetings and the Students receive a trophy with their names engraved in it, which is then handed over next year to the next winner. The trophy has been traveling long in the past decade, carrying the names of all the proud winners since 2005.

HVAC World Student Competition

In 2013, REHVA founded a World Student competition with several its international partner associations. Ever since 2016, the HVAC World Student Competition has been taking place between students nominated by REHVA (EU), ASHRAE (United States), CAHVAC (China), FAIAR (South America), ISHRAE (India), SAREK (South Korea) and SHASE (Japan). Each association may send one candidate from their region or continent. REHVA's candidate in the HVAC World Student Competition is the winner from REHVA Student Competition. The other MoU partners organise the HVAC World Student Competition according to the same rules around the world with the participation of REHVA in the jury. The first competition was held in 2016 by REHVA in Denmark. REHVA co-finances the participation of the European candidate in these global competitions

REHVA Student Competitions 2023

REHVA Student Competition 2023 took place in Brussels during REHVA's Annual Meeting on May 11, 2023. This event brought together 11 students from various parts of Europe who gathered in Brussels to showcase their research projects before a distinguished panel of jury members.

Jury members :

The jury team members included Livio Mazzarella (AiCARR-Italy), Maja Todorović (KGH-Serbia), Dejan Mumovic (CIBSE-UK), Francis Allard (AICVF – France), Uwe Schulz (Die Planer – Switzerland), Anatolijs Borodinecs (Latvac – Latvia), Tiberiu Catalina (AIIR – Romania), Adélio Gaspar (Ordem dos Engenheiros – Portugal).

Here is the final result and the subject of their project:

The 1st place and the trophy were awarded to Bas Turk, from The Netherlands, for his work titled "Quantifying the potential of overheating countermeasures on a humanitarian shelter through measurements and building performance simulation."

Lewis Turner secured second place for his paper on "Efficacy of Air Purification to Control Infection in NHS Hospitals," while Miguel Rodríguez Fernández came third with his study on an "Indirect Evaporative Heat Exchanger Prototype Manufactured with 3D Printing." Aurore Toulou won the "best poster" category.

HVAC World Student Competitions 2023

The HVAC World Student Competition 2023 took place online on May 12th, 2023.

The first prize was awarded to Bas Turk (The Netherlands) with his work on the topic "Quantifying the potential of overheating countermeasures on a humanitarian shelter through measurements and building performance simulation."
The next two prizes were awarded to Jingjing Pan (CAHVAC, China) and Indra Permana (ASHRAE, USA), respectively.
The HVAC World Student Competition 2023 was the 4th time that REHVA's representative won the 1st prize.

About RCYP (REHVA Community of Young Professionals)

The RCYP was founded in 2020 by REHVA and coordinated by Arash Rasooli, the first winner of REHVA and HVAC World Student Competition (2016). REHVA seeks the objective of advancing its programs and services for young engineers, helping them build their professional foundations and career. REHVA organises courses for students and young professionals and promotes their participation in the REHVA network event by discounts. REHVA will support the joint activities defined together with the RCYP members and offer advantages relying on the existing REHVA knowledge sources and services, such as free or discounted access to REHVA guidebooks, events and trainings, publication possibility in the REHVA Journal, specific sessions at REHVA events for the community.

The CLIMA World Congresses are inviting young researchers to submit abstracts. If students team-up and purchase REHVA guidebooks, they receive a discount. RCYP is building an online community and information hub tailored to the interest of community members. For any inquiries, feel free to contact us at rcyp@rehva.eu.

Results

REHVA Student Competition 2023
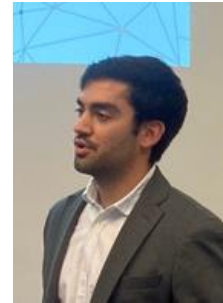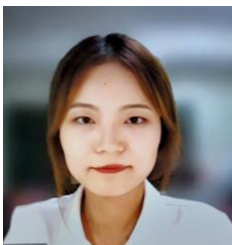

Lewis Turner

Turk Bas

Miguel Rodríguez Fernández

2

1

3

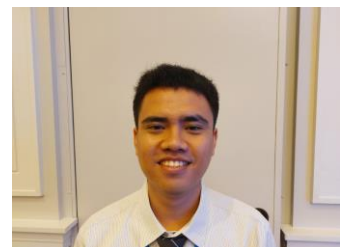## HVAC World Student Competition 2023

Jingjing Pan

Turk Bas

Indra Permana

2

1

3

1st Place
REHVA
Student Competition

Turk Bas
The Netherlands

1st Place
HVAC
World Student Competition

Quantifying the potential of overheating countermeasures on a humanitarian shelter through measurements and building performance simulations

Author: B. (Bas) Turk MSc. ***Year:*** April 2022. ***Institute:*** Eindhoven University of Technology (TU/e) ***Supervisors:*** Prof. J.L.M. (Jan) Hensen (TU/e), Dr. R.C.G.M. (Roel) Loonen (TU/e), T. (Tim) de Haas MSc (Better Shelter)

Abstract — Globally, 82.4 million people are forcibly displaced. Frequently, accommodation is found in shelters designed for short-term occupation, while in practice average stays exceed ten years. Settlements are often located in extremely hot climates in which such shelters tend to overheat. Beyond discomfort, long-term exposure to extreme thermal conditions can result in heat-related illnesses and death. This research aims to 1) quantify the effectiveness of various overheating countermeasures on the Relief Housing Unit (RHU), a temporary shelter produced by Better Shelter, by conducting a case study in a semi-controlled environment, and 2) validate a building performance simulation model of the case study.

Laboratory and field measurements were conducted in the Netherlands on a standard RHU and RHUs with overheating countermeasures. Results show that the indoor thermal climate responds quickly and strongly to solar irradiance, and that reflective envelope coatings and shade nets significantly reduce the amount of overheating in the shelter. On the other hand, darkening the façade's foam color or installing an additional door to promote cross-ventilation did not lead to significant reductions. Fans can best be used to improve the airflow over the occupant's skin, rather than to exhaust warm air.

Additionally, the measurements were used to validate a building performance simulation model of the RHU. This work provides key lessons on modeling solar transmittance through the façade and underlines the importance of model validation and calibration. The model can be used to predict the effectiveness of whole-façade adaptions and modifications to the roof to reduce solar gains, but currently shows low validity to evaluate adaptions that primarily influence the heat flow through the walls or ground. Future work is needed to solve these limitations and assess the robustness of the measurement findings for different locations and hotter climates.

Index Terms — building performance, calibration, heat, humanitarian shelter, measurements, overheating, prototypes, refugee, simulation, thermal

I. INTRODUCTION

Globally, 82.4 million people were forcibly displaced at the end of 2020, of which more than half were children [1], [2]. Although these people often find accommodation in temporary shelters, their average stay exceeds ten years. Shelter settlements often have no access to electricity and are frequently located in extremely hot climates in which the lightweight, leaky and unconditioned structures tend to overheat [3], [4]. Beyond discomfort, long-term exposure to extreme thermal conditions can result in heat-related illnesses and death [5]. Changes in climate and population demographics are likely to increase the occurrences and severity of such problems in the future [6]. It is therefore

important to prevent humanitarian shelters from overheating.

However, a trade-off exists in shelter design between thermal performance, costs, weight, ease of implementation and production, and user-friendliness. Costs are a primary factor, as underfunding is a structural problem in every area of refugee assistance. The funding availability for emergency shelter and Non-Food-Items (NFI) has been less than 30% since 2017 [7]. An increase in weight would generate an increase in transportation costs and a decrease in the refugee's ability to relocate.

A. Status quo of research into overheating in humanitarian shelters

The thermal performance of humanitarian shelters is rarely evaluated and contrary to permanent buildings, no standards are in place that specify thermal requirements or methods to evaluate overheating [8]. Only 15 academic publications before 2018 have studied the thermal performance of humanitarian shelters. The lack of research is mainly caused by the lack of funding [9], while the absence of standards originates from the standpoint of aid organizations who rather help a bit than not at all.[a] More research has focused on cold than hot climates [4], which is exemplified in the development of a winterization kit for a range of tents deployed by the UNHCR, including the Relief Housing Unit (RHU) [10].

Overheating is a problem in a wide variety of humanitarian shelter types, ranging from concrete dwellings to caravans and canvas tents [8], [11]–[13]. Ref. [4], [14] mention a trade-off between ventilation and privacy, security, and dust and sand ingress. The effectiveness of ventilation thus depends on occupant behavior, in contrast to insulation and shading. Thermal mass shows to be an effective solution in climates with a large diurnal temperature variation, but only in combination with insulation or shading [3], [15], [16]. If electricity is available, fans can be used as a means of cooling [14]. Occupants try to stay in outdoor shaded areas as much as possible during the day, as there it is often cooler than indoors [17].

B. Research problem

This research focuses on a case study, the Relief Housing Unit (RHU) version 1.2. The RHU is a temporary shelter produced by the Swedish non-profit Better Shelter and has been deployed since 2015. The shelter shows relevance to the described problem as it has been used on a large scale - 60.000 times in 57 different countries - while thermal comfort is known to be an area for further improvement [18]–[21]. Especially too high temperatures in summer appear to be a problem [22]. Better Shelter is actively looking for overheating countermeasures (OCs) that can be implemented in the design of new shelters or can serve as an add-on to existing shelters. A complete revision of the design is not desired, as interventions should be easy to

---

[a] Personal communication with Corsellis, T., Shelter Centre (July 2020)

implement. Quantitative data would help Better Shelter in their aim to advise partners, once overheating issues are identified. In this regard, building performance simulations look promising as they have the potential to provide such data for many different design options and climates under similar conditions, while circumventing long construction and possibly development times and costs required for real testing.

C. Research goal and scope

This research aims to 1) quantify the effectiveness of various overheating countermeasures on the Relief Housing Unit (RHU) by conducting a case study in a semi-controlled environment, and 2) validate a building performance simulation model of the case study. This research builds on a simulation model from previous work by the same author to quantify the thermal performance of the RHU, hereinafter referred to as research A, [23]. Possible hidden modeling assumptions and uncertainties have a large effect on the simulation results, incentivizing a validation study with measurement data. This creates the need to conduct measurements. Measuring shelters inside a refugee camp is problematic due to financial and ethical constraints. Alternatively, field and laboratory measurements are conducted during summer in the Netherlands to gain insight into the physical aspects of the shelter, such as temperatures and heat flows, and to see whether the model assumptions correspond to reality. The measurements also help to gain insight into the practical implementability of the interventions. The modelling study aims to validate a simulation model of the RHU with the measurement findings and identify the model's strengths and shortcomings, so it can be used to test OCs in future research.

II. Methods

The measurement and simulation studies are structured according to the flowchart in Fig. 1. First, laboratory and field measurements are conducted regarding the solar spectral properties of the façade panels and the infiltration rate of the RHU at the measurement location, respectively. These findings are used to decrease the uncertainty in the model inputs. Second, field measurements are conducted on the thermal environment of the standard shelter, and shelters with interventions. The results of the field measurements are used to quantify and compare the effectiveness of the different design strategies, and to validate the simulation model.
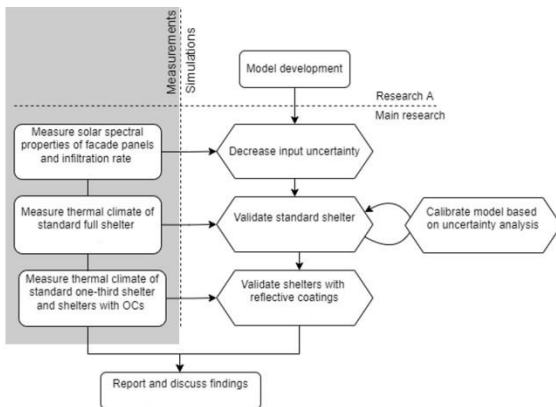

Fig. 1: Flowchart of the research methodology

A. Measurements strategy

Ten different OCs are tested (Fig. 2). 1) and 2) improve the solar reflectance of the envelope using a white-colored paint and aluminum foil coating. 3) and 4) utilize roof shading to decrease the solar gains using a black and aluminum shade net. 5) aims to decrease the solar transmission of the façade panels by using a grey foam color instead of a white one. Besides, the shelter has a beige roof color. 6) aims to reduce the infrared heat radiation from the roof toward the occupied zone with an interior ceiling. 7) and 8) promote cross-ventilation with an exhaust fan and additional door. 9) increases the shelter's thermal mass with a 1000 liter water tank. 10) combines the aluminum foil coating and the aluminum shade net.

Laboratory measurements — The spectral properties of the façade panels and shade nets are measured using a Perkin Elmer UV-VIS-NIR spectrophotometer across the solar spectrum from 350 to 2200 nanometers. Testing samples are used of two by four centimeters. The results are weighted over the solar spectrum using a standard solar spectrum [24] to obtain singular input values for the simulation model. Additionally, the effectiveness of the shade nets is quantified with a shade factor, which is the sum of the solar reflectance and solar absorptance.

Field measurements — From May 19th to August 13th 2021, measurements were conducted on the indoor thermal climate of multiple RHUs at the campus of Eindhoven University of Technology in Eindhoven, the Netherlands. In total, the measurement setup comprises one standard setup of the RHU and four smaller versions of the shelter with one-third of the length. The choice for smaller versions decreases the construction time, required size of the measurement site, and transportation costs. One of the four small shelters is used as a reference case, while the other three are used to compare OCs under similar weather conditions. As not all design variants can be compared at once, they are measured in sequence (table II). All shelters are oriented in the north-south direction with the door on the north side. To prevent that the shelters cast shadows on each other, they are placed four meters apart in the north-south direction and six in the east-west direction.

There is a general agreement that at least four environmental parameters (air temperature, radiant temperature, humidity, and airspeed) and two personal factors (metabolic rate and clothing insulation) are of influence on overheating. The air temperature is the most important predictor of all six [25]. It is measured at 50 and 120 centimeters height in the center of each shelter (Fig. 3). The first height resembles occupants in sitting position, while the latter is the center of gravity of the shelter, used to validate the simulation model. In addition, the mean radiant temperature (MRT) and relative humidity (RH) are measured at 120 centimeters height, also at the center of each shelter. The air velocity is measured in the full shelter only. CO_2 concentration decay tests are conducted to estimate the infiltration rate. Besides, the surface temperatures and heat fluxes of the roof, south wall, and ground are measured in each shelter. The ground temperature is measured below five centimeters of soil, to reduce radiative influences. The measured meteorological parameters are air temperature, RH, wind direction and speed, rain, solar irradiance, and air pressure (Fig. 3). Solar irradiance data is additionally retrieved from the measurement station at the roof of building Vertigo on the TU/e campus, one kilometer from the measurement site.

Fig. 2: In reading direction: Standard full shelter, standard one-third shelter, one-third shelters with black shade net, aluminum shade net, white paint-coated envelope, grey foam panels and beige paint-coated roof, aluminum-coated envelope, and aluminum-coated envelope with aluminum shade net, Exhaust fan applied to vent in the full shelter, Interior ceiling under construction in the full shelter with the exhaust fan in the background, additional door for cross ventilation in the full shelter, water tank for thermal mass in the small shelter

Fig. 3: Left to right; 1. Tripod installed in a small shelter with air temperature and RH sensors and a black globe to measure the MRT at 120 centimeters, and an additional air temperature sensor at 50 centimeters height. 2. Thermistor applied to the center of a roof panel, fixated with iron wire. 3. On-site weather station, 200 centimeter height. Viewing direction to the south. 4. Heat flux plate

All ventilation openings are fully open most of the time to measure the most realistic scenario. All variants are also measured without ventilation to test for the worst-case scenario, as façade openings are frequently blocked for reasons of privacy, security, or (in arid climates;) dust and sand ingress [26]. Warm and dry measurement days are selected to assess each shelter variant. Provided that no big discrepancies are found between the full and one-third shelter, a comparison is made between the one-third shelters with OCs and with the standard buildup.

The combined effect of the environmental parameters of influence on overheating will be evaluated using the Universal Thermal Climate Index (UTCI), as it presents clear stress categories (moderate, strong, very strong) that

can be used to compare design alternatives [27], [28]. Overheating is expressed in Degree-Hours, which is the temperature difference above the 'moderate' heat stress threshold for each hour summed over the measured period [29]. A sensitivity analysis is performed to assess the effect of different performance indicators on the ranking of OCs, including the ASHRAE [30] and Vellei [31] adaptive comfort models, the Wet-Bulb Globe Temperature (WBGT) index for heat stress [32], and wet-bulb temperature limits described by [33].

B. Modelling strategy

The model was developed in DesignBuilder version 6.1, an interface for EnergyPlus 8.9 (Fig. 4). The shelter is modeled as a single thermal zone. The steel frame is not modeled as it is assumed that the thin elements of a conductive material do not significantly influence the thermal resistance or thermal mass of the envelope. It is assumed that the effect of thermal bridges in the façade is trivial to that of the shelter's air permeability. Heat gains from occupancy and plug loads are not considered, corresponding to the measurement setup.

First, the uncalibrated model, with input values based on literature and the laboratory and infiltration rate measurements, is compared to the measurement data. The measured data is down sampled to hourly values and translated to an EnergyPlus Weather (EPW) file to allow a comparison. Second, an uncertainty analysis is performed to aid in understanding how the modeling assumptions, uncertainties, and limitations influence predicted overheating. The scenario without ventilation is considered to limit the input uncertainty. Based on research A, the following influential variables are assessed: i) wind characteristics (infiltration, convection coefficients, and wind exposure), ii) façade properties (solar absorption, thermal emittance, and volumetric heat capacity), and iii) ground modeling. Third, the model's ability to represent the order of magnitude and trend of the physical phenomena of the shelter, most importantly overheating, is improved through calibration to the measurement set. However, model calibration is not the main simulation goal as the (climatic) circumstances differ per location. Fourth, the calibrated model is used to model the reflective coatings and compare the results to the measurement data, as an additional validation step. The coatings are modeled by changing the solar absorptance values of the envelope. As the coatings were measured on the one-third shelters, the model is adjusted accordingly.

III. DATA PRESENTATION

A. Measurements results

Laboratory measurements — The results in table I show that the aluminum-coated panel is most effective at
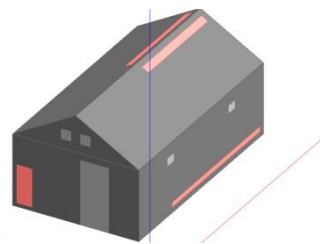

Fig. 4: simulation model of the RHU in DesignBuilder software

reflecting solar radiation, followed by the white paint-coated panel. The absorbing shade nets, with green and black color, provide the highest shade factor. However, the shade factor does not take into account that part of the absorbed heat in the absorbing nets is re-radiated toward the shelter. This decreases their effectiveness. [34] states that reflective nets are more effective than absorbing ones.

Field measurements — The maximum recorded wind speed matches a 'moderate' wind velocity of force 4, while the average wind speed is weak with force 2. Assuming that no major local differences occur on-site, the measurement location can be considered to be sheltered from wind [35]. The CO_2 concentration decay tests resulted in an estimated infiltration rate of 0.8 ACH for the full shelter. The pyranometer positioned inside the unventilated full shelter recorded a maximum irradiance of 40 to 50 W/m². This indicates that around 5% of solar irradiance is directly transmitted through the façade. This is considerably larger than the findings from the laboratory, likely because the full building envelope is more permeable than an individual material sample.

The indoor air temperature in the standard unventilated shelter can reach up to 38ºC at 50 centimeters height, even on days when the outdoor air temperature stays below 26ºC. The Indoor thermal climate of the lightweight shelter responds quickly and strongly to solar irradiance, which is in line with expectations from literature and indicates the potential of measures to reduce the solar heat gains and of additional thermal mass. During the night, the indoor air temperature is near the outdoor air temperature. Natural ventilation can cause a reduction in the indoor air temperature of 5.5ºC. Still, the indoor air temperature in the ventilated standard shelter exceeds 35ºC on the warmest recorded day, when the maximum recorded outdoor air temperature peaked at 31.6ºC. Even when natural ventilation is deployed, the standard shelter on the measurement site can overheat for more than one-third of the day (table II).

The interior surface temperature of the east roof reached up to 49ºC, indicating the potential for roof insulation or a (ventilated) second skin roof. As expected, ventilation only has a small influence on the surface temperatures of sun-exposed façade elements (maximum 5ºC reduction). The measured MRT is very similar to the air temperature, both in dynamics and values, which is typical for lightweight structures. The peak MRT is about 1 to 2ºC lower than the peak air temperature at the same height. Though there is a radiant asymmetry between the cold floor and warm roof, the MRT does not cover this and presents an average value. A maximum vertical temperature gradient of 9.3ºC occurs

over body height (180 centimeters), which can lead to discomfort. Although the heat flux measurements cannot be used as absolute results due to the influence of a large sensor on a thin façade panel, it is clear that decreasing the heat gains through the roof is most important, as these are twice as big as through the south wall and much bigger than through the ground. Contradictory to literature [16], [36]–[38], the ground likely has less influence on the indoor thermal climate. The heat flow through the facade increases after ventilation is deployed, as the temperature difference between the panel and indoor air increases. This indicates that ventilation would not reduce the effectiveness of additional insulation, but would rather improve it. The airspeed in the large shelter only exceeds 0.1m/s on one measurement day.

No large differences were found between the indoor thermal climates of the full and one-third shelter after the ventilation capacity of the latter was decreased by closing half of the vents. This was done to achieve a similar ratio between ventilation openings and building volume for each shelter. Their match is considered good regarding the aim to use the one-third shelter to compare OCs.

The aluminum-coated shelter performed best. However, the white paint-coated shelter and shelters with shade nets perform only slightly worse, especially when ventilation is deployed. All significantly reduce the amount of overheating in the shelter, based on the UTCI. A limitation of the field measurements is that the aluminum and black shade nets could not be tested simultaneously. No clear differences in performance were found, as both nets performed better than the standard shelter and worse than the shelter with aluminum-coated panels. Because hand calculations based on the laboratory measurements indicated that the black shade net would outperform the aluminum-coated shelter, this indicates that the shade factor indeed overestimates the effectiveness of shade nets. The shelter with grey foam and beige roof, and the two measures to promote cross-ventilation did not lead to a significant reduction in overheating. No usable data was

TABLE I.
Measured transmittance (τ), reflectance (ρ), and absorptance (α) values weighted over the solar spectrum

Panels	τ (%)	ρ (%)	α (%)	Shade Factor (%)
Aluminum coating	0.0	87	13	
White paint	1.3	71	28	
Beige paint, grey foam	0.6	44	55	
Beige paint, white foam	1.1	49	50	
Blue paint	0.2	24	76	
Shade nets				
Aluminum	35	54	12	65
Green	20	8	73	80
Black	21	4	75	79

TABLE II.
Comparison of UTCI discomfort hours (above moderate heat stress) in one-third shelters of Setup A (top) and Setup B (bottom). Only data points on which all shelters recorded data have been taken into account.

Setup A Scenario	Over-heating	Standard shelter	Alu coating	Black SN	White coating
Not ventilated June 1–3	Hours [h]	27.2 (-)	23.6 (-13%)	25.8 (-5%)	23.7 (-13%)
	Degree-hours [K·h]	173.5 (-)	71.0 (-59%)	109.8 (-37%)	96.1 (-45%)
Ventilated June 15–17	Hours [h]	28.2 (-)	21.9 (-22%)	23.0 (-18%)	21.9 (-22%)
	Degree-hours [K·h]	118.1 (-)	70.1 (-41%)	81.2 (-31%)	74.7 (-37%)

Setup B Scenario	Over-heating	Standard shelter	Alu coating	Alu SN	GF + BR
Not ventilated July 7–9	Hours [h]	17.8 (-)	8.1 (-54%)	9.5 (-47%)	16.2 (-9%)
	Degree-hours [K·h]	47.2 (-)	6.7 (-86%)	12.4 (-74%)	33.6 (-29%)
Ventilated July 15–17	Hours [h]	15.4 (-)	11.9 (-23%)	13.0 (-16%)	15.9 (-3%)
	Degree-hours [K·h]	39.5 (-)	16.1 (-59%)	20.5 (-48%)	43.9 (+11%)

recorded for the measurement setups with the ventilated roof, thermal mass, and shade net on the aluminum-coated shelter, due to bad weather and a blackout of one week. The choice of performance indicators for overheating does not change the ranking of the tested OCs.

B. Modelling results

The uncalibrated model, based on values found in literature and the laboratory and infiltration rate measurements, likely underestimates overheating with 8.5 Kelvin on the peak UTCI (peak outdoor air temperature of 29°C). An uncertainty analysis is performed to identify possible causes.

First, uncertainty and variability in the local wind characteristics affect the amount of convection and infiltration. Though very strong levels of heat stress are expected for a reference case without infiltration, this is not the case. Furthermore, it is unknown whether the steady convective heat exchange coefficients used in the software – intended for conventional buildings [40] – match the highly fluctuating convection rates on-site. Changing the site's wind exposure does not affect the convective heat transfer coefficient and U-value of the wall elements, while this should be expected [41]. Moreover, the coefficients for the walls are higher than for the roof, where it is expected that the roof has higher coefficients due to elevated wind speeds. The peak heat flow through the south wall predicted by the uncalibrated model is half as big as the measured value, which suggests that the coefficients for the walls are too high.

Second, the measured solar absorptance values in the laboratory may differ from the values on the measurement site or in a refugee camp due to the deposition of sand and dust. A 10%-point uncertainty range is applied to the measured values. Because solar radiation is the main cause of overheating, uncertainty in the solar absorptance of the panels has a considerable influence on predicted overheating, as shown in the uncertainty ranges in Fig. 5.

Third, in correspondence to literature, changes to the ground model have a big impact on the modeled overheating. However, the measured heat flow through the ground is relatively small, with a maximum of roughly 40W/m². This matches with the expectation of reality, where the massive ground slab has little influence on the thermal climate of the lightweight structure.

Fourth, the effect of thermal emissivity and volumetric heat capacity on overheating is relatively small. Because the façade panels are very light and thin a large change in the capacity has little effect on the thermal mass. The thermal conductivity of the panels is known from ref. [42]. As the modeled external surface temperatures by the uncalibrated model are lower than the measured internal surface temperatures, the underestimation of overheating seems to be related to convective or radiative heat exchange in the outside surface heat balance rather than conduction through the panels.

Model adjustments are done based on the uncertainty analysis, including, i) decreasing the convective heat losses from the exterior façade by changing the site's wind exposure from 'normal' to 'sheltered'. The convection coefficients are not adjusted manually as this would result in fixed - and therefore likely unrealistic - values. ii) increasing the shortwave radiative heat absorptance of the exterior façade by 10 %-point, and iii) decreasing the heat

exchange with the ground by choosing the least conductive settings for the soil properties. Based on the measurement findings, the solar transmittance of the façade is incorporated in the model by strips of fully transparent glazing that cover 5% of the exterior surface area (Fig. 4). Modelling the shelter as fully glazed, as recommended by Ref. [36], is not preferred as the software assumes that glass layers are thin enough to neglect heat storage and the conductivity of glass is high enough to assume a layer is isothermal [43].

The calibrated model is used to model the reflective coatings. The differences between the modeled standard one-third and full shelter are considered acceptable, where the full shelter is 0.5 Kelvin warmer on the UTCI in the afternoon of the hottest measured day. In line with the calibration steps, the solar absorption is set 10%-point higher than the values obtained from the laboratory measurements.

Fig. 5 shows the predicted and measured overheating in the standard shelter, and effect of the reflective coatings on overheating. The uncertainty range of the aluminum coating is bigger than that of the white paint coating due to additional uncertainty of the thermal emissivity. As the coatings target the heat flow through the façade, the comparison with the measured surface temperatures of the east roof and south wall is deemed most important. This match is regarded as good given the anticipated measurement and modeling uncertainty.

Some limitations of the simulation model are identified. First, the model is not able to capture fast fluctuations in the indoor thermal climate due to changeable weather. Second, the perfectly-mixed air assumption causes an overprediction of the ground surface temperature and the effect of the reflective façade coatings on this temperature, the MRT, and UTCI. This highlights a design challenge for future research to model thermal stratification in the shelter. Third, the calibrated model predicts that the heat flow through the south wall is only directed inwards for a short period of the day, which does not match the measured trend. These findings strengthen earlier indications that the model overpredicts the convection rate from the shelter's walls on the measurement site. Fourth, modeling the solar transmittance of the façade increases the heat gains through the façade by roughly 50%. However, the effect on predicted overheating is smaller than expected (from 32 to 34°C on UTCI). Fifth, the 10%-point increase in the modeled solar absorption values is motivated by uncertainty from the deposition of sand and dust on the façade. The increase leads to a sufficient match with the measurements for all modeled shelters. However, sand and dust would likely have a larger effect on the performance of the shelters with reflective coatings. In addition, the field measurements did not show a decline over time in the performance of the aluminum-coated shelter in comparison to the standard shelter. This suggests that the increased solar absorption values are compensating e.g., the overprediction in convection or modeling simplifications.

IV. Discussion

The results from the field measurements are in line with the laboratory findings, although the mutual differences in performance are smaller on-site due to i) ventilation, ii) possible sedimentation of sand and dust on the panels, and iii) the fact that performance is more complex than comparing material properties. Both the match between
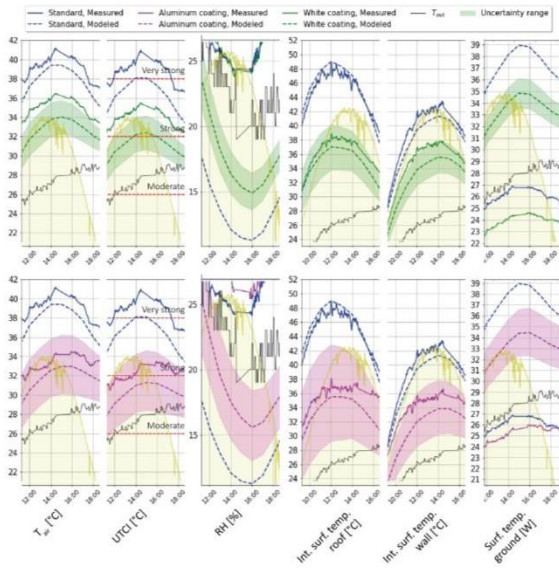
Fig. 5: Comparison of modeled and measured effect of reflective coatings on overheating in the RHU, June 2nd.

the predicted and measured overheating in the standard shelter and the effect of the reflective coatings is evaluated as good given the anticipated measurement and modeling uncertainty. Presenting the results as uncertainty ranges is useful in case the model will be applied to new contexts. Moreover, the measurement data cannot be considered the ultimate truth.

The shelter's thermal performance is part of a trade-off with costs, weight, ease of production and implementation, and user-friendliness. First, the aluminum-coated shelter had a slightly better measured thermal performance on-site than the white paint-coated shelter. However, the latter is easier to implement in the production process as the aluminum coating leads to imperfections in the panel when it is heated in a press mould and notably deteriorated on site when in contact with ground moisture. The white coating is easier to implement as an add-on to existing shelters and does not lead to an increase in production costs of new shelters. A downside of the tested coatings is their design flexibility. Removable coatings deserve attention in further research.

In this light, the tested shade nets do provide this flexibility and can be applied to both new and existing shelters. The nets can also be used to create shaded courtyards, improve privacy, or in colder periods, serve as blankets or protect the shelter from wind. A downside is a large increase in production costs of roughly 25% and the added weight of the structural frame, leading to an increase in transportation costs. A downside of both the reflective coatings and shade nets is that they change the external appearance of the shelter. Ref. [15] mentions that the camp authorities of Azraq refugee camp in Jordan did not allow this, mainly due to security concerns.

The measured airspeed is too low to have a significant effect on thermal comfort [39] [30]. This might be a problem specifically for the measurement location as it appeared to be sheltered from wind, but the situation may be worse in a densely populated refugee camp. This indicates the potential of fans, which can best be used to improve the airflow over the occupant's skin, rather than to exhaust hot air.

exhaust hot air. The heat gains of the standard shelter have to be reduced significantly before the limited capacity of exhaust fans will have a considerable effect on the indoor air temperature. However, measures to promote ventilation can also have a positive effect on poor air quality, which results in approximately 20,000 displaced people dying prematurely every year [26].

It is important to note that the findings from the field measurements only hold for the specific climatic conditions on site. Future research can use building performance simulations to assess the robustness of the measurement results for more extreme climates. Additionally, translating the level and duration of overheating into the risk of health effects can give substantiation for the necessity of OCs in light of the described trade-offs. At the moment, no indicator for overheating is perfectly applicable in the humanitarian sector. Applicability issues are identified for the thermal comfort models, as prevailing mean outdoor temperatures above 33.5°C are not covered by ASHRAE Standard 55 [30]. Empirical research to develop new performance indicators, for example through questionnaires in refugee camps, is suggested for future work.

V. CONCLUSIONS

Field measurements in the Netherlands on the ventilated standard shelter showed that the indoor air temperature far exceeds outdoor values on a warm sunny day. The Indoor thermal climate responds quickly and strongly to solar irradiance, indicating the potential of additional thermal mass and measures to reduce the solar heat gains. Decreasing the gains through the roof is most important. Contradictory to earlier studies, the ground has less influence on the indoor thermal climate. Thermal stratification remains a point for further improvement when ventilation is deployed. Roughly 5% of solar radiation is directly transmitted through the unventilated shelter, of which the majority through cracks and holes. These results are in line with the findings of a literature review, which found that measures to avoid solar gains should be favored above passive and active cooling principles.

Different design options were tested on their ability to reduce overheating in the RHU. Both laboratory and field measurements indicate that an aluminum-coated shelter performs best. However, a white paint-coated shelter and shelters with shade nets perform only slightly worse, especially when ventilation is deployed. All significantly reduce the amount of overheating in the RHU, based on the Vellei adaptive thermal comfort model. The sensitivity of these findings to the choice of performance indicators for overheating is low. On the other hand, darkening the panel's foam color or installing an additional door to promote cross-ventilation did not reduce overheating. Fans can best be used to improve the airflow over the occupant's skin, rather than to exhaust hot air.

It is important to note that these conclusions only hold for the specific climatic conditions on the measurement site. Future work using building performance simulations is required to test the robustness of the findings for different locations and climates. This work underlines the importance of model validation and calibration and provides key lessons on modeling solar transmittance through the façade. The validated simulation model from this research can be used to predict the effectiveness of whole-façade adaptions and adaptions to the roof to reduce

6

solar gains. Due to the limitations identified, the model shows low validity to test adaptions that primarily influence the heat flow through the walls or ground. In addition, the validity of the model predictions regarding measures that promote evaporative cooling or ventilative cooling is uncertain as the validation study has focused on the unventilated shelter. Future research can solve these limitations by conducting measurements to validate the modeled convection coefficients and a higher-resolution ventilation model required to simulate thermal stratification. The sensitivity of the findings to the choice of performance indicators should be re-evaluated when tests are conducted for more extreme climates or measures based on evaporative cooling or ventilative cooling.

Based on the research findings, Better Shelter will likely implement the tested white paint coating in the production process of shelters to deploy in year-round hot climates.

BIBLIOGRAPHY

[1] UNHCR, 'Global Trends - Forced displacement in 2020', 2021. https://www.unhcr.org/flagship-reports/globaltrends/ (accessed Apr. 18, 2022).

2 UNHCR, 'Resettlement at a glance (January-December 2019)', 2020.

3 D. Fosas, D. Albadra, S. Natarajan, and D. Coley, 'Overheating and health risks in refugee shelters: Assessment and relative importance of design parameters', Proceedings of 33rd PLEA International Conference: Design to Thrive, PLEA 2017, vol. 3, pp. 3746–3753, 2017.

4 D. Albadra, D. Coley, and J. Hart, 'RIBA president's awards for research 2017 winner of the annual theme - Housing: Toward healthy housing for the displaced', Journal of Architecture, vol. 23, no. 1, pp. 115–136, 2018, doi: 10.1080/13602365.2018.1424227.

5 M. Lee, L. Shi, A. Zanobetti, and J. D. Schwartz, 'Study on the association between ambient temperature and mortality using spatially resolved exposure data', Environ Res, vol. 151, pp. 610–617, 2016, doi: 10.1016/j.envres.2016.08.029.

6 N. Watts et al., 'The 2019 report of The Lancet Countdown on health and climate change: ensuring that the health of a child born today is not defined by a changing climate', Lancet Publishing Group, Nov. 2019. doi: 10.1016/S0140-6736(19)32596-6.

7 UN OCHA United Nations Office for the Coordination of Humanitarian Affairs, 'Funding progress by sector| Financial Tracking Service', 2022. https://fts.unocha.org/appeals/overview/2022 (accessed Apr. 17, 2022).

[8] S. Tuladhar, J. Jahn, and H. Samuelson, 'Tempering The Temporary: Improving Thermal Comfort and Human Well-being in Relief Shelters', Proceedings of Building Simulation 2019: 16th Conference of IBPSA, vol. 16, no. September, pp. 547–554, 2020, doi: 10.26868/25222708.2019.211323.

[9] P. Manfield, 'Emergency Shelter for Humanitarian Relief in Cold Climates : Policy and Praxis', 2001.

10 UNHCR, Shelter Design Catalogue. 2016.

11 D. Borge-Diez, A. Colmenar-Santos, C. Pérez-Molina, and M. Castro-Gil, 'Passive climatization using a cool roof and natural ventilation for internally displaced persons in hot climates: Case study for Haiti', Build Environ, vol. 59, pp. 116–126, 2013, doi: 10.1016/j.buildenv.2012.08.013.

12 S. Attia, 'Assessing the thermal performance of bedouin tents in hot climates', 1st International Conference on Energy and Indoor Environment for Hot Climates, no. Losleben 2003, pp. 328–335, 2014.

13 C. Cornaro, D. Sapori, F. Bucci, M. Pierro, and C. Giammanco, 'Thermal performance analysis of an emergency shelter using dynamic building simulation', Energy Build, vol. 88, pp. 122–134, 2015, doi: 10.1016/j.enbuild.2014.11.055.

14 S. Y. Saleh and M. Gadi, 'An Investigation into Thermal Comfort of Shelters in Refugee Camps in Palestine Using Questionnaires and Computer Simulation', IUG Journal of Natural and Engineering Studies, vol. 20, no. 2, pp. 127–152, 2012.

15 D. Fosas, D. Albadra, S. Natarajan, and D. A. Coley, 'Refugee housing through cyclic design', Archit Sci Rev, vol. 61, no. 5, pp. 327–337, 2018, doi: 10.1080/00038628.2018.1502155.

16 D. Fosas, F. Moran, S. Natarajan, J. Orr, and D. Coley, 'The importance of thermal modelling and prototyping in shelter design', Building Research and Information, vol. 48, no. 4, pp. 379–400, 2019, doi: 10.1080/09613218.2019.1691489.

17 D. Albadra, M. Vellei, D. Coley, and J. Hart, 'Thermal comfort in desert refugee camps: An interdisciplinary approach', Build Environ, vol. 124, pp. 460–477, 2017, doi: 10.1016/j.buildenv.2017.08.016.

18 bettershelter.org, 'About Us : Better Shelter'. https://bettershelter.org/about/ (accessed Dec. 08, 2020).

[19] Engineering For Change, 'Better Shelter'. https://www.engineeringforchange.org/solutions/product/better-shelter/ (accessed Oct. 23, 2020).

20 Better Shelter, 'Year in review 2019', 2019.

21 The Housing Innovation Collaborative, 'Better Shelter RHU 1.2 // Live Home Tour - The Rapid Shelter Innovation Showcase', youtube.com, 2020. https://www.youtube.com/watch?v=wx7lh6uMO2Y&ab_channel=TheHousingInnovationCollaborative (accessed Oct. 15, 2021).

22 T. de Haas, 'Better Shelter Thermal Comfort - Progress Update June 2021'. 2021.

23 B. Turk, 'Thermal comfort and heat stress in a humanitarian shelter: a simulation study', 2021.

24 PVEducation, 'Standard Solar Spectra: ASTM G-173-03 (International standard ISO 9845-1, 1992)'. https://www.pveducation.org/pvcdrom/appendices/standard-solar-spectra (accessed Nov. 26, 2021).

25 Y. Epstein and D. S. Moran, 'Thermal comfort and the heat stress indices', Ind Health, vol. 44, no. 3, pp. 388–398, 2006, doi: 10.2486/indhealth.44.388.

26 D. Albadra et al., 'Measurement and analysis of air quality in temporary shelters on three continents', Build Environ, vol. 185, no. June, p. 107259, 2020, doi: 10.1016/j.buildenv.2020.107259.

27 F. R. d'Ambrosio Alfano, B. I. Palella, and G. Riccio, 'Universal Thermal Climate Index (UTCI): a Challenge for the Thermal Environment Assessment', 2011.

28 K. Blazejczyk, Y. Epstein, G. Jendritzky, H. Staiger, and B. Tinz, 'Comparison of UTCI to selected thermal indices', Int J Biometeorol, vol. 56, no. 3, pp. 515–535, 2012, doi: 10.1007/s00484-011-0453-2.

29 C. Di Napoli, F. Pappenberger, and H. L. Cloke, 'Verification of heat stress thresholds for a health-based heat-wave definition', J Appl Meteorol Climatol, vol. 58, no. 6, pp. 1177–1194, 2019, doi: 10.1175/JAMC-D-18-0246.1.

30 ASHRAE, 'ANSI/ASHRAE Standard 55-2017: Thermal environmental conditions for human occupancy', 2017.

31 M. Vellei, M. Herrera, D. Fosas, and S. Natarajan, 'The influence of relative humidity on adaptive thermal comfort', Build Environ, vol. 124, pp. 171–185, 2017, doi: 10.1016/j.buildenv.2017.08.005.

32 International Organization for Standardization, 'ISO 7243:2017 - Ergonomics of the thermal environment — Assessment of heat stress using the WBGT (wet bulb globe temperature) index', 2017. Accessed: Nov. 13, 2020. [Online]. Available: https://www.iso.org/standard/67188.html

33   C. Raymond, T. Matthews, and R. M. Horton, 'The emergence of heat and humidity too severe for human tolerance', Sci Adv, vol. 6, no. 19, 2020, doi: 10.1126/sciadv.aaw1838.

34   Svensson R&D, 'Technical Reflective Shade Screen', pp. 0–2, 2015.

[35] KNMI, 'Beaufort wind scale'. https://www.knmi.nl/kennis-en-datacentrum/uitleg/windschaal-van-beaufort (accessed Jan. 12, 2022).

[36] S. Obyn, G. Van Moeseke, and V. Virgo, 'Thermal performance of shelter modelling: Improvement of temporary structures', Energy Build, vol. 89, no. December 2018, pp. 170–182, 2015, doi: 10.1016/j.enbuild.2014.12.035.

37   R. Pöschl, 'Modelling the Thermal Comfort Performance of Tents used in Humanitarian Relief', 2016.

38   A. Rijs, 'Development of a software tool for decision-making on HVAC systems' capacity for military tents', 2020.

39   F. Nicol, 'Adaptive thermal comfort standards in the hot-humid tropics', Energy Build, vol. 36, no. 7, pp. 628–637, 2004, doi: 10.1016/j.enbuild.2004.01.016.

40   M. Mirsadeghi, D. Cóstola, B. Blocken, and J. L. M. Hensen, 'Review of external convective heat transfer coefficient models in building energy simulation programs: Implementation and uncertainty', Appl Therm Eng, vol. 56, no. 1–2, pp. 134–151, 2013, doi: 10.1016/j.applthermaleng.2013.03.003.

[41] DesignBuilder Software Ltd, 'Site Details'. https://designbuilder.co.uk/helpv4.6/Content/_Site_details.htm (accessed Apr. 13, 2022).

42   RISE Research Institutes of Sweden AB, 'Determination of thermal resistance of Better Shelter RHU AB Virgin Wall, Dubai Wall, Virgin Roof, Dubai Roof'. 2017.

43   U.S. Department of Energy, 'EnergyPlusTM Version 8.9.0 Documentation, Engineering Reference, chapter 19.1 Radiant System Models'. pp. 1300–1333, 2018.

2nd Place
HVAC World
Student Competition

**Jingjing Pan
China**

Investigation on physiological responses, thermal perceptions and comfort zone with indoor solar radiation in the summer

Jingjing Pan, College of Civil Engineering, Hunan University, Changsha, 410081, China, pjj1208@hnu.edu.cn
Nianping Li*, College of Civil Engineering, Hunan University, Changsha, 410081, China, linianping@126.com
Based on a Master thesis of 2023

Abstract—**Indoor solar radiation significantly affects human thermal sensation, especially with the extensive use of glass structures in modern buildings. This study explored the varying characteristics of human physiological and psychological responses to indoor solar radiation in the summer, based on a laboratory experiment involving 20 participants and six cases comprising different intensity levels and irradiation areas. In this experiment, the thermal sensation and acceptability were recorded, and environmental and physiological parameters such as local skin temperature, arterial oxygen saturation (SpO$_2$) and pulse rate (PR) were continuously monitored. The results revealed that human physiological regulation is generally delayed, as compared with the psychological changes in unstable environments. This paper proposes a method for calculating the mean skin temperature, representing the skin temperature on the irradiated side by that on the nonirradiated side. The skin temperature calculated using this method reflected the strongest correlation with thermal sensation; this helped reduce the prediction errors in thermal sensation due to psychological factors, when considering skin temperature as a predictor. Furthermore, this study used the standard effective temperature (SET) to calculate acceptable temperature ranges and a neutral SET. It was found that the upper limit of acceptable temperature was 1.77 ℃ higher than that recommended in ISO 7730, indicating humans' enhanced acceptance ability to air temperatures under indoor solar radiation. Notably, the results of this study constitute a significant theoretical basis for improving thermal comfort under indoor solar radiation in the summer.**

Index Terms—**Solar radiation, Mean skin temperature, Thermal sensation, Acceptable temperature range, SET.**

1. Introduction

Glass structures such as glass curtain walls, skylights, and floor-to-ceiling windows, which are increasingly used in modern buildings, meet architectural aesthetics and daylighting requirements; however, they also introduce large amounts of solar radiation indoors (mainly visible light and near-infrared radiation (NIR), accounting for 45% and 50% of the energy emitted, respectively [1]). In such buildings, human thermal comfort is significantly affected by indoor solar radiation: occupants close to windows might be overheated by solar radiation and the equivalent operative temperature increase can be higher than 5℃ that exceeds the compensation capacity of HVAC systems [2]. The variability in sunlit areas considerably creates nonuniform thermal environments for indoor occupants. When the set-point of HVAC systems are changed to maintain comfort of occupants exposed to solar radiation, the adjacent spaces without strong solar radiation are likely to be overcooled [3]. Moreover, the

solar radiation incident upon occupants can trigger physiological response changes (skin temperature, arterial oxygen saturation, sweating, etc.) that significantly affect people's comfort, health, and work performance and directly impacts human thermal sensation (approximately 1.5-scale rise of TSV) [4, 5].

Thus far, many researchers have considered the impact of solar radiation on indoor thermal environments. Gennusa et al. [6, 7] proposed a calculation method for the mean radiant temperature (MRT), considering the direct and diffused components of solar radiation; this approach can be utilized to improve the estimation of human heat balance at any point in a room. Marino et al. [8, 9] suggested a detailed method for calculating the indoor radiation asymmetry under solar radiation, in order to evaluate the local thermal discomfort over time and space. Based on the SC and DC models, He et al. [2] established a new mathematical model for simulating indoor irradiation on the body that was capable of rapid annual computations of the increase in the MRT at specific sites. Although the aforementioned studies improved the accuracy of thermal sensation analyses under indoor solar radiation, they lacked discussion about the physiological and psychological changes caused by irradiation on the body.

Many studies have also considered both solar radiation and human physiological parameters. Guan et al. [10] combined physiological characteristics with subjective responses to develop a dynamic human thermal comfort model applied for highly transient conditions in automobiles, which improved the prediction accuracy of the overall and local thermal sensations. Hodder et al. [1] determined the quantitative relationship between human skin temperature and thermal sensation by exposing the front glass of a car to simulated solar radiation with varying intensities. Ohnaka et al. [11] compared the sensitivities of different parts of the human body to solar radiation by irradiating the head and torso in the sitting position, under various simulated solar radiation intensities. Liu et al. [4] studied the effects of indoor solar radiation on the local skin temperature through thermal comfort experiments conducted in the winter. It was found that solar radiation can significantly affect human thermal sensation, which gradually increases with the irradiation area. Nevertheless, previous research has rarely explored the thermal comfort under solar radiation in the summer. This is likely because, in the summer, the increase in thermal sensation due to solar radiation is not conducive to thermal comfort, unlike that in the winter. However, the physiological and psychological responses induced by unstable solar radiation may influence human thermal acceptance. Therefore, it is also necessary to investigate

human thermal comfort under indoor solar radiation in the summer.

With the rapid development of wearable and non-invasive technologies, the application of physiological responses to reflect human thermal comfort has recently become prevalent. Scholars generally consider parameters such as the skin temperature [12, 13], arterial oxygen saturation (SpO_2) [12, 14], blood pressure [12, 15], heart rate [14], and pulse rate (PR) [12]. Choi et al. [16] measured the skin temperature at seven selected parts of the human body and built a decision tree model; the highest accuracy of individual thermal sensation predictions was achieved when adopting a combination of the arm, back, and wrist temperatures as the input. Liu et al. [17] verified the viability of skin temperature in assessing human thermal sensation under high temperature conditions and found that using the wrist skin temperature as the input could improve the prediction accuracy by up to 93 % for the proposed models. Existing studies [12-18] have indicated the reliability of these physiological parameters in correlating human thermal sensation under a uniform indoor environment; this, however, needs to be further investigated under more specific non-uniform environments (such as indoor solar radiation environments).

As human thermal comfort in an environment is comprehensively affected by several factors [19], including the metabolic rate, clothing insulation, air temperature, mean radiant temperature (MRT), relative humidity, and air velocity, a variety of indices have been proposed for the evaluation of human thermal comfort. For instance, the standard effective temperature (SET) is based on the two-node human physiological model proposed by Gagge [20], which is an equivalent temperature that integrates the six factors mentioned above with human basic thermoregulation and can help predict some physiological indicators such as the mean skin temperature and skin moisture. The SET index has been shown to feature a favorable correlation with thermal sensation at low metabolic rates [21-23], and it also widely applicable in dynamic environments [24-26]. For calculating the acceptable or comfort temperature zone, many studies [19, 21, 27, 28] have adopted the approach of first determining the SET zone and then calculating the temperature zone based on the average parameter values under specific conditions. Nonetheless, the application of the SET in an indoor solar radiation environment may differ, owing to the strong impact of solar radiation on human physiological responses. Therefore, it is necessary to validate the viability of the SET before applying it under indoor solar radiation environments.

In summary, existing research has primarily focused on the indoor thermal environment under solar radiation, or the rational use of indoor solar radiation to improve human thermal comfort in the winter; however, thus far, limited efforts have been devoted toward investigating the human physiological and psychological responses triggered by indoor solar radiation in the summer. In this study, the varying characteristics of human physiological and psychological responses with respect to indoor solar radiation were investigated, relying on an experiment combining environmental parameters, physiological parameters, and subjective questionnaires in the summer. The acceptable temperature ranges and neutral SET under indoor solar radiation were calculated after verifying the applicability of the SET, in order to further investigate the influence of indoor solar radiation on the human acceptance ability in the summer. The findings of this study are expected to facilitate suggestions aimed at improving human thermal comfort and building energy efficiency under indoor solar radiation in the summer.

2. Methods

A preliminary experiment was also conducted in the chamber in advance, considering the radiation blocking of the surrounding trees, which revealed that direct radiation entered the room at approximately 8:00 a.m. The experiment was carried out from 8:05 to 10:35 a.m., a duration wherein the solar radiation was relatively stable. The experimental phase and interval were determined based on sun position movement. The following six cases were studied in accordance with the differences in the irradiation area and solar radiation intensity: whole body irradiated with low-intensity solar radiation (< 100 W/m^2) (case 1), whole body irradiated with high-intensity solar radiation (> 100 W/m^2) (case 2), whole body except head irradiated with high solar radiation (case 3), upper body irradiated with high solar radiation (case 4), lower body irradiated with high solar radiation (case 5), and no parts of the body irradiated (case 6). The upper body includes the forehead, chest, upper arm, and wrist, whereas the lower body includes the thigh, calf, and ankle.

At 7:50 a.m., the subjects entered the adaptation phase and completed the basic information questionnaire; 15 min later, subjects #1/2 and #3/4 exchanged positions, at intervals of 15 min, with a subjective questionnaire completion at the end of each 15-min period. At the beginning of the experimental period (8:05 a.m. to 8:35 a.m.), cases 1 and 2 were created to explore the influence of solar radiation with varying intensity (above or below 100W/m^2) on the human body. As the solar altitude was
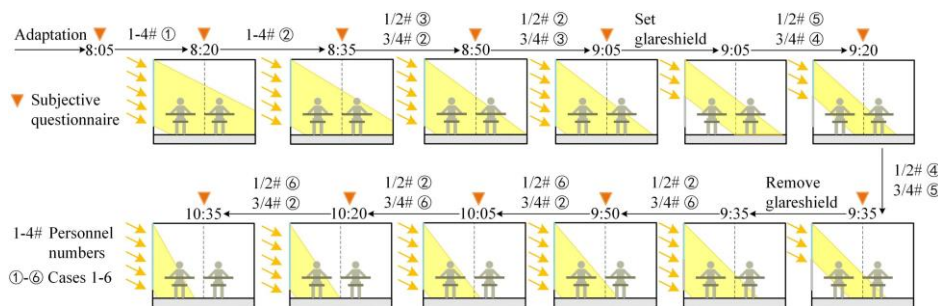

Figure 1. Experimental procedure.

getting higher, cases 2 and 3 were designed in the half-hour that followed, exploring how irradiation on the head affects the human body. To achieve cases 4 and 5 with irradiation only on the upper body or lower body, respectively, a glareshield was placed on the window at 9:05 a.m. and removed at 9:35 a.m. In the rest of the period, cases 2 and 6 were designed to investigate the psychological responses between irradiated and nonirradiated conditions. The specific time periods and corresponding irradiation cases are shown in Fig. 1, and the average solar radiation intensity during the measurement periods (8:05 a.m. to 10.35 a.m.) of experimental days (Sep.15th to Sep.19th) for each case is listed in Table 1.

Table 1. Solar radiation intensity for each case.

case	case 1	case 2	case 3	case 4	case 5	case 6
Solar radiation (W/m^2)	47.39	269.14	257.89	270.20	216.25	22.05

3. Data Presentation and Discussion

3.1 Thermal sensation and irradiation areas

To intuitively quantify the effect of solar radiation on human thermal sensation, the corresponding local and overall thermal sensation changes for each irradiation case were plotted as presented in Fig. 2, where the thermal sensation vote values of each part represent the average of all subjects. As shown in Fig. 2, case 4 entailed the highest thermal sensation for all parts of the body, followed by cases 2 and 3, respectively; the thermal sensation in these three cases clearly deviated from the human comfort range (-0.5 to +0.5). In case 5 as well, there were certain parts with thermal sensations beyond the comfort range. Furthermore, the thermal sensations of each part of the body under cases 1 and 6 were low and within the comfort range.

A comparative analysis of the local thermal sensations among the cases was performed. The thermal sensation in the upper body for case 4 was 0.3－0.4 scale higher than that for case 2. A likely explanation is that case 2 included conditions with lower solar altitudes in this experiment, resulting in a wider range of solar radiation intensity; although the average solar radiation intensity in case 2 was nearly identical to that in case 4. Furthermore, in case 2, compared with that in case 3, the thermal sensation of the forehead was 0.95 scale higher; the thermal sensations of all the other parts of the body were also higher. Thus, as the irradiation on the head reduces, the thermal sensations of local body parts also exhibit a decreasing trend, which is more pronounced on the upper body (>0.5 scale lower) than on the lower body (0.1－0.3 scale lower). Comparing case 2 with case 5, the thermal sensation of the upper and lower body reflected a difference of 1.1 － 1.3 and 0.6 － 1.0, respectively, in terms of the scale considered. This indicates that a reduction in irradiation on the upper body is correlated with the cool sensations of other parts, especially the thigh (0.98 scale lower). The difference in thermal sensation between cases 5 and 6 was not significant for the upper body (0.15 scale) and approximately 0.4 scale for the lower body, suggesting that the influence of irradiation on the lower body on the other parts is not substantial and can be neglected. The above comparisons suggest that the irradiation-induced (>

100 W/m^2) sensation changes on one part alter the perception of the other body parts; when compared with the upper body, reducing irradiation on the lower body has a lower likelihood of perceiving cool sensation on other parts. A similar phenomenon was also observed in the study of He et al. [29] where the subjects felt that in cool environments, the unheated body parts felt warm when local heating stimuli were applied to only a few body parts. Based on a comparison of cases 1 and 6, direct solar radiation below 100 W/m^2 has no significant effect on human thermal sensation, which implies that the corresponding fluctuations in thermal sensation will not exceed the human comfort range.
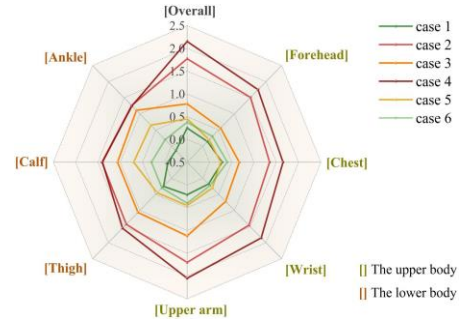

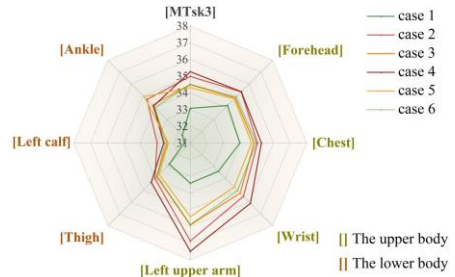Figure 2. Local and overall thermal sensation of human body in irradiation cases.

Figure 3. Skin temperatures of human body in irradiation cases.

3.2 Irradiation areas and skin temperature

According to the measurement results, considering the skin temperature difference influenced by irradiation between two sides of the same segment according to the above measurement results, four calculation methods for the mean skin temperature were discussed, based on the existing four-point (4b) method (right upper arm, left chest, anterior thigh, and anterior calf) as shown in Table 2. Here, the left point represents the irradiated side, whereas the right point represents the side without irradiation.

Table 2. Calculation methods for mean skin temperature.

	Chest	Upper arm (Left)	Upper arm (Right)	Thigh	Calf (Left)	Calf (Right)
MTsk1-4b	√		√	√	√	
MTsk2	√		√	√		√
MTsk3	√	√		√	√	
MTsk4	√	√√		√		√√

√√: The average of both sides' measured values.

	MTsk1-4b	MTsk2	MTsk3	MTsk4
Spearman ρ	0.452**	0.474**	0.548**	0.532**

The correlation coefficients between the mean skin temperature values calculated using the four methods and the overall thermal sensation are shown in Table 3; it is evident that MTsk3 shows the highest correlation with thermal sensation, followed by MTsk4. Both methods consider the skin temperature of the irradiated side, indicating that it is appropriate to consider the irradiated side for all computations referring to the mean skin temperature under indoor solar radiation. Thus, MTsk3 was used for all subsequent analyses involving the mean skin temperature.

To intuitively quantify the effect of solar radiation on the skin temperature, changes in the corresponding local and mean skin temperatures for each irradiation case were plotted as presented in Fig. 3, where the skin temperatures of each part denote the average for all subjects. The figure indicates that the irradiated segments of the upper limb (wrist and upper arm) retained the highest skin temperatures in all cases, with substantial fluctuations across the cases. Compared to the upper body, the lower body was not significantly affected by the cases, which corroborates the statement in Section 3.1 that the lower body is relatively insensitive to solar radiation.

Comparing Figs. 2 and 3, the thermal sensations in cases 1 and 6 are similar and both within the comfort range for both cases; however, the corresponding skin temperature differs considerably, with a maximum difference of 2.49 ℃ (left arm) and a minimum difference of 0.72 ℃ (forehead). A probable explanation is that case 1 was set in the early stages of the experiment when the subjects entered the area with lower solar radiation after the adaptation phase. By contrast, case 6 was set in the later stages of the experiment, when the subjects entered the area without solar radiation after experiencing solar irradiation for a period of time; consequently, the skin temperature decreased but did not return that in the absence of irradiation experience in the short term. This phenomenon of similar thermal sensation but significant differences in skin temperature suggests that the skin temperature values are not always fully representative of the thermal sensation variations; it also indicates that human physiological regulation is commonly delayed, as compared to psychological changes, in unstable environments. Considering the instability and instantaneity of solar radiation, when the skin temperature is used as a predictor, the psychological influences may lead to thermal sensation prediction errors under indoor solar radiation.

3.3 Improvement in mean skin temperature calculations

As discussed in Section 3.2, the calculation of the mean skin temperature under indoor solar radiation must adopt the values of the irradiated side, mainly for parts that have two sides and are generally exposed, such as limbs. Therefore, the upper arm and calf were selected for analyses as typical parts of the upper and lower limbs, respectively. There is a strong correlation between the skin temperatures of the two sides (0.520** for the upper arm and 0.745** for the calf). Considering the more

complicated measurements and the delayed physiological regulation, as compared with psychological changes, the skin temperature of the irradiated side is proposed to be represented by that of the nonirradiated side.

The measured data were classified into two conditions based on the cases: irradiated (> 100 W/m^2) and nonirradiated (including radiation < 100W/m^2). The multiplicative connection (coefficient $a_1=1.1$ for the upper body and $a_2 =1.04$ for the lower body) between the skin temperatures of both sides was calculated under the irradiated condition; for the nonirradiated condition, the skin temperatures on both sides were taken directly considered equal. For the new calculation method (MTsk*) for the mean skin temperature, the skin temperature of the limbs was determined under the abovementioned two conditions, while the rest of the body remained unchanged. The formula in this study is adopted as an example, which is based on the four-point (4b) method, given by Eq. (1) and (2). With the measured values of the nonirradiated side being substituted into the formulas to obtain the MTsk* values, the correlation between MTsk* and the overall thermal sensation was found to be 0.624**, which is considerably higher than that for MTsk3.

According to the results in Section 3.2, it can be surmised that, in an unstable environment, physiological and psychological responses may bit be synchronized, resulting in inconsistencies between the physiological characteristics and thermal sensation. When entering a non-irradiated area from an irradiated area, for example, the skin temperature on the irradiated side does not decrease immediately but the thermal sensation does. Owing to its disregard for the thermoregulation lag, this new calculation method could achieve a greater correlation with thermal sensation and, to a certain extent, mitigate the prediction errors in thermal sensation caused by psychological factors (when using the skin temperature as a predictor).

Calculation formula for the solar irradiated condition:

$$MTsk^* = 0.3T_{chest} + 0.3 \cdot a_1 \cdot T_{upper\ arm} + 0.2T_{thigh} + 0.2 \cdot a_2 \cdot T_{calf} \quad (1)$$

Calculation formula for the non-irradiated condition:

$$MTsk^* = 0.3T_{chest} + 0.3T_{upper\ arm} + 0.2T_{thigh} + 0.2T_{calf} \quad (2)$$

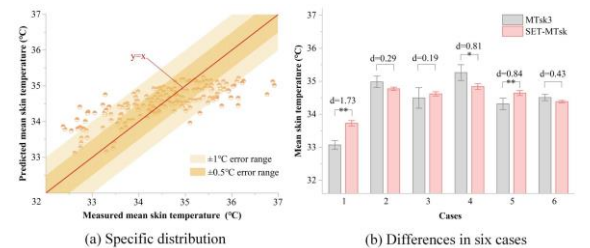(a) Specific distribution   (b) Differences in six cases

Figure 4. Comparison of predicted and measured mean skin temperatures.

3.4 Applicability of SET under indoor solar radiation

Based on the data predicted by the two-node model in the SET, a variance analysis of the predicted and measured values (MTsk3) of mean skin temperature was conducted, indicating that the overall data were not significantly different. Fig. 4(a) depicts the specific distribution, demonstrating that the prediction of mean

skin temperature from the two-node model has an accuracy of 50.3 % when the error range is ±0.5 °C, and up to 82.7 % when the error range is ±1 °C. One of the likely explanations for the errors is that the 15-min intervals in this experiment cannot ensure the subjects have reached a fully steady state, which implies their physiological parameters might still be fluctuating. As an intermediate indicator for calculating the SET within the two-node model, the mean skin temperature within 20 % error under ±1 °C accuracy can ensure that the SET is certainly correlated with human physiological responses, thus achieving a certain degree of applicability in the indoor solar radiation environment.

A further comparison of the predicted and measured values of the mean skin temperature in different cases is shown in Fig. 4(b), and it can be seen that the differences are mainly reflected in cases 1, 4, and 5. The differences in case 1 indicate that the effect of low-intensity solar radiation on human skin temperature is overestimated in the two-node model, and the differences in cases 4 and 5, which are both cases of solar irradiation on parts of the body, indicate that the two-node model overestimates the effect of solar irradiation on the lower body skin temperatures and underestimates the effect of solar irradiation on the upper body skin temperatures. The results suggest that further investigation of the prediction accuracy of the thermal sensation in the SET under indoor solar radiation is merited.

3.5 Thermal acceptable range under indoor solar radiation

To explicitly discuss the human acceptance of a single factor of air temperature in an indoor solar radiation environment, the percentage of thermal acceptability was divided into two kinds of overall environment and air temperature. Table 4 presents a regression model using the disordered multiclass logistic regression [19, 34, 35] calculations, both of which are statistically significant. The ASHRAE 55 standard [36] defines an acceptable thermal environment as one which a substantial majority (more than 80%) of occupants find it thermally acceptable. Therefore, in this study, the percentage of thermal acceptability was required to be above 80%, as indicated by the dotted line in Fig. 5. The solid red line in Fig. 5 represents the model of the logistic regression. The percentage of thermal acceptability is calculated as the ratio of the data with a thermal acceptable value of +0.01 and +1 to all the data, as represented by the yellow histogram, which is nonuniform due to the fact that the environmental parameters were actually monitored but not precisely designed during the experiment.

The upper limit of the overall environmental acceptable SET is 26.19 °C, which is 1.62 °C lower than the acceptable SET for air temperature. Thus, it has been discovered that the ability of the human body to accept air temperatures is significantly improved under indoor solar radiation, such that satisfying thermal comfort requirements by simply lowering the indoor temperature under this specific environment will lead to inefficient and high energy consumption.

Based on the calculated upper acceptable SET and average parameter values (metabolic rate = 1 met, clothing insulation = 0.49 clo, relative humidity = 47.71%, and air velocity = 0.11 m/s), the upper acceptable temperature was determined, as shown in Table 4. To compare our

calculation results with the standards in the case of office buildings located in hot summer and cold winter regions, the class C range (-0.7 ≤ PMV ≤ +0.7) in ISO 7730 [37] was selected to obtain an upper acceptable temperature of 27 ℃. Based on Table 4, the upper acceptable temperatures (both for the overall environment and simply air temperature) are beyond the standard by varying degrees. It is, thus, suggested that, for hot summer and cold winter regions, the acceptable air temperature threshold in the existing standard can be relaxed under indoor solar radiation in the summer.

Table 4. Logistic regression equations for percentage of thermal acceptability and SET.

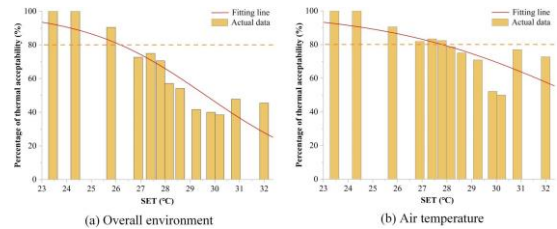|	Equation	Upper acceptable SET (℃)	Upper acceptable air temperature (℃)
Overall environment	$Y = \dfrac{1}{1+e^{0.1018SET-11.9862}+e^{-2.2984SET-0.}}$	26.19	27.24
Air temperature	$Y = \dfrac{1}{1+e^{0.2575SET-8.5705}+e^{-1.0556SET-0.}}$	27.81	28.77

Figure 5. Logistic regression results of the percentage of thermal acceptability and SET.

4. Conclusions

This study investigated the changes in human physiological and psychological responses under indoor solar irradiation through a summer experiment combining environmental parameters, physiological parameters, and subjective questionnaires, and calculated the acceptable and neutral intervals using the SET index. Specifically, this work aimed to further investigate the effects of solar radiation on human thermal acceptability. The main findings of this study can be summarized as follows.

(1) Irradiation-induced (> 100 W/m^2) sensation changes on one site correlate with the perception of other body sites. When compared with the upper body, reducing irradiation on the lower body has a lower likelihood of perceiving cool sensation on other parts. The thermal sensation fluctuation triggered by solar irradiation below 100W/m^2 will not exceed the human comfort range.

(2) Human physiological regulation is commonly delayed, as compared with psychological changes in unstable environments (such as under solar irradiation). Accordingly, this work formulated a new calculation method for the mean skin temperature, which represents the skin temperature of the irradiated side by that of the nonirradiated side, to mitigate the prediction errors in thermal sensation caused by psychological factors (i.e., when using skin temperature as the predictor).

23

(4) To a certain extent, the SET can reflect human thermal sensation variations and physiological responses under indoor solar radiation. Predictions of the mean skin temperature based on the two-node model entail an accuracy of up to 82.7%, when the error range is ±1 °C, with specific differences mainly appearing in the cases of low-intensity solar radiation or direct solar radiation incident on the upper and lower body alone.

(5) Compared with the normal indoor environment, the upper acceptable SET for air temperature is 1.62 °C higher than that for the overall environment; this indicates that the human acceptance ability to air temperature is significantly improved under indoor solar radiation and also that simply lowering the indoor temperature in this specific environment to satisfy thermal comfort requirements will result in inefficient and high energy consumption.

References

1   S.G. Hodder, K. Parsons, The effects of solar radiation on thermal comfort, Int J Biometeorol, 51(3) (2007) 233-50.

2   Y. He, E. Arens, N. Li, Z. Wang, H. Zhang, Y. A, C. Yuan, Modeling solar radiation on a human body indoors by a novel mathematical model, Building and Environment, 187 (2021).

3   E. Arens, T. Hoyt, X. Zhou, L. Huang, H. Zhang, S. Schiavon, Modeling the comfort effects of short-wave solar radiation indoors, Building and Environment, 88 (2015) 3-9.

4   G. Liu, Z. Wang, C. Li, S. Hu, X. Chen, P. Liang, Heat exchange character and thermal comfort of young people in the building with solar radiation in winter, Building and Environment, 179 (2020).

5   H. Zhang, R. Yang, S. You, W. Zheng, X. Zheng, T. Ye, The CPMV index for evaluating indoor thermal comfort in buildings with solar radiation, Building and Environment, 134 (2018) 1-9.

6   M.L. Gennusa, A. Nucara, G. Rizzo, G. Scaccianoce, The calculation of the mean radiant temperature of a subject exposed to the solar radiation—a generalised algorithm, Building & Environment, 40(3) (2005) 367-375.

7   M. La Gennusa, A. Nucara, M. Pietrafesa, G. Rizzo, A model for managing and evaluating solar radiation for indoor thermal comfort, Solar Energy, 81(5) (2007) 594-606.

8   C. Marino, A. Nucara, M. Pietrafesa, Mapping of the indoor comfort conditions considering the effect of solar radiation, Solar Energy, 113 (2015) 63-77.

9   C. Marino, A. Nucara, M. Pietrafesa, Thermal comfort in indoor environment: Effect of the solar radiation on the radiant temperature asymmetry, Solar Energy, 144 (2017) 295-309.

10 Y.D. Guan, M.H. Hosni, B.W. Jones, T.P. Gielda, Investigation of human thermal comfort under highly transient conditions for automotive applications - Part 2: Thermal sensation modeling, Ashrae Transactions, 109 (2003) 898-907.

11 T. Ohnaka, S. Hodder, K. Parsons, The effects of simulated solar radiation to the head and trunk on the thermal comfort of seated subjects, Elsevier Ergonomics Book, 3 (2005) 305-311.

12 Chaudhuri, Tanaya, Zhai, Deqing, Soh, Yeng, Chai, Li, Hua, Xie, Random forest based thermal comfort prediction from gender-specific physiological parameters using wearable sensing technology, Energy & Buildings, (2018).

13 J.H. Choi, V. Loftness, Investigation of human body skin temperatures as a bio-signal to indicate overall thermal sensations, Building & Environment, 58(DEC.) (2012) 258-269.

14 Y. Jiang, N. Li, A. Yongga, W. Yan, Short-term effects of natural view and daylight from windows on thermal perception, health, and energy-saving potential, Building and Environment, 208 (2022).

15 I. Gilani, M.H. Khan, M. Ali, Revisiting Fanger's thermal comfort model using mean blood pressure as a bio-marker: An experimental investigation, Applied Thermal Engineering, (2016).

16 J.-H. Choi, D. Yeom, Study of data-driven thermal sensation prediction model as a function of local body skin temperatures in a built environment, Building and Environment, 121 (2017) 130-147.

17 W. Liu, X. Tian, D. Yang, Y. Deng, Evaluation of individual thermal sensation at raised indoor temperatures based on skin temperature, Building and Environment, 188 (2021).

18 C. Bulcao, S.M. Frank, S.N. Raja, K.M. Tran, D.S. Goldstein, Relative contribution of core and skin temperatures to thermal comfort in humans, Journal of Thermal Biology, 25(1-2) (2016) 147-150.

19 H. Du, Z. Lian, D. Lai, W. Liu, L. Duanmu, Y. Zhai, B. Cao, Y. Zhang, X. Zhou, Z. Wang, X. Zhang, Method of determining acceptable air temperature thresholds in Chinese HVAC buildings based on a data-driven model, Energy and Buildings, 241 (2021).

20 A.P. Gagge, A.P. Fobelets, L.G. Berglund, A standard predictive index of human response to the thermal environment, Ashrae Trans, 92 (1986) 709-731.

21 H. Du, C. Yang, Re-visitation of the thermal environment evaluation index standard effective temperature (SET*) based on the two-node model, Sustainable Cities and Society, 53(2) (2019) 101899.

22 B. Li, C. Du, M. Tan, H. Liu, E. Essah, R. Yao, A modified method of evaluating the impact of air humidity on human acceptable air temperatures in hot-humid environments, Energy and Buildings, 158(PT.1) (2018) 393-405.

23 M.L. Zhu, Q. Ouyang, H.G. Shen, Y.X. Zhu, Field study on the objective evaluation of sleep quality and sleeping thermal environment in summer, Energy and Buildings, 133 (2016) 843-852.

24 S. Zhang, Z. Lin, Standard effective temperature based adaptive-rational thermal comfort model, Applied Energy, 264 (2020).

25 Z. Fang, X. Feng, J. Liu, Z. Lin, C.M. Mak, J. Niu, K.T. Tse, X. Xu, Investigation into the differences among several outdoor thermal comfort indices against field survey in subtropics, Sustainable Cities and Society, 44 (2019) 676-690.

26 Z. Yu, B. Yang, N. Zhu, T. Olofsson, G. Zhang, Utility of cooling overshoot for energy efficient thermal comfort in temporarily occupied space, Building & Environment, 109(nov.) (2016) 199-207.

27 W. Ji, Y. Zhu, B. Cao, Development of the Predicted Thermal Sensation (PTS) model using the ASHRAE Global Thermal Comfort Database, Energy and Buildings, 211 (2020).

28 Z. Zhang, Y. Zhang, A. Khan, Thermal comfort of people from two types of air-conditioned buildings - Evidences from chamber experiments, Building and Environment, 162 (2019).

29 Y. He, T. Parkinson, E. Arens, H. Zhang, N. Li, J. Peng, J. Elson, C. Maranville, Creating alliesthesia in cool environments using personal comfort systems, Building and Environment, 209 (2022).

30 Y. He, N. Li, W. Zhang, J. Peng, Overall and local thermal sensation & comfort in air-conditioned dormitory with hot-humid climate, Building and Environment, 101 (2016) 102-109.

31 Y. He, N. Li, Q. Huang, A field study on thermal environment and occupant local thermal sensation in offices with cooling ceiling in Zhuhai, China, Energy and Buildings, 102 (2015) 277-283.

32 ASHRAE, Standard 55-2013-Thermal Environmental Conditions for Human Occupancy, American Society of Heating, Refrigerating and Air-Conditioning Engineers, Inc., Atlanta, 2013.

33 J. Huang, Human and Thermal Environment, Beijing: Science Press, China, 2011.

34 D. Lai, C. Chen, Comparison of the linear regression, multinomial logit, and ordered probability models for predicting the distribution of thermal sensation, Energy & Buildings, 188-189(APR.) (2019) 269-277.

35 R. Thapa, H.B. Rijal, M. Shukuya, Field study on acceptable indoor temperature in temporary shelters built in Nepal after massive earthquake 2015, Building and Environment, 135 (2018) 330-343.

36 ASHRAE, Standard 55-2017-Thermal Environment Conditions for Human Occupancy, American Society of Heating, Refrigerating and Air-Conditioning Engineers, Inc., Atlanta, 2017.

37 ISO, ISO 7730: Ergonomics of the thermal environment - Analytical determination and interpretation of thermal comfort using calculation of the PMV and PPD indices and local thermal comfort criteria, International Standards Organization, Genève, 2005.

2ⁿᵈ Place
REHVA
Student Competition

Lewis Turner
UK

Efficacy of Air Purification to Control Infection in NHS Hospitals

Lewis Turner

Abstract— **Healthcare Associated Infections (HAI) are among the major complications of receiving modern medical treatment. Mechanically assisted ventilation is seen as an important factor to reduce HAI within NHS hospitals. However, because of aging hospital buildings common ventilation practices such as mechanical ventilation and natural ventilation cannot be utilised, thus, there is a growing emphasis on the utilisation of simple ventilation systems such as air purification. This study seeks to identify if air purification is a suitable solution by benchmarking against current ventilation systems using computational fluid dynamics and infection risk modelling. This study identified that air purifiers have a higher performance than that of natural ventilation and should be utilised in hospitals where natural ventilation isn't available. However, air purifiers cannot perform to the level of standard mechanical ventilation, thus, should not be used as an alternative.**

Index Terms—**COVID-19, Air purification, CFD, Healthcare infections.**

Introduction

The COVID-19 pandemic exposed numerous issues in ventilation within the National Health Service (NHS) hospitals. Despite otherwise good infection control practices multiple hospitals noticed ongoing transmissions and outbreaks of COVID-19. Authors suggest that this occurred due to a lack of fresh air ventilation to dilute and remove pathogens. Many NHS hospital buildings were built to older health building standards, and are, therefore, poorly ventilated [1]. Most aged hospital buildings were designed using the Nightingale ward principles which emphasised natural ventilation. Due to changes in safety, and thermal energy regulations, natural ventilation has been phased out in most wards and as a result of the original construction new mechanical ventilation is not feasible [7]. Therefore, there is a need for innovative ventilation technologies that can be implemented simply into poorly ventilated areas. A solution discussed predominantly since the COVID-19 pandemic is air purification/cleaning devices, as they provide a localised and decentralised solution to provide ventilation without the need for large ventilation plant and distribution systems. This study investigated these technologies further to assess their performance against currently used ventilation systems.

I. Methodology

A. Research Approach

The study investigated the performance of air purification systems to reduce infection by benchmarking air purifiers against currently utilised ventilation techniques (mechanical ventilation, natural ventilation) within an NHS hospital ward scenario. To achieve this approach, the study developed an experimental scenario representing a typical two bed ward bay. The study utilised a two-stage approach to investigate and analyse the difference in performance. In stage A the risk of infection is modelled, then in stage B the pathogen and air flow characteristics are studied through computational fluid dynamics (CFD) simulations. This enables the identification of performance to reduce infection risk, and the concentration of airborne pathogens.

B. Experimental Scenario

The experimental scenario is representative of a typical hospital bay consisting of 2 patient beds. This bay has an area of $31.9m^2$ and a volume of $87.73m^3$. Two windows (1.25 x 1.50m) are present for natural ventilation. The bay has a ceiling based mechanical ventilation system. The hospital room includes no equipment other than beds. Within this experimental zone, there are 4 male persons. Person 1 shall be assumed to be infected with a respiratory virus and symptomatic. Person 1 exhibits typical symptoms of respiratory illnesses such as coughing thus shall generate infectious quanta. Persons 2,3, and 4 are not infected with a respiratory illness and thus are susceptible to infection from Person 1.
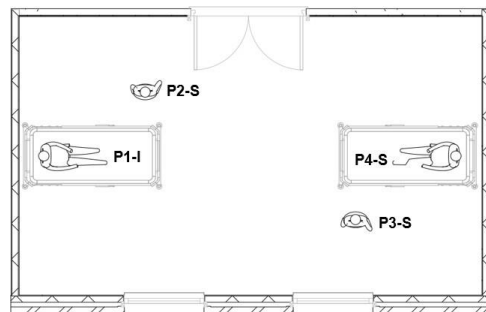

Figure 1. Plan View of Experimental Hospital Zone and occupants.

C. Ventilation Systems Outline

Two air purifiers shall be studied, one air purifier will represent a "healthcare grade" system, and the second air purifier will represent a "domestic" system. These systems were developed through a process of sampling. The healthcare air purifier shall be a "side in - top out" flow rate of 520 m^3/h and maximum aerosol efficiency of healthcare-focused air purifier (AP-H) with a maximum 99.728%. The domestic air purifier shall be a "cylindrical" domestic-focused air purifier (AP-D) device with a maximum flow rate of 190 m^3/h and maximum aerosol efficiency of 99.82%. Air purifiers will be located to the right of Person 1 on the floor.
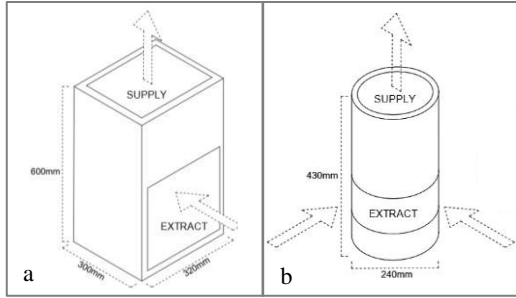
Figure 2. (a): AP-H, (b): AP-D

The described air purifiers shall be benchmarked against the following mechanical and natural ventilation systems (See Figure 3). The mechanical ventilation system has two ceiling inlets and outlets. This system provides balanced ventilation at a 6 air changes per hours (ACH) achieving a volume flow rate of 528m3/h with each outlet/inlet providing 264m3/h of air exchange. This mechanical ventilation system is designed to the health regulation frameworks, therefore, can be taken as the standard for performance within healthcare ventilation. Natural ventilation shall be provided through the openable windows. Given the average wind speeds and window opening, this study predicts an average fresh air flow rate
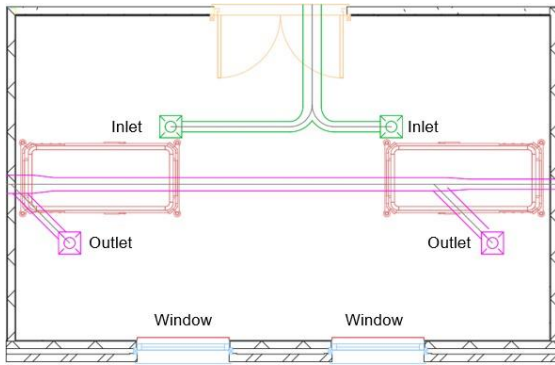
of 185m3/h.

Figure 3. Mechanical and Natural Ventilation Systems

D. Stage A: Infection risk mathematical modelling

In this stage, the study shall utilise a derivative of the original Wells-Riley model developed by Gammaitoni and Nucci [3]. This model is used to calculate the probability of susceptible people catching an infection when in the same ventilated space as infectious people [9]. This derivate model incorporates mixing factors to account for incomplete mixing of air. This will enable the study to model the potential risk of infection whilst utilising air purification devices and natural and mechanical ventilation.

$$P_{INFECTION} = 1-e^{(\frac{Iqp}{V} * \frac{Ct+e^{(-Ct)}-1}{C^2})} \qquad (1)$$

In (1): $P_{infection}$ = the infection probability, p = pulmonary ventilation rate of a person (m³/hr), q = quanta generation rate (1/hr), t = exposure time (hr), C = equivalent ventilation rate (1/hr), V = volume of the space (m³).

$$C = \frac{Q}{K} * \frac{\eta_{filter}}{V} \qquad (2)$$

The equivalent ventilation rate (C) is the ventilation rate incorporating a mixing factor to the account for incomplete mixing of air. In (2): Q = the ventilation rate (m³/h), K = the mixing factor, η_{filter} = the filtration efficiency, V = the room volume. For the air purification devices, this study has assumed a value of 2 for K. For the natural ventilation this study has assumed a value of 2.5 for K. For the mechanical ventilation system this study has assumed a value of 1.5 for K

To accurately study the infection control efficacy of each ventilation type, various infectious diseases shall be studied. Thus, various values for q in (1) are identified as per Table 1:

TABLE I. QUANTA GENERATION RATES

Infectious Disease	Quanta Generation	Citation
Rhinovirus	3.1 / hr	[11]
Tuberculosis	8.2 / hr	[4]
SARS	28.94 / hr	[6], [10]
Influenza	76.18 / hr	[6], [3]
Measles	124 / hr	[11], [3]

E. Stage B: Computational Fluid Dynamics

Computational Fluid Dynamics (CFD) is the process of simulating fluid flow and solving it numerically. CFD will be used in this study to simulate cough particulates travelling through air, and how they interact with the ventilation systems. CFD software will be used in the form of Ansys Fluent 2020 R1 Academic. The CFD model is set out as follows. Person 1 shall cough 3.13e-8kg of COVID-19 infected aerosol into the zone within a period of 0.5s. Person 1 is sitting up in bed and thus the cough shall be released 90º to their face with a velocity of 10m/s. The mouth of person 1 is positioned 590mm above the bed with an opening surface area of 4cm². Cough particulate shall be injected into the zone with a randomised diameter between 2.5 µm to 200 µm and shall consist of liquid water. Within these CFD simulations, the study shall analyse three scenarios: utilisation of AP-D, utilisation of AP-H, and the utilisation of the mechanical ventilation system. It should be noted that natural ventilation cannot be simulated given the chaotic nature of the airflow.
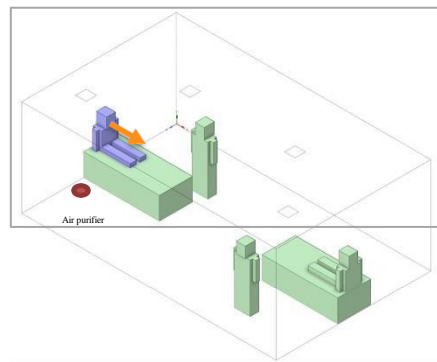

Figure 4. Model Geometry in Ansys Fluent

TABLE II. CFD BOUNDARY CONDITIONS

Boundary condition	Value
Simulation model	K-ε model
K-ε model Type	Standard
Near wall treatment	Standard wall functions
Acceleration due to gravity	-9.81m/s2

II. STAGE A: INFECTION RISK MODELLING

The study utilised (1) and (2) to identify the number of infected individuals after a 4-hour contact period. As around 85% of visits to emergency departments are under 4 hours this result set shall enable the study to accurately estimate the number of subsequently infected patients under typical circumstances [8].

A. Infection Risk Modelling Results
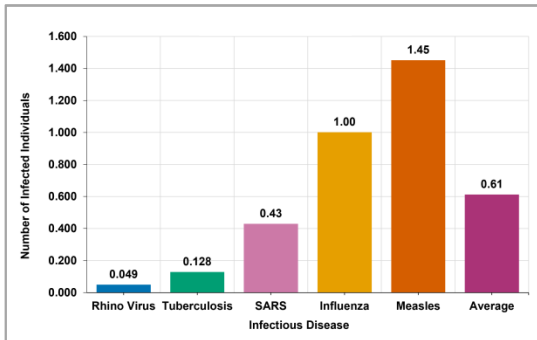
Figure 5.   Infected persons after 4 hours under mechanical ventilation
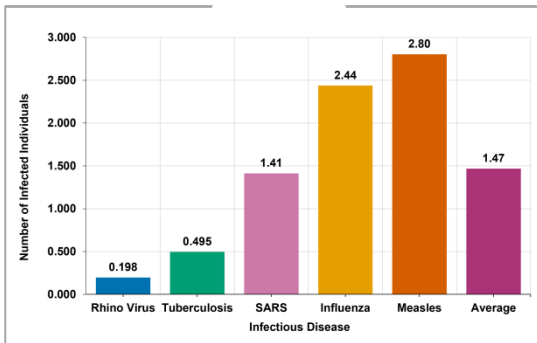
Figure 6. Infected persons after 4 hours under natural ventilation
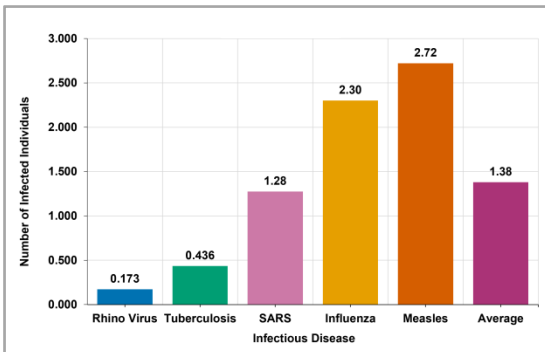
Figure 7. Infected persons after 4 hours under AP-D ventilation
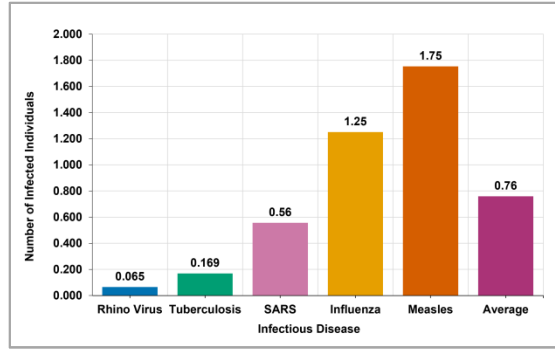
Figure 8. Infected persons after 4 hours under AP-H ventilation

B. Infection Risk Modelling Results Discussion

The results indicate similarities in the performance of AP-D and natural ventilation with a performance differential of 10.7% in favour of AP-D. This similarity indicates AP-D type devices can perform to a similar if not higher level to that of natural ventilation to reducing infection risk. AP-D and natural ventilation have a comparable flow rate but, have different mixing factors of 2 and 2.5 respectively. The mixing factor has a significant impact on performance as it defines how well the fresh dilutes the pathogen. The mixing factor is higher for natural ventilation due to unpredictable natural airflow currents that cause ineffective mixing. For AP-D on the other hand, the fresh airflow is forced into the zone at a constant level and can mix with the internal air more effectively. This enables AP-D to outperform natural ventilation.

The results also indicate AP-H and AP-D fail to meet the standard of mechanical ventilation. AP-H and AP-D are seemingly limited by mixing factor and flowrate. In terms of mixing factor, the air purifiers have a higher mixing factor of 2 than that mechanical ventilation 1.5. Air purifiers have a higher mixing factor as single outlet air systems are less effective at mixing air throughout a zone. Through extrapolation of the data, the study identified that the higher mixing factor results in a 29% higher infection probability for air purifiers. AP-D and AP-H have a lower volume flow rate (190m3/h and 520m3/h respectively) than that of mechanical ventilation (528m3/h). Thus, the lowest flow rates cause the air purifiers not to meet healthcare standards. The failure to fresh air standards contributes to the poor performance of the air purifiers to control infection <1 for the pathogens. Thus, the air purifiers do not meet the performance of the mechanical ventilation system.

The discussion indicates that both AP-D and AP-H dilute pathogens with greater performance than natural ventilation but fail to meet the performance of mechanical ventilation. This indicates that air purifiers could replace natural ventilation for dilution of pathogens. However, air purifiers cannot be utilised in place of mechanical ventilation, as the performance differential is too great.

III. COMPUTATIONAL FLUID DYNAMICS STUDY

The study shall use the CFD model to generate three sets of data. The first set of results is the mass in the domain over time representing the ability of each ventilation system to reduce the particulate concentration. The second result set presents the escaped mass, which represents the quantity of infectious particulate leaving the zone through the ventilation outlets. The third set of results presents the penetration distance over time, which represents the distance of the furthest travelling particle normal to the point of injection. Throughout these results, each ventilation system shall be compared to identify the performance differential.

A. Mass in domain results

Figure 9 presents the mass of cough droplets in the domain over time for AP-H, AP-D, and mechanical ventilation. This indicates the time to reduce mass in domain to 5% (1.565e-9kg) per ventilation system.
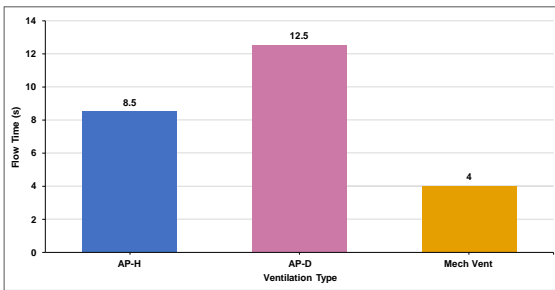
Figure 9. Time to reduce mass in domain to 5% per ventilation system

The results indicate, mechanical ventilation has the highest performance, AP-H has the median performance, and AP-D has the lowest performance. Therefore, the air purifiers do not meet the performance of mechanical ventilation for particulate reduction. The performance of the air purifiers does however present some efficacy for infection control as they reduce the particulate mass to 0kg in <13 seconds.

B. Escaped mass results

Escaped mass is defined as particulate mass that exits the zone through ventilation outlets. Total escaped mass values for each system are presented in Figure 10. From the results, mechanical ventilation sees the highest escaped mass of (4.38e-9kg), AP-H sees the median escaped mass (3.13e-09kg) and AP-D sees the lowest escaped mass (2.5e-9kg).
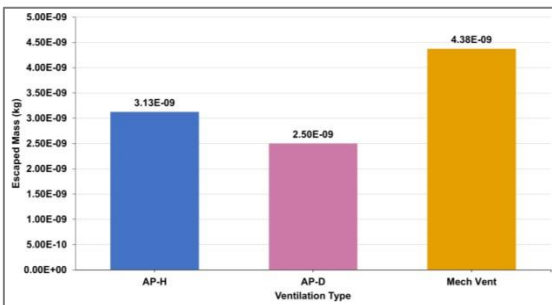

Figure 10. Escaped particle mass through ventilation outlets

Thus, all ventilation systems fail to remove a majority of the 3.13e-8kg of infectious particulate from the zone. As a result, the majority of the particulate is still present in each zone on walls and surfaces. This incurs a further infection risk as infectious particles can often sustain on surfaces for multiple days depending on the material.

C. Penetration distance results

Figures 11, 12, and 13 present the maximum penetration distance of particles within the zone from person 1. The penetration data has been coordinated with the distance of each susceptible person to identify if particles could potentially come in contact with them. This indicates the performance to control pathogen spread.

It is assumed that 1.25e-09 kg of particulate mass represents an infectious load of COVID-19. Therefore, periods of particle mass >1.25e-09 kg indicates a higher infection risk and flow times in which <1.25e-09 kg indicate a lower infection risk (Anand et al, 2020)
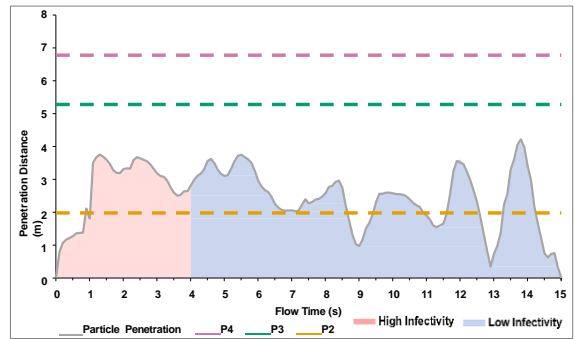

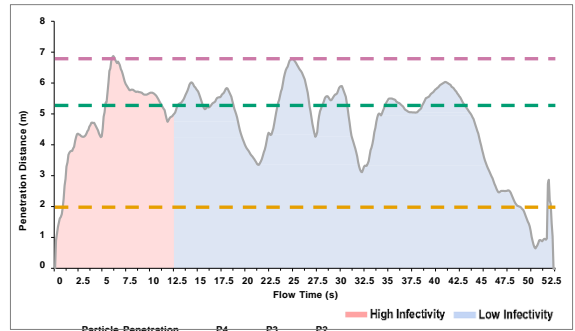Figure 11. Penetration distance of particles - Mechanical ventilation

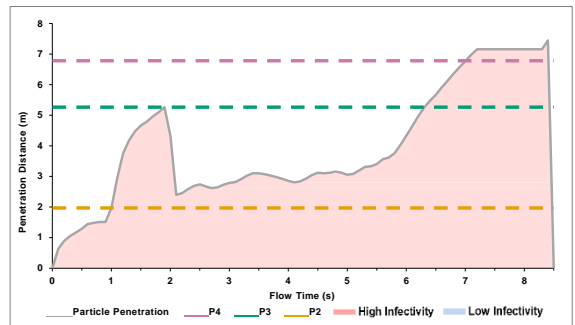Figure 12. Penetration distance of particles - AP-H ventilation

Figure 13. Penetration distance of particles - AP-D ventilation

Overall mechanical ventilation sees the highest performance with only 1 susceptible person potentially inhaling an infectious load. The air purification devices in comparison present a lower performance with 3 potential infectious load inhalations for AP-H and 2 potential infectious load inhalations for AP-D. This indicates a lower efficacy for infection control for the air purification devices.

D. Results summary

The results indicate mechanical ventilation as the highest performing system. For all results, the air purifiers fail to meet or exceed the performance of the mechanical ventilation systems and thus could potentially result in a higher risk of inhalation of infectious particulate. When comparing the performance of the air purifiers, AP-H generally sees a higher performance than AP-D with shorter reduction time and higher escaped mass, however, AP-H does perform lower on penetration distance. These results shall now be further analysed in the context of air and particle flow patterns to further understand the cause of performance differences.

E. Computational Fluid Dynamics Discussion

The mass in domain results identified a performance variation in the reduction of airborne cough particulate. The particle flow patterns indicate that a higher particle velocity (moving towards an outlet) correlates with a higher reduction of concentration.
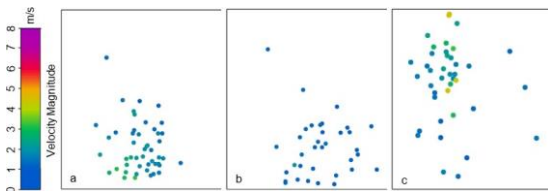

Figure 14. Particle velocity (a) AP-H , (b) AP-D, (c) Mechanical Ventilation

The peak particle velocity was identified to be 2m/s, 2.5m/s, and 5m/s, for AP-D, AP-H, and mechanical ventilation respectively. Despite the similar flow rate of AP-H and mechanical ventilation, the velocity is significantly higher for mechanical ventilation. This occurs as the particles have to change direction and momentum to move towards the air purifier outlet whereas for the mechanical ventilation, the momentum is carried from the initial cough, thus resulting in higher overall velocity towards the outlets.
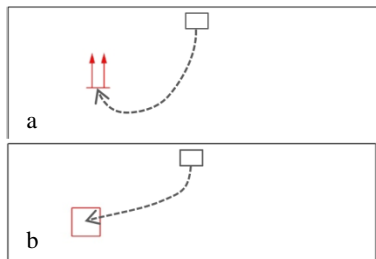

Figure 15. Directional change (a): AP=H, (b): Mechanical Ventilation

The outlets of the air purifiers are positioned away from the direction of the cough; thus the particles undergo a change in momentum as they flow towards the outlets. This change negatively impacts the reduction time as the momentum from the initial injection is lost. Therefore, outlet position has an impact on velocity and subsequently mass reduction speed as a result of directional change.

The results identified that all ventilation systems fail to effectively remove infectious particulate from the zone with the majority of the particulate still present in each zone on walls and surfaces. Despite the particle moving in the direction of the outlets, the results show that the quantity of escaped mass is significantly smaller than the total injected mass. Although the particles move towards the outlet, it seems as though they become scattered and subsequently miss the outlet and contact the air purifier body and surrounding surfaces. Prior research has found that the size of the outlet is the primary limiting factor, impacting the quantity of mass escaping the zone [12]. This phenomenon occurs within the results, as mechanical ventilation has the largest outlet (0.18m^2) and the largest escaped mass (4.38e-9kg). However, this hypothesis does not directly correlate with the results for the air purifiers as AP-D has the smallest escaped mass (2.5e-9kg) with an outlet (0.075m^2) that is greater than that of AP-H (0.063m^2). This seems to occur as the cough particles move towards a single side of the AP-D air purifier and thus do not utilise the full surface area of the circular outlet, therefore, the effective outlet surface area for AP-D is half the full outlet size at 0.0315m^2. These findings indicate that the size of the outlet of each ventilation system impacts the total escaped mass, and as a result of the air purifiers having a smaller particle capture area they cannot remove as much mass as the mechanical ventilation system.

The results identified that AP-H and AP-D fail to effectively control the penetration of infectious particulate whereas the mechanical ventilation system can control particulate with much higher effectiveness. The investigation of the air and particle flow patterns has indicated two causes of the performance differential: vertical airflow, and short-circuiting / reach. It appears that vertical airflow from the air purifier inlets negatively impacts the control of particle penetration. As discussed upon injection of the particles, a flow is formed towards the air purifier, however, as a result, the particles intersect airflow coming from the inlet. This causes the particles to gain velocity and then further scatter and penetrate through the zone. This issue seems to be amplified by the low position of the air purification devices as the inlet is much closer to the injection point than the outlet, therefore, the particles are highly likely to come in contact with turbulent upwards air flows.

The particles that subsequently penetrate the zone are further negatively impacted by short-circuiting. Short-circuiting occurs when the flow from the inlets meets with the flow to the outlet causing a stream of air straight from

the inlet to the outlet (See Figure 16). This negatively impacts propagation as the outlet is primarily taking air from the inlet rather than reaching further into the zone. For the air purifiers this caused a lack of air currents within the further side of the zone. As a result, particles that propagate far into the bay do not intersect airflow currents towards the outlet, thus, they free flow within the zone. For mechanical ventilation short-circuiting does occur, however, as the system has 2 outlets on either side of the room, therefore there are effective airflow currents towards the outlets at most points within the zone.

Figure 16. Flow patterns (a) AP-H / AP-D, (b) Mechanical Ventilation

IV. TRIANGULATION OF FINDINGS

The findings from both stages indicate both AP-H and AP-D fail to meet the performance of mechanical ventilation. From the infection probability results (Wells-Riley) and the removal and penetration results (CFD) this study can triangulate that the potential for infection under air purification is higher than that of mechanical ventilation. Both stages identified the following limiting factors: inlet and outlet flow rate, and geometry. The findings indicate that air purifiers can result to higher rates of infection and should not be used in place of mechanical ventilation.

Despite the failure to meet the performance of mechanical ventilation, the results from both stages indicate that air purifiers can provide infection control at a higher performance than natural ventilation. Both air purifiers are found to exceed the performance of natural ventilation throughout the infection probability modelling (Wells-Riley) data collection in which it was found that the higher mass flow rates and lower mixing factor of the air purifiers cause higher performance. These findings are corroborated by the CFD data in which it is identified that both air purifiers can reduce the concentration within a short period. The higher performance of air purifiers is caused by the constant forced airflow whereas the varied wind speeds of natural ventilation would cause varied air flow, this generally results in an average fresh air flow rate lower than both air purification units.

The findings from both stages indicate a performance differential between AP-H and AP-D in favour of AP-H. AP-H is found to exceed the performance of AP-D throughout the infection probability modelling (Wells-Riley). The CFD results seem to corroborate these results, in which AP-H sees faster concentration reduction and

higher escaped mass. AP-D did outperform AP-H on penetration distance; however, the overall performance indicates AP-H performs higher. The performance differential occurs due to differences in flow rate and outlet geometry. The higher flow rate of AP-H reduces the infection probability and increases the mass concentration significantly better than that of AP-D. The large square outlet of AP-H sees greater escaped mass than that of the curved outlet of AP-D. Therefore overall, AP-H sees a significantly greater performance than that of AP-D

V. CONCLUSION

This research study aimed to identify the efficacy of air purification devices to provide infection control within NHS hospital environments. Stage A, infection probability modelling enabled the study to assess the performance of air purifiers against current ventilation practices to dilute infectious quanta. Stage B, CFD modelling enabled the study to identify the performance of air purifiers against current ventilation practices to remove and reduce the penetration of infection particulate. Through the triangulation of the findings the study has effectively benchmarked the performance of air purifiers by comparing them to currently accepted ventilation practices. By investigating a domestic and medical based air purification units the study has also generated a greater understanding of the potential performance of differing air purifiers. Overall, the study has provided new knowledge as to the theoretical performance of air purifiers that can assist hospitals to increase ventilation in poorly ventilated areas.

VI. REFERENCES

1. Agwu, C. 2021. "Nosocomial infection hospital acquired covid-19", pp.12-16.
2. Anand, S. and Mayya, Y. Size distribution of virus laden droplets from expiratory ejecta of infected subjects. In *Scientific Reports*, vol. 10, 2020
3. Chen, S., Liao, C., Li, S. and You, S. "A Probabilistic Transmission Model to Assess Infection Risk from Mycobacterium Tuberculosis in Commercial Passenger Trains. Risk Analysis". 2010. pp.930-939.
4. Escombe, A., Oeser, C., Gilman, R., Navincopa, M., Ticona, E., Pan, W., Martínez, C., Chacaltana, J., Rodríguez, R., Moore, D., Friedland, J. and Evans, C. "Natural ventilation for the prevention of airborne contagion". In *PLoS Medicine*,2007. vol. 4. p.68.
5. Gammaitoni, L. and Nucci, M. 1997. "Using a mathematical model to evaluate the efficacy of tb control measures". In *Emerging Infectious Diseases*. vol. 3. pp.335-342.
6. Liao, C., Chen, S. And Chang, C. "Modelling respiratory infection control measure effects". in *Epidemiology and Infection*. 2007. vol. 136, pp.299-308.
7. National Health Service. 2021. "Health technical memorandum 03-01" *London: National Health Service*, pp.23-32.
8. NHS Digital, 2020. "Summary Reports - Performance Times and Waits for Admissions". Online
9. Noakes, C., Beggs, C., Sleigh, P. And Kerr, K. 2006. "Modelling the transmission of airborne infections in enclosed spaces". In *Epidemiology and Infection*. vol. 134. pp.1082-1091.
10. Qian, H., Li, Y., Nielsen, P. and Huang, X. "Spatial distribution of infection risk of SARS transmission in a hospital ward". In *Building and Environment*. 2009. vol. 44. pp.1651-1658.
11. Rudnick, S. and Milton, D. "Risk of indoor airborne infection transmission estimated from carbon dioxide concentration". in *Indoor Air*. 2003. vol.13. pp.237-245
12. Turner, L. 2021. "Infection Control Through Mechanical Ventilation in a Hospital Ward Scenario". Unpublished

3rd Place
HVAC World
Student Competition

Indra Permana
USA

Performance Improvement of a Biotechnology Vaccine Cleanroom for Contamination Control

Indra Permana[1], Fujen Wang[2]

Department of Refrigeration, Air Conditioning and Energy Engineering, National Chin-Yi University of Technology, Taichung 411, Taiwan; [1] indra.refrigeration@gmail.com; [2] fjwang@ncut.edu.tw (M.S. Thesis accepted in July 2021)

Abstract—The contaminants, temperature, humidity, and pressure are all strictly regulated in cleanrooms. Contamination control is crucial in several industries to assure product reliability, including pharmaceuticals, specifically for vaccine cleanrooms. This study investigates a biotechnology vaccine cleanroom using a comprehensive field measurement test and numerical simulation analysis. Field measurements were taken during the at-rest and operational occupancy states. As a result, it was discovered that the operational condition has a higher concentration than the at-rest condition. The improvement approach used in this study, numerical simulation, aimed to reduce concentration under operational conditions. The strategy proposed in this simulation is determining the ventilation rate and arranging the outlet air grilles. The ventilation and removal efficiency in at-rest conditions is 90.0% and 86.2%, while concentration increases in the operational condition, and efficiency drops to 81.3% and 80.1% for the baseline case. After the proposed improvement design, the ventilation and removal efficiency in the operational condition could improve by up to 6.8% and 5.2%, respectively. A proper arrangement of outlet air grilles could control decreasing the concentration. In addition, a higher ventilation rate also could decrease the concentration. However, it caused high energy consumption. Therefore, the ventilation rate must be designed optimally to compromise contamination control and energy saving.

Index Terms— Biotechnology cleanroom, vaccine, field measurement, numerical simulation, contamination control.

I. Introduction

Controlling contamination is key in several industries in assuring product reliability, such as pharmaceuticals specific for vaccine cleanrooms [1]. Cleanrooms are spaces with strict control of the contaminants, along with temperature, relative humidity, and pressurization [2]. The particle count is the most important test to ensure a cleanroom works correctly. A particle counter is used to count and size particles in the air of a cleanroom. The particle concentration in the cleanroom could be affected by the conditions outside the cleanroom. The cleanroom pressure differential impacts cleanliness, especially around the cleanroom door. It was found that 0.04 in. (10 Pa) or higher is an adequate pressure differential to minimize particle migration from a less-clean corridor to a cleanroom [3]. Besides that, physical movements can induce more particles. Human movement at a walking speed of 1.0 m/s induced more particles into the cleanroom than at a walking speed of 0.5 m/s. The reduction rate of the particle concentration was larger when the doorway airflow was increased. Increasing the doorway airflow reduced the

adverse effect caused by human movement [4]. In addition, an airlock can reduce the migration of contaminants into the cleanroom. Poor airlock design concepts may cause undesired migration of chemical fumes, particles, or microbiological agents, which can be toxic, harmful, or infectious, into protective areas or cause contaminated products or processes from excessive airborne contaminants inside the controlled environments [5].

When maintaining a controlled environment, cleanrooms can be 10–100 times as energy-intensive as typical office buildings (in terms of cleanliness, temperature, relative humidity, and pressure) [6]. Many reports have indicated that cleanroom supply airflow rates are often over-designed to meet the air cleanliness classes, and over-supply can cause significant energy consumption [7]. Loomans et al. [8] conducted experiments in a demonstration cleanroom to examine how an ideal airflow pattern may be achieved in the cleanroom, resulting in a high contaminant removal efficiency, and contributing to a more energy-efficient cleanroom. A probabilistic optimal design method of air-conditioning systems is developed for cleanrooms/spaces requiring strict temperature and humidity controls. It could facilitate optimal ventilation control strategies to be implemented successfully under uncertainties [9].

Field measurements are essential in assuring a cleanroom performs satisfactorily and achieves contamination standards. The field test for contamination control in the cleanroom was conducted by Wang et al. The biological contamination control strategies under different models have been simulated and then compared with field measurement to check the acceptable level of consistency [10]. Besides, it reported that contamination could not be minimized, but targeted monitoring should be undertaken through the data reviewed and examined for trends [11]. Testing results would be a basic validation for a cleanroom in performing a simulation. The CFD simulation can predict airflow patterns and investigate the accumulated contamination. The solution given by CFD to these predictions is quite effective because it can overcome the limitations of the experimental method of direct measurement. Nowadays, CFD simulations are important tools for simulating various fields, such as the HVAC system, to determine ventilation control in a room by predicting airflow patterns and its ability to remove airborne particles [12]. Rouaud et al. [13] conducted numerical simulations on pollutant removal efficiency in food processing cleanroom environments. In the general cleanroom, higher ventilation rates are often used to maintain the required cleanliness level for the environment. But higher ventilation rates will cause more energy

consumption and not ensure the required cleanliness level. Chung [14] used CO_2 as a pollutant to assess indoor ventilation efficiency. The numerical simulation was used to examine the airflow pattern through the experiments to verify the concentration simulation scenarios. There are still few studies on the biotechnology cleanroom, especially for vaccines, despite the extensive use of CFD simulations and field measurements. In this study, field measurement tests are used to examine the biotechnology vaccine cleanroom, and CFD techniques are also used to analyze and identify performance improvements for contamination control inside the cleanroom.

II. METHODOLOGY

A. Cleanroom Layout and Design

The investigated biotechnology cleanroom is part of the pharmaceutical cleanroom focused on vaccine production. The layout is illustrated in Fig. 1. The cleanroom has various cleanliness levels, classified as Grade C, D, and E for pharmaceuticals. The main manufacturing process is for a syringe-filling vaccine classified as Grade C according to the Pharmaceutical Inspection Co-operation Scheme (PIC/S) and Good Manufacturing Practice (GMP) [15]. The production machines already existed in the biotechnology cleanroom. Besides syringe filling, Grade C is used in the weighing, formulation, vestibule, sterile part equipment, washing, material airlock, and gowning rooms. Grade D is used for the transfer room and personnel airlock. Then, Grade E is a grade for a non-sterile area such as a corridor.
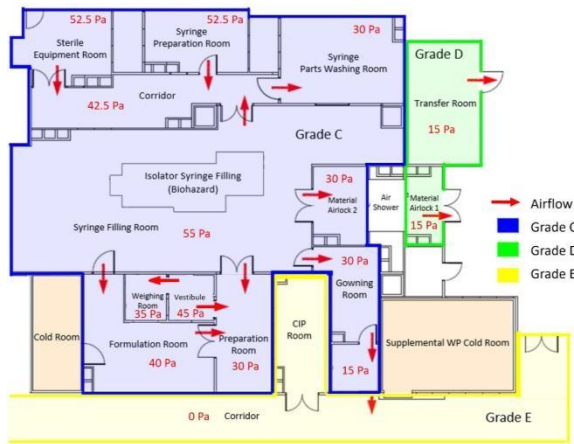

Figure 1.   The layout of the investigated vaccine cleanroom

In this research, the focus will be on investigating the syringe filling room. The indoor environmental parameters design includes temperature maintained at 19±2°C and relative humidity <60%. The ACH is maintained at 25, and pressurization is at 55 Pa. There are 15 high-efficiency particulate air (HEPA) filters installed with a dimension of 1200 mm x 600 mm. HEPA filters, which have a 99.997% efficiency rating according to grade MERV 18 or H14 and can trap particles sized at 0.3μm, are used for filtration. HEPA filters are designed to effectively capture and filter out very fine particles.

B. Field Test and Data Collection

The indoor environment parameters were thoroughly examined through field measurement. At-rest and operational conditions are the two occupancy states used to evaluate the performance of cleanrooms. It should be certified according to these parameters: airflow rate, temperature, relative humidity, particle counts, and pressurization. All parameters should be qualified based on the design standard. However, before experimental data retrieval, HEPA leakage testing must be carried out to ensure the cleanroom's HVAC system is in good operating condition. Fig. 2 illustrates a diagram of the HEPA leak test. All airborne particles larger than 0.5 μm must be eliminated by the HEPA filter at a rate of at least 99.997%. The maximum allowable leakage should be 0.01%, and the leak test was run for 1 minute. The HEPA filter's integrity is examined through a method called poly alpha olefin (PAO) testing. These experiments produce an aerosol similar to particles in its characteristics. The test will attest to the HEPA filter's integrity and prove no leaks or damages. Data retrieval for airflow rate, temperature, relative humidity, pressure, and particle counts can be done after the HEPA filter is completely operational. The specification of all apparatus is shown in Table 1.
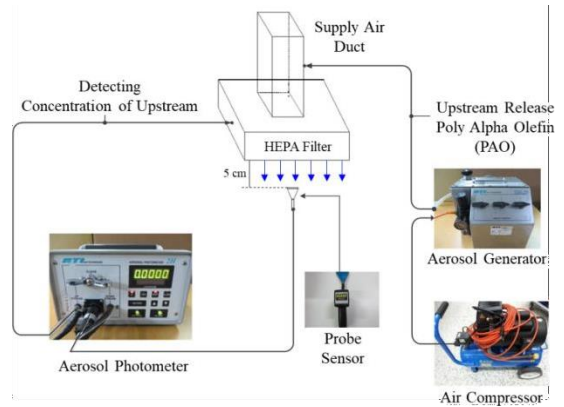

Figure 2.   Schematic diagram of HEPA leakage test

TABLE I.
APPARATUS FIELD MEASUREMENT

Parameters	Apparatus Model	Operative Range	Accuracy
HEPA Leak Test	ATI TDA 2H	0.0001% - 100%	±0.05%
Temperature Relative Humidity	TSI TA465P	-10 ~ 60°C 5 - 95% RH	±0.3°C ±3%RH
Air Velocity Pressure	TSI 8380	0.125 - 12.5 m/s Diff ± 3735 Pa	±3% ±2%
Particle Counter	AeroTrak TSI	0.3, 0.5, 1, 3, 5, 10 μm	±5%

C. CFD Simulation

The simulation was performed by using the Ansys Fluent software version 2020 R2. It provides several equations to solve the problems, including laminar and turbulent fluid flow problems, incompressible and compressible fluid, and other problems. The full-scale geometric layout of the investigated biotechnology vaccine cleanroom is illustrated in Fig. 3. The geometry was created based on the actual size and situation of the investigated cleanroom. The geometrical elements of the model were simplified during this study because the high-level detail of the model would not significantly influence the overall simulation results. On the other hand, it will consume a lot of resources and time when performing calculations.
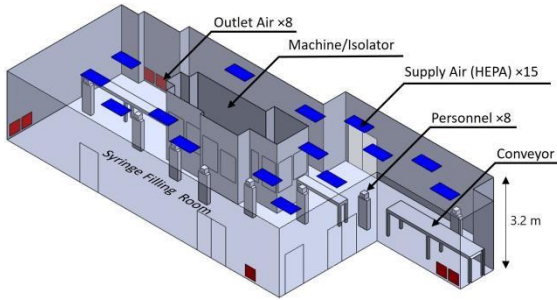
Figure 3.   The geometry of the investigated vaccine cleanroom

In this study, the Semi-Implicit Method for Pressure-Linked Equation (SIMPLE) was adopted to solve all the governing equations simultaneously. The realizable k-ε was selected as the turbulence model. A total of 8 personnel were implemented into the geometry design to simulate the operational condition. The personnel will generate some airborne contaminants. Then it will evaluate the concentration inside the cleanroom. Transient numerical simulation was carried out to monitor and investigate the airborne contaminant. The tracer gas method was used in this simulation to certify the contamination level in the investigated cleanroom. Carbon dioxide (CO_2) was selected and assumed as particles or concentration generation from the personnel. The initial condition for the concentration is set at 3,000 ppm. Concentration is monitored for 500 seconds to determine the change in concentration level in the investigated cleanroom. Table 2 shows the details of the boundary condition to perform the numerical simulation.

TABLE II.
THE BOUNDARY CONDITION FOR NUMERICAL SIMULATION

Boundary Condition	Type	Value
Supply Air	Velocity Inlet	Velocity: 0.2822 m/s Temperature: 19.2°C Concentration: 400 ppm
Outlet Air	Pressure Outlet	Pressure: 55 Pa
Personnel concentration [16]	Velocity Inlet	Velocity: 0.1875 m/s Concentration: 38,000 ppm
Wall	Wall	Adiabatic; no heat transfer
Personnel	Wall	Heat flux: 38 W/m²
Machine	Wall	Heat flux: 57 W/m²

D. *Proposed Study*

Determining the best location for supplying air or outlet air grilles is essential to ensure good airflow effectiveness and avoid dead zones with stagnating airflow and higher loaded particle concentration. CFD simulation with particle tracer could support this in the design phase to attain a well-designed room airflow. A total of 6 cases were analyzed in this study to find the improvement strategy of concentration control. Various cases are described as follows:

- Case 1: Existing design (at-rest condition)
- Case 2: Existing design (operational condition)
- Case 3: Operational condition (increased ACH to 35)
- Case 4: Operational condition (increased ACH to 50)
- Case 5: Operational condition added 1 outlet air grille
- Case 6: Operational condition added 3 outlet air grilles

III. RESULTS AND DISCUSSION

A. *Experimental Results and Verification*

The biotechnology vaccine cleanroom was examined both while it was unoccupied and when it was occupied. Field measurements were taken in each of the 16 rooms. With a total of 16 rooms, field measurements were done in each one. However, only the syringe filling room will be analyzed in the CFD simulation part. The experimental results for 16 rooms revealed that temperature ranges from 19.5°C to 21.7°C, while relative humidity ranges from 45% to 51.4%. In addition, to maintain the air quality, it must have sufficient clean air supplied to dilute and remove the airborne contamination generated within the cleanroom. So, the contamination can be prevented during the production process. The total air volume of 10,953 CMH for the syringe filling room was obtained from field measurement. Its room volume is 424.07 m³. So, the ACH is 25.83 compared to the design standard is 25 ACH. According to the standard, the ACH in this investigated cleanroom is qualified. Then, the number of particles counted in the at-rest condition is 12,580 particles at a size ≥0.5µm, which is less than the maximum standard permitted of 350,000 particles/m³. In comparison, the number of particles increases during operational conditions is 113,320 particles at a size ≥0.5µm, but still less than the maximum permitted of 3,500,000 particles/m³. In addition, pressurization is critical to the proper functioning of the cleanroom. Various types of pressurization with 16 rooms have met the pressurization standard.

B. *Validation*

During the numerical simulation setting process, the planning and selection of the number of grids will significantly affect the simulation results. The number of grids is critical in affecting simulation calculation efficiency and accuracy. The temperature in 16 points as field measurement is chosen to assess the number of grids. A total of 5 different grids are selected for comparison to verify the accuracy of the results. The grid numbers start at 850,701 to 2,578,392. By increasing the number of grids, the accuracy of the simulation solution is better. However, the time required for the relative simulation operation will be increased. After compromising the simulation time and accuracy, the grid number 2,205,820 was chosen as a follow-up numerical simulation of the grid number. The validation results between field measurement and simulation are shown in Fig. 4. It represents the temperature in the biotechnology vaccine cleanroom, which has a small error percentage. The overall error rate is less than 10%. Validation data shows good agreement in the acceptance temperature design conditions maintained at 19±2°C.
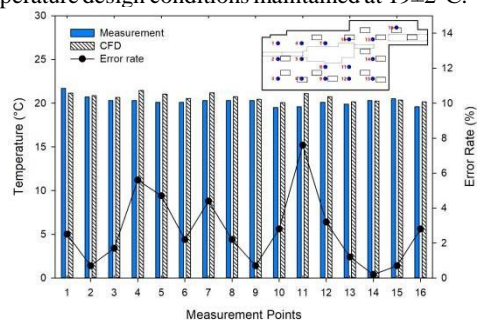

Figure 4.   Validation between field measurement and simulation

C. Temperature and Airflow Distribution

Manufactured products in cleanrooms need accurate control of temperature. The general indoor environment parameters with strict temperature and relative humidity must be maintained, especially for vaccine production. In addition, temperature and relative humidity are related to the growth of microorganisms. Higher temperatures and relative humidity could encourage the growth of bacteria and microorganisms. Fig. 5 illustrates temperature and airflow distribution simulation results during at-rest and operational conditions measured at 1.2 m above the floor. Some heat flux generated by a machine causes a higher temperature, along with the 8-personnel during the at-rest condition. However, the overall temperature is within the acceptable range based on the design criteria kept at 19±2°C.
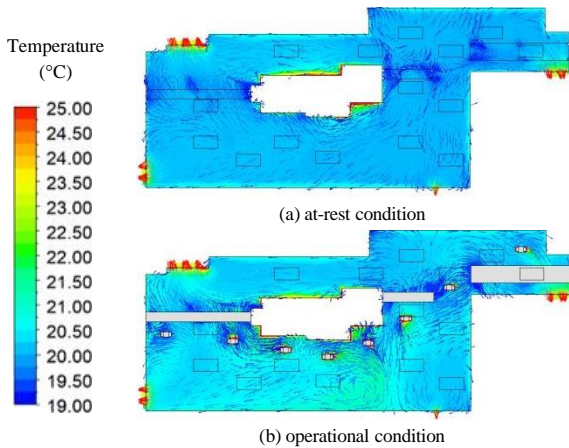
Figure 5. Airflow velocity and temperature distribution

Some differences in airflow patterns occur under at-rest and operational conditions. A better approach to airflow patterns is needed to maintain the biotechnology cleanroom cleanliness. It will certainly affect the airflow of clean air supplied by the HVAC system through the HEPA filters to reduce the contamination in the cleanroom. There is equipment inside the investigated cleanroom but without personnel in at-rest conditions. Airflow is evenly distributed, but some dead zones cause airflow to be blocked by some equipment. The blue color means a lower airflow velocity closer to 0 m/s. The airflow velocity near outlet air grilles becomes higher absorbed. Another case was carried out during operational conditions. Some personnel were included in this case, with 8 personnel. In contrast to this case, adding personnel could make some difference to the airflow distribution. Some airflow that hits the personnel will cause velocity variation. When airflow hits the personnel, it will be some turbulence of airflow. Some dead zone exists in this case in some spot or locations. Personnel inside the cleanroom could induce concentration generation.

D. Contamination and Concentration Distribution

The most important contamination control issue within cleanrooms is air. Air can distribute contamination around the cleanroom, and how particles behave in the air concerning a tendency to settle. Hence the essential part of cleanroom design is through established principles designed to control airborne particles. Concentration concern has been carried out in this research with CFD simulation. A particle tracer was employed in this simulation to analyze the better concentration removal design. CFD simulation was calculated with a transient method for 500 seconds. In the beginning, the simulation used 3,000 ppm for the initialization value. The concentration will decrease along with time until it reaches the steady-state condition. The data simulation was collected every 25 seconds.

Fig. 6 shows the concentration contour every 100 seconds when simulated in at-rest and operational conditions. The addition of personnel in operational conditions resulted in higher concentration levels inside the cleanroom than in at-rest conditions. Compared to the at-rest condition, the concentration almost reaches the steady state condition when stimulated for 400 seconds. Inversely, the operational condition still has a higher concentration. The results reveal that the operational condition had a higher concentration of 598 ppm than the at-rest condition of 415 ppm when simulated until 500 seconds. The position of outlet grilles could affect the concentration removal effectiveness. Improper positioning of outlet grilles makes concentration accumulate in a certain area. The red spot represents the highest concentration. The concentration in the operational condition is not evenly distributed, unlike the at-rest condition, which has been evenly distributed because no concentration is generated from personnel.
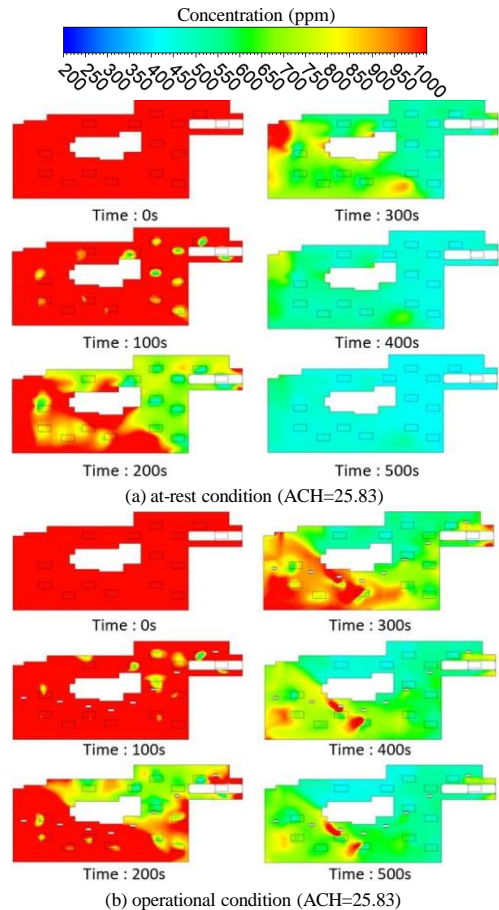

Figure 6. Concentration distribution in different times and conditions

The proposed study with a total of 6 cases simulation results is shown in Fig. 7. Cases 1 and 2 are the original design for at-rest and operational conditions. Increasing the ventilation rate was proposed in cases 3 and 4, while some outlets were added in cases 5 and 6 to make a lower concentration. The concentration distribution was measured at the height of 1.2 m observed. The original condition is in case 1 and case 2. The results reveal that the operational condition has a higher concentration of 598 ppm than the at-rest condition of 415 ppm. The addition of personnel could affect the higher concentration. The concentration in operational conditions is not evenly distributed. Some spots or zone still have accumulated with high concentration. Some improvement strategies were employed in this simulation to enhance the operational condition airflow pattern and make a lower concentration of operational condition approach to the at-rest condition.

A better airflow rate could make better contamination control important in the cleanroom environment. A ventilation system can dilute concentration. Cleanliness type and filter efficiency also influence the airflow rate requirements. It refers to the number of times per hour that filtered the air replaces the existing volumes in the room. The ACH was increased to 35 and 50, respectively, to compare with the existing ACH of 25.83 to check whether the indoor air contamination distribution was properly adjusted. The CFD simulates the locations of monitoring points and adopts the previous section's monitoring points. The contaminant concentration is also higher than the average concentration. Increasing ventilation rates in cases 3 and 4 lower the concentration to 515 ppm and 442 ppm.

Higher ventilation rates are often used to maintain the required cleanliness level for the environment. But higher ventilation rates will cause more energy consumption and not ensure the required cleanliness level. Due to energy consumption, the arrangement of outlet air was conducted as another improvement strategy. In this section, the location of the return air grille may affect the airflow in the cleanroom. Case 5 added 1 return air grille to dilute the concentration to 545 ppm, while case 6 added 2 return air grilles, lowering the concentration to 495 ppm.

By analyzing the distribution of contaminants by simulating and increasing the ACH or supply air velocity, the results showed that increasing the velocity caused enhancement of contaminant removal. The increasing face velocity is based on the cleanroom standard or design requirement of around 0.2 m/s to 0.5 m/s. In addition, the increasing velocity can remove the contaminant in a relatively short time. By analyzing adding return air grilles, the result revealed that added outlet air grilles caused the contamination control improvement. As shown in Fig. 8, the concentration is almost steady after 400 seconds and conducted for 500 seconds. The at-rest condition demonstrates good concentration distribution because of no generated concentration. Many personnel with the operation of equipment may influence the concentration. Contamination control can be improved by increasing the ventilation rate and proper arrangement of outlet air. The higher ventilation rate makes the concentration decrease. However, it caused high energy consumption. Therefore, the ventilation rate must be designed in optimal conditions.
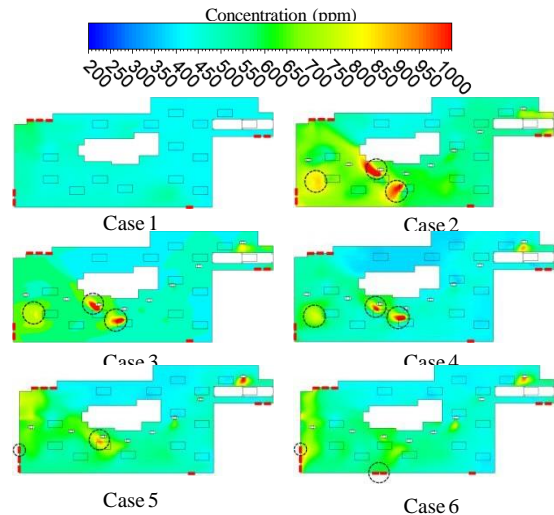

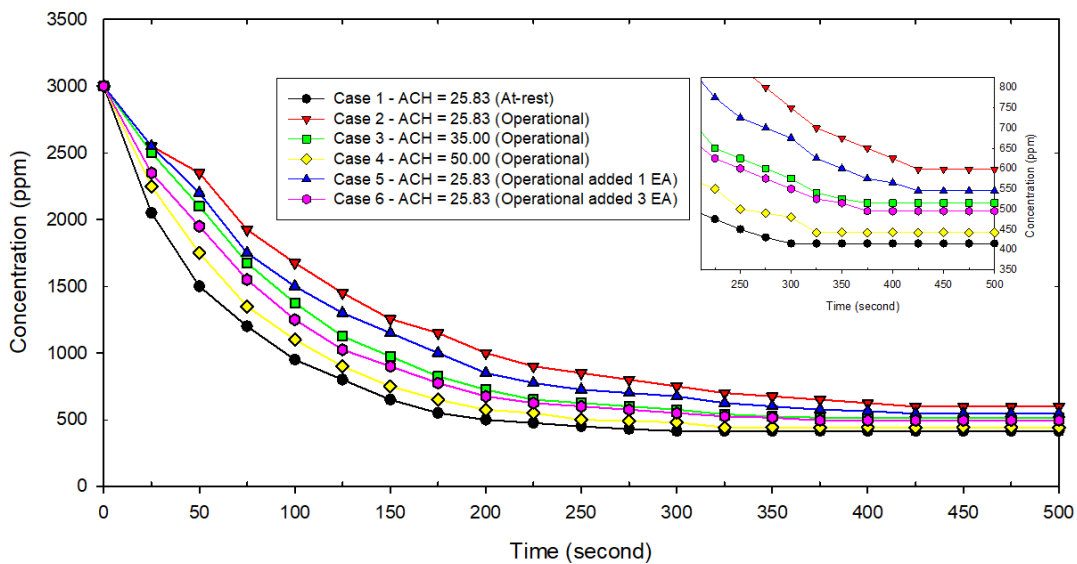Figure 7. Concentration distribution in different cases

Figure 8. Concentration contaminant decay in different case studies

E. Ventilation and removal efficiency

Contamination control is one way to improve the cleanliness of the biotechnology vaccine cleanroom. Effective airflow dispersion is required for the biotechnology cleanroom to eliminate contaminants. We assess how effectively the ventilation system replaces stale air in a space with fresh air by using ventilation and removal efficiency as an indicator to assess the ventilation performance between the concentration of contaminants in the spaces and the concentration of contaminants in the outlet air. Contaminant removal efficiency is defined as the ratio of contaminants in the outlet air to contaminants in a specific place within the occupied area. It measures how quickly the airborne contaminant is eliminated from space.

Fig. 9 displays the ventilation and removal efficiency of the biotechnology vaccine cleanroom. CFD method is used to simulate the six case scenarios. Overall, case 1 has the highest efficiency in both assessments because there is no concentration generation from personnel. In operational conditions, the increasing airflow rate strategy has the highest ventilation and removal efficiency in case 4. The contamination in the cleanroom can be removed more efficiently than in other cases. Another approach for contamination control is a proper arrangement of outlet air in case 5, and case 6 also shows a better efficiency than the original design in case 2. With good ventilation strategies, contamination removal can be more effective.
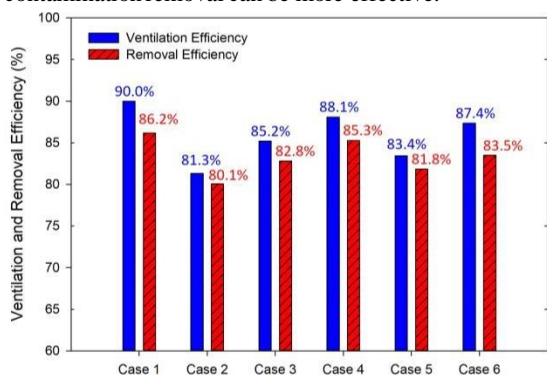

Figure 9. Ventilation and removal efficiency

IV. CONCLUSION

This study investigates the indoor environment parameter in the biotechnology vaccine cleanroom through field measurement tests and CFD simulation to certify, validate, design improvement strategies, and find the effectiveness of the cleanroom system. The performance of indoor environment parameters has been measured comprehensively, including airflow rate, temperature, relative humidity, pressurization, HEPA leak test, and particle counts. The results of the field measurements test show that all the indoor environment parameters are qualified and comply with the design standard. The ventilation and removal efficiency in at-rest conditions has 90.0% and 86.2% because no concentration is generated. Operational condition concentration increases, and efficiency drops to 81.3% and 80.1% for the baseline case. The efficiency of operational conditions could improve by up to 6.8% and 5.2% by adding some improvements. Contamination control can be improved by increasing the

ventilation rate and proper arrangement of outlet air. The higher ventilation rate makes the concentration decrease. However, it caused high energy consumption. Therefore, the ventilation rate must be designed in optimal conditions.

REFERENCES

1 Z. Yang, Y. Hao, W. Shi, X. Shao, X. Dong, X. Cheng, X. Li, X. Ma, "Field test of pharmaceutical cleanroom cleanliness subject to multiple disturbance factors," *J. Build. Eng.*, vol. 42, 103083, Oct 2021.

2 A.S.P. Mendes, A. Rutgersson, M. Paulsson, "Outdoor environmental effects on cleanrooms–A study from a Swedish hospital pharmacy compounding unit," *Eur. J. Pharm. Biopharm.*, vol. 177, pp. 100-106, Aug 2022.

3 W. Sun, K. Flyzik, J. Mitchell, "Cleanroom Pressurization Strategy Update-Quantification and Validation of Minimum Pressure Differentials for Basic Configurations and Applications (Part 2)," *ASHRAE Trans.*, vol. 119, Jan 2013.

4 X. Shao, K. Hashimoto, L. Fang, A.K. Melikov, K.G. Naydenov, C. Rasmuseen, "Experimental study of airborne particle transmission through the doorway of a cleanroom due to the movement of a person," *Build. Environ.,* vol. 183, 107205, Oct 2020.

5 W. Sun, "Cleanroom airlock performance and beyond," *ASHRAE J.*, vol. 60, pp. 64-69, Feb 2018.

6 C. Zhuang, K. Shan, S. Wang, "Coordinated demand-controlled ventilation strategy for energy-efficient operation in multi-zone cleanroom air-conditioning systems," *Build. Environ.*, vol. 191, 107588, Mar 2021.

7 L. Zhou, W. Sun, C. Huang, H. Li, Z. Zou, C. Wu, "Studies on Comparison of Particle Concentration Models for Cleanroom," *Proc. Eng.*, vol. 205, pp. 3308-3315, Jan 2017.

8 M.G.L.C. Loomans, P.C.A. Molenaar, H.S.M Kort, P.H. Joosten, "Energy demand reduction in pharmaceutical cleanrooms through optimization of ventilation," *Energy Build.*, vol. 202, 109346, Nov 2019.

9 C. Zhuang, S. Wang, K. Shan, "Probabilistic optimal design of cleanroom air-conditioning systems facilitating optimal ventilation control under uncertainties," *App. Energy,* vol. 253, 113576, Nov 2019.

10 F. Wang, I. Permana, K. Lee, D. Rakshit, P.P. Rosulindo, "Improvement of Airflow Distribution and Contamination Control for a Biotechnology Cleanroom," *Atmosphere*, vol. 13, 335, Feb 2022.

11 T. Sandle. *Pharmaceutical microbiology: essentials for quality assurance and quality control*. Woodhead, Cambrige, UK, 2015.

12 Z. Sun, S. Wang, "A CFD-based test method for control of indoor environment and space ventilation," *Build. Environ.*, vol. 45, pp. 1441-1447, Jun 2010.

13 O. Rouaud, M. Havet, "Numerical investigation on the efficiency of transient contaminant removal from a food processing clean room using ventilation effectiveness concepts," *J. Food Eng.*, vol. 68, pp. 163-174, May 2005.

14 K.C. Chung, S.P. Hsu, "Effect of ventilation pattern on room air and contaminant distribution," *Build. Environ.*, vol. 36, pp. 989-998, Nov 2001.

15 Pharmaceutical Inspection Convention and Pharmaceutical Inspection Co-operation Scheme (PIC/S). *Guide to Good Manufacturing Practice for Medicinal Products Annexes*. Geneva, Switzerland, 2018.

16 F. Wang, I. Permana, D. Rakshit, B.Y. Prasetyo, "Investigation of airflow distribution and contamination control with different schemes in an operating room," *Atmosphere*, vol. 12, 1639, Dec 2021.

3rd Place
REHVA
Student Competition

Miguel Rodríguez Fernández
Spain

Study of an indirect evaporative heat exchanger prototype manufactured with 3D printing using plastic materials and design of a test bench

Student: Miguel Rodríguez Fernández – E-mail: mrodriguezfernandez98@gmail.com
Supervisor: Manuel Ruiz de Adana Santiago – E-mail: manuel.ruiz@uco.es
University of Cordoba, Superior Polytechnic School, Campus Rabanales, 14071, Andalusía, Spain
Approved date: 28 September 2022

Abstract— **In this study, a prototype heat exchanger manufactured with 3D printing using plastic materials has been investigated as an alternative to traditional HVAC methods. This type of device operates based on the fundamentals of indirect evaporative cooling, a technology that has certain features and advantages that make it a great option to consider as a substitute for older systems. In order to characterize the thermal behavior of the prototype with sufficient reliability, a DOE has been established to cover the climatic conditions of possible situations of interest. In parallel, to simulate the conditions for studying the prototypes, the design of a new test bench has been carried out, consisting of various combined systems. The analysis of the heat exchanger results showed a reduction in air temperature of up to 21ºC between the inlet and supply air. In terms of cooling power, the prototype reached 440 kW, in addition to a maximum EER of 26, much higher than conventional equipment. Regarding device's ability to cool the air to the theoretical limit, the dew point efficiency has shown maximum values of 88%, indicating an excellent performance due to its proximity to maximum capacity. The highest wet bulb efficiency also reached 120%, confirming the successful operation of the equipment.**

Keywords— **Compactness, dew point efficiency, EER, experimental design, HVAC, indirect evaporative cooling, test bench, wet bulb efficiency.**

Introduction

The complexity of the situations in which the industrial sector is being involved year after year has not ceased to increase due to the constant appearance of problems in terms of health, energy prices and basic resources, shortage of raw materials, CO2 emissions and pollution, global warming... Facts that highlight the immediate need to develop solutions that enable the sector to adapt to this dynamic and complicated scenario.

Translating the aforementioned problems into data, from the end of 2021 to mid-2022, the final monthly average price of electricity in Spain reached values above 250 euros per megawatt-hour, reaching figures even 6 times higher than those recorded years ago [1]. Regarding carbon dioxide in the atmosphere, despite the plans to contain emissions that have been drawn up (Kyoto, Paris...), the concentration has not stopped increasing and is currently at values above 400 ppm, the highest ever measured on Earth [2]. The consequences of this are reflected in the increase in the average global temperature of the Earth's surface, which has already reached an increase of one degree Celsius with respect to the average temperature calculated between 1901 and 2000 [3].

In relation to all of the above, the construction sector is identified as one of the main sectors responsible for total energy consumption and greenhouse gas emissions, accounting for 40% and 35% respectively worldwide. Specifically, within this sector, HVAC systems (Heating, Ventilation and Air Conditioning) are the ones with the highest consumption, accounting for 50% of the total, which is equivalent to 20% of final energy consumption [4]. This factor, combined with the rising price of energy, with increasingly higher (what makes the use of these systems indispensable), and taking into account that traditional equipment uses greenhouse gases that are increasingly subject to prohibitions, leads to the conclusion that this sector is a major focus of action to seek alternatives to the technologies used to date. In this way, solutions could be found to the unceasing problems that must be faced at present and those that may arise in the future.

Thus, the answer to this was found in evaporative cooling technology, which has very high efficiency values compared to traditional systems and also does not need refrigerants that cause greenhouse effect, since it uses only water and air as working fluids. For this reason, this project has consisted of the experimental analysis of a prototype of a regenerative indirect evaporative cooler, manufactured by 3D printing with plastic materials in collaboration with the ANDALTEC Technology Center, with the main objective of characterizing the energy performance of the equipment, as well as the influence of different climatic conditions on the performance parameters of the equipment. In addition to this main objective, the secondary goal consisted of designing an experimental plant to carry out the necessary tests, for which the different equipment and electrical and control systems were selected.

Evaporative Cooling description

Evaporative cooling is a thermodynamic principle that has been used for several thousand years. The operation is based on the natural process in which the evaporation of water is used to cool the air. This occurs because the heat is used by the liquid water to change phase to water vapor, while increasing the relative humidity (latent heat rise) of the air. At the same time, the water loses part of its sensible heat, which lowers its temperature.

Depending on the interaction between air and water, two main groups can be distinguished: direct evaporative

cooling (DEC), an open-loop process in which air is brought into direct contact with water and the enthalpy of vaporization is used to raise its humidity while lowering the dry bulb temperature; and Indirect Evaporative Cooling (IEC), a closed loop process based on the transfer of heat and mass between two air streams separated by a heat transfer surface, with a dry side where only air is cooled and a wet side where both air and water are cooled [5]. The air stream entering through the dry channels is called primary air, while that flowing through the channels in contact with the water is called secondary air.
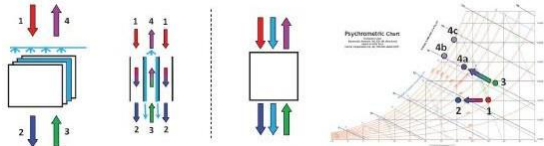
Figure 1. IEC schematic and principle of operation [5].

Within each of the main groups there are numerous types of variants with different characteristics and improvements over the basic ones. In this case, the technology studied during the development of the project was regenerative indirect evaporative cooling (R-IEC). This is a process developed to reduce the temperature at which the primary air arrives at the outlet to values below the wet bulb temperature of the secondary air at the system inlet. This is achieved thanks to the principle of regeneration, which consists of extracting a part of the primary air at its outlet (already cooled) and using it as secondary air, starting from a lower wet bulb temperature than the conventional secondary air flow.

Methods

A. Experimental Plant Design

The design of the experimental plant was carried out with the aim of expanding the capacity and possibilities for conducting research studies, specifically those that require more precise outdoor and local air conditions in terms of temperature, humidity, flow rate and quality. This would allow the study of existing equipment in more varied operating situations in a simpler, more ergonomic, and optimized way.

Therefore, the aim of the new test bench was to reproduce the conditions required by the test matrix in each test. This would require treating the air with specific latent and sensible loads and providing the necessary flow rate. To achieve this, the equipment that were part of the plant included: Air Handling Units (AHUs) with capacity to perform these functions, combined with equipment such as hydraulic pumps, boilers, heating and cooling coils, filters, humidifiers, steam distribution lances, duct systems, valves... With their respective measurement, control, monitoring and data recording systems, all of which would allow to achieve the specific conditions within the AHUs. Consequently, he design of the experimental plant is as shown in the Figure 2.
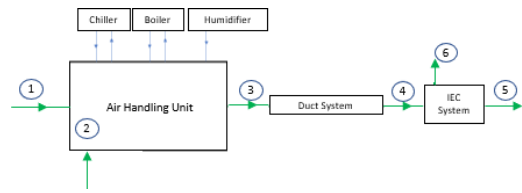

Figure 2. Simplified scheme of the experimental plant.

Along the different points of the proposed plant, the air passes through the different states shown in the TABLE I.

TABLE I.
AIR STATES IN THE EXPERIMENTAL PLANT

STATE	*CONDITIONS*
1	Outside air inlet
2	Mixing of outside and room air
3	Air discharged into the duct system, after passing through the various sections inside the AHU
4	Air at inlet conditions in the prototypes, after losses in the ductwork
5	Supply air to the utilities after passing through the IEC
6	Exhaust air after being recirculated in the IEC

Among the different components of the AHU are: filter to retain particles and other contaminants; air-water cooling coil, consisting of an exchanger through which cold water circulates inside (obtained thanks to the action of a chiller), and which is used to cool and/or dehumidify the air passing through it; heating coil connected to a boiler, with the same principle as the previous one, but with the objective of heating the air, i.e. to provide sensible load; a radial impulsion fan to provide the pressure difference necessary to deliver the required air flow, according to the air characteristic curve; a steam lance to distribute the steam generated in the humidifier in the air circulating through the AHU, and thus provide the latent load.

Complementary to this equipment, the last elements that made up the experimental plant were the control system for the different variables (temperature, humidity, flow rate), the hydraulic pump, and the humidifier; and the Agilent Technologies model 3498A monitoring and data recording system.

B. Design Of Experiments

The phase preceding the execution of the experimental tests was the design of the test matrix, which established the values of the parameters that determined the conditions under which the prototype was studied. The aim was to obtain results that were as significant and representative as possible. For this purpose, the software called "*Statgraphics*" was used, employing the statistical technique called Design Of Experiments (DOE) to identify and quantify the causes of an effect within an experimental study, allowing the determination of the variables that have the greatest influence on a given factor.

In the case of this project, in which the performance of a prototype heat exchanger was to be studied under different inlet air conditions, the design of experiments used was a screening design, specifically of the factorial

type. Therefore, for the creation of the test matrix, the number of experimental factors (independent values) corresponding to the conditions at which the air would enter the equipment, and the number of response (output) variables that would need to be measured during each test to analyze the behavior, were selected. To do this, based on the art study and the conditions at which the unit was to be studied, the experimental factors chosen were: air dew temperature at the unit inlet (T_{re}), dry bulb temperature at the inlet (T_e), inlet air volume flow rate ($\dot{V}_e$) and secondary air rate with respect to the air entering the unit, also called recirculation (R). For each of the factors, a low and a high value was also defined as shown in TABLE II. , with the objective of combining all of them to obtain the final matrix.

TABLE II.
AIR STATES IN THE EXPERIMENTAL PLANT

Factors	Low value	High value	Units
A: T_e	30	45	ºC
B: T_{re}	7.4	21.6	ºC
C: $\dot{V}_e$	90.5	120	m^3/h
D: R	0.4	0.6	-

C. Experimental tests realization

The studied prototype corresponded to a new type of regenerative indirect evaporative cooler developed by the University of Cordoba in collaboration with ANDALTEC.

The two materials used to manufacture the prototype were: gold PLA, a material based on polylactic acid with the addition of bronze, with hydrophobic behavior and improved thermal conductivity; and Layfelt, a composite of felt integrated in a polymeric matrix of polyvinyl alcohol, resulting in a porous material with excellent hydrophilic properties.

TABLE III.
CHARACTERIZATION OF THE EQUIPMENT MATERIALS

Material	Cp (J/g·K)	α (cm²/s)	ρ (g/cm³)	σ (W/ m·K)	HDT (ºC)	WSP (%)	W10M (%)
LayFelt	2,095	0,000992	1,1386	0,239	-	32	40
Gold PLA	1,945	0,0816	1,2781	0,261	60	0,1	0

The dimensions of the area of the equipment where the heat exchange takes place are 38x14x4.7 cm (length x height x width), leaving another 12 cm of height approximately for the water reservoir used to run through the wet channels. In total, the equipment has 80 channels, divided between dry and wet, with a width of 3 mm and a height of 15.3 mm.
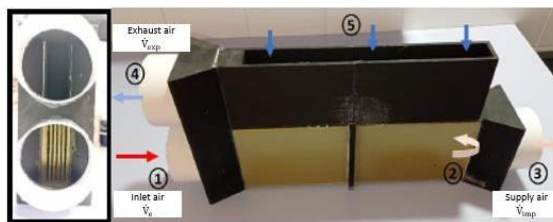

Figure 3. Front (left) and side (right) view of the analyzed prototype.

The air circulation mechanism in the prototype starts at point (1), where the hot air arrives at the dry channels under the conditions set in the test matrix. This air circulates through the dry channels while being cooled at constant humidity until it reaches the end of the exchanger at point (2), where recirculation takes place depending on the overpressure generated in the zone, so that a portion of the air flows through the wet channels until expulsion at point (4), while the other part of the air is driven to the corresponding services (process or useful air) at point (3). The water inlet into the wet channels occurs at point (5).

The instrumentation of the unit is shown in Figure 4. , where the symbol "T" stands for the dry bulb temperature sensors, "T_r" for the dew temperature sensors, "$\dot{V}$ " for the flow sensors and "ΔP" for the pressure sensor.
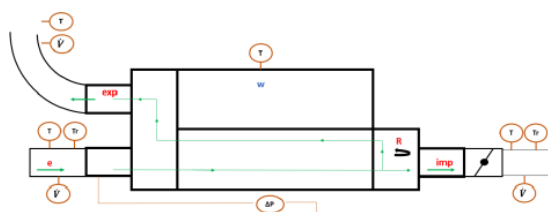

Figure 4. Prototype instrumentation scheme.

The sensors with which the prototype was equipped are shown in the TABLE IV.

TABLE IV.
MAIN CHARACTERISTICS OF THE USED SENSORS

Measured variable	Sensor	Brand
Dry bulb temperature	PT100	GE
Dew temperature	Chilled mirror	GE
Air flow	Windlass (100 mm)	Testo
Press	Pitot	Testo

Thus, with the experimental plant, the design of experiments and the prototype with its instrumentation, the system was subjected to the 18 different experiments

defined in the test matrix, and the results of the output variables were measured for each of them.

Data Presentation and Discussion

A. Measured and calculated variables

There are certain parameters that are used to determine the thermal performance of a unit. These parameters are calculated by measuring specific variables that define the state of the air at each point. The variables measured and the parameters calculated are described below.

- Measured variables

Dry bulb temperature, T. This variable, expressed in ºC, was measured at three different points; at the air inlet point of the equipment (T_e), at the supply area to the services (T_{imp}) and at the recirculated air outlet area (T_{exp}). With this measurement, one of the two variables necessary to know the psychrometric state of the air at each point of the exchanger was already known.

Dew point temperature, T_{pr}. This is measured in ºC and corresponds to the highest temperature at which the water vapor present in the air at a given pressure begins to condense, producing phenomena such as dew, mist or, if the temperature is low enough, frost. The variable was both measured at the IEC inlet (T_{re}) and at the discharge (T_{rimp}). It was the second variable needed to know the psychrometric state of the air at those points, and allowed obtaining other variables such as density (ρ, kg/m³) or specific enthalpy (h, kJ/kg) from the corresponding diagram.

Pressure drop, ΔP. The pressure drop, measured in "Pa", refers to the static pressure drop of the air as it passes through the ducts of an IEC unit. This value indicates the pressure difference that the fan has to provide to deliver a given flow rate. This variable was measured by connecting two flexible tubes to orifices placed both at the air inlet point of the equipment and at the outlet point, so that the differential pressure between both points could be read by means of the "Testo" device.

Air flow rate, $\dot{V}$. The air flow rate refers to the volumetric flow rate of air passing through the channels of the IEC equipment. It is usually expressed in m³/h or m³/s. If the density of the air is known, it can be converted to air mass flow rate, expressed in kg/h or kg/s. This variable was measured at the IEC inlet ($\dot{V}_e$), at the supply ($\dot{V}_{imp}$) and at the discharge to the outside ($\dot{V}_{exp}$).

- Calculated parameters

Wet bulb efficiency, ε_{bh}. This is a parameter describing the degree of approximation of the product air temperature at the IEC outlet versus the wet bulb temperature of the inlet working air, and can be defined as:

$$\varepsilon_{bh} = \frac{T_e - T_{imp}}{T_e - T_{bhe}} \quad [-] \tag{1}$$

Dew point efficiency, ε_{pr}. This is another parameter used for the same purpose as the previous one, and is defined as the ratio of the temperature difference between the inlet and outlet product air temperature to the temperature difference between the dry bulb temperature of the product air at the inlet and the dew point temperature of the working air at the inlet. This reflects the degree of approximation of the product air

temperature at the outlet versus the working air dew point at the inlet, and is formulated as follows:

$$\varepsilon_{pr} = \frac{T_e - T_{imp}}{T_e - T_{re}} \quad [-] \tag{2}$$

Conventional IEC equipment can achieve wet bulb efficiencies between 0.5 and 0.8.

Power/Cooling capacity, $\dot{Q}_{enf}$. The cooling capacity is referred to the enthalpy change of the product air when circulating through the dry channels of the IEC equipment, and is expressed as follows:

$$\dot{Q}_{enf} = \dot{V}_{imp} \cdot \rho \cdot \Delta h_{e-imp} \quad [W] \tag{3}$$

Since the air is cooled to constant humidity in the dry channels, the enthalpy variation of the air could also be represented by the temperature reduction.

Power consumption, $\dot{W}$. IEC systems consume much less power than conventional air conditioning equipment based on mechanical compression refrigeration, since they have to use electrical energy to run the compressor, fans, pumps... while in IEC equipment electricity is only used to drive the fans and pumps. Knowing the pressure drop that the fan has to overcome, the air flow rate it has to drive, and the efficiency of the fan (obtained from the technical characteristics of the fan, with a value of 0.63), the power consumption can be calculated as follows:

$$\dot{W} = \frac{\Delta P \cdot \dot{V}_e}{\eta_{vent}} [W] \tag{4}$$

Energy efficiency, COP or EER. The energy efficiency factor, called COP or EER for its abbreviations, "Coefficient Of Performance" and "Energy Efficiency Ratio" respectively, is the ratio of cooling capacity to power consumption, mathematically expressed as follows:

$$EER = \frac{\dot{Q}_{enf}}{W} \quad [-] \tag{5}$$

This parameter indicates the cooling power that the system can produce for each unit of electrical power consumed.

Inlet-supply temperature variation, ΔT. The temperature differential between two points makes it possible to observe the evolution of the air temperature along the system. Thanks to this parameter, it is possible to observe in which test and under which conditions the highest and lowest thermal jump occurs.

$$\Delta T = T_e - T_{imp} \quad [K] \tag{6}$$

The points between which the temperature difference was measured were at the air inlet to the unit (T_e) and at the air supply to the services (T_{imp}).

Compactness, C. It corresponds to the ratio between the cooling power of the IEC and the volume available for heat exchange, and is expressed in W/m³. The main use of this parameter lies in the comparison of exchangers of different sizes.

$$C = \frac{\dot{Q}_{enf}}{V_{IEC}} \quad [\frac{W}{m^3}] \tag{7}$$

Ratio of secondary air to primary air, R. In IEC equipment, secondary air, also known as working air, is used to cool the primary air (product air). The ratio of the secondary air flow rate to the primary air flow rate has

important effects on the cooling performance of the system, so it is a parameter to be taken into account.

$$R = \frac{V_{exp}}{V_e} \quad [-] \qquad (8)$$

The parameter indicates the recirculation rate in the IEC, by the quotient between the air flow rate expelled, $\dot{V}_{exp}$ (m³/h), and the air flow rate entering the system, $\dot{V}_e$ (m³/h). Thus, the higher the value of R, the greater the proportion of air is expelled and the lesser the amount is driven into the services.

B. Results

After recording the data of the variables in each of the tests, it was observed that the greatest reduction in air temperature in the prototype was 20.9ºC and was achieved at the maximum values of inlet temperature, flow rate and recirculation, being 45ºC, 120 m³/h and 60% respectively, combined with the lowest level of dew temperature, i.e. 7.4ºC.

The lowest supply temperature obtained was 21.8ºC under the same conditions as in the previous case, except for the inlet temperature, which was 30ºC. On the contrary, the lowest temperature reduction in the system was 5.6ºC when the inlet temperature and recirculation were at low levels, while the dew point temperature and flow rate were at the high ones, that is, one of the most unfavorable situations for the cooling efficiency of the equipment.

The highest cooling power was 440.2 kW and was reached with the most favorable conditions for this, with the maximum inlet temperature and flow rate, and with the lowest humidity and recirculation, since this way the highest cooling is achieved and at the same time the highest flow rate is available to carry out the cooling. The lowest cooling power was 76,6 kW under the opposite conditions, with the lowest inlet temperature and flow rate, and the highest humidity and recirculation.

The electrical power consumed by the AHU fan was higher in the cases where the greatest flow rate was required and with the highest recirculation rate, i.e., the higher the pressure drop to overcome. In these cases, the power was around 77 W, reaching a maximum of 79,3 W.

Regarding cooling efficiency or energy efficiency ratio (EER), the prototype reached very with values, with a maximum of 26.69 when the combination of conditions was optimal for higher cooling power with lower power consumption. These values were much higher compared to traditional systems, which are typically between 2 and 4. Also the compactness of the prototype, with a maximum of 176.05 kW/m³, was very high compared to typical equipment, which is typically on the order of 20 kW/m³.

The heat transfer in the equipment reached a high performance, shown by the maximum dew point efficiency, which reached 88%, and by the maximum wet bulb efficiency, which reached 120%, both obtained when the inlet temperature was the lowest, while the humidity, flow rate and recirculation were the highest.

TABLE V.
SUMMARY OF THE MOST FAVORABLE VALUES ACHIEVED

Parameter	Max. value	Tª inlet (ºC)	Tª dew inlet (ºC)	Flow rate inlet (m^3/h)	Recirculation ratio (-)
ΔT (K)	20,90	45,0	7,4	120,5	0,6
$\dot{Q}_{enf}$ (W)	440,20	45,0	7,4	120,0	0,4
$\dot{W}_{elect}$ (W)	5,73	30,0	7,4	90,5	0,6
EER (-)	26,69	45,0	21,6	90,5	0,4
C (kW/m³)	176,05	45,0	7,4	120,0	0,4
ε_{pr} (-)	0,88	30,0	21,6	120,0	0,6
ε_{bh} (-)	1,20	30,0	21,6	120,0	0,6

Conclusions

After carrying out the necessary activities for the development of this work, it was found that the test bench designed fulfilled the expected goals, as the combination of the selected equipment enabled the required conditions for performing the various tests to be fulfilled.

After all the information gathered, it was seen that the factor that has the greatest influence on the supply air temperature is the inlet temperature, followed, but to a lesser extent, by the recirculation rate, which helps to reduce the temperature the higher its value. Finally, it has been seen that high air humidity has a negative influence on air cooling.

The high cooling power values combined with the low electricity consumptions, i.e., the high EER of the equipment under the conditions observed, as well as the high compactness compared to typical systems, allow to conclude that the equipment studied is a excellent alternative to replace traditional units, especially for applications where there is a high ambient temperature with low humidity. Therefore, its use would be suitable for areas with dry tropical climate, such as Africa, Arabia, Iran, Asia… and similar places with features such as low vegetation, strong winds and high aridity and heat.

Areas of application could cover human and non-human thermal comfort such as building cooling, laboratory conditioning, agricultural storage, etc.

REFERENCES

[1] '• Electricidad: precio medio final España 2010-2022 | Statista'. https://es.statista.com/estadisticas/993787/precio-medio-final-de-la-electricidad-en-espana/ (accessed Jul. 13, 2022).

[2] 'ClimateDashboard-atmospheric-carbon-dioxide-graph-20211004-1400px.jpg | NOAA Climate.gov'. https://www.climate.gov/media/13611 (accessed Jul. 13, 2022).

[3] 'Climate Change: Global Temperature | NOAA Climate.gov'. https://www.climate.gov/news-features/understanding-climate/climate-change-global-temperature (accessed Jul. 13, 2022).

[4]   L. Perez-Lombard, J. Ortiz, and I. R. Maestre, 'The map of energy flow in HVAC systems', *Appl. Energy*, vol. 88, no. 12, pp. 5020–5031, 2011, doi: 10.1016/j.apenergy.2011.07.003.

[5]   B. Porumb, P. Unguresan, L. F. Tutunaru, A. Şerban, and M. BĂlan, 'A Review of Indirect Evaporative Cooling Technology', *Energy Procedia*, vol. 85, no. November 2015, pp. 461–471, 2016, doi: 10.1016/j.egypro.2015.12.228.

HVAC World
Student Competition
Other Participants' Contribution

Su-Young Jo	Korea
Hye Jin Cho	

Performance Evaluation of Heat-Pump- Integrated Hollow Fiber Membrane Humidification System

Su-Young Jo, Hye-Jin Cho, Jae-Weon Jeong*

*Department of Architectural Engineering, College of Engineering, Hanyang University, Seoul 04763, Republic of Korea (E-mail : *jjwarc@hanyang.ac.kr*)

Abstract— **A heat pump, considered a carbon-neutral core technology by the International Energy Agency, is a system for cooling and heating a room by absorbing heat from a low-temperature heat source. However, when heating using a heat pump, the supply air gradually dries out because only the indoor air temperature is being raised and recirculated. According to the American Society of Heating, Refrigerating, and Air Conditioning Engineers, maintaining the indoor humidity at 40–60% can reduce the risk of infection in indoor air; in winter, 22 °C and 45–50% are recommended as the indoor temperature and humidity specifications, respectively. In the case of conventional humidifiers, as water or steam is directly sprayed into the air, various air pollution problems can occur. Therefore, this study proposed a hollow-fiber-membrane-based humidification system for a heat pump and tested a prototype of a heating-integrated hollow fiber membrane humidification system. The results obtained indicated that the average humidification amount of the proposed system was 0.52 kg/h, with sensible and latent heat efficiencies of 81.0% and 37.2%, respectively. Importantly, the proposed system shows an approximately 1.4-fold higher humidification performance (438 mL/h) compared to the average humidification amount (320 mL/h) provided by commercial humidifiers. In addition, contamination by water is avoided, with the system exhibiting efficient thermodynamic behavior when integrated with heating equipment. Thus, the heat pump heating-integrated hollow fiber membrane humidification system proposed herein is expected to improve the indoor air environment and air quality in winter by overcoming the major issues in indoor air quality in the post-COVID era.**

Index Terms—**Humidifier, Hollow fiber membrane, Experiment, Integrated system, Sensible and latent effectiveness.**

Introduction

A heat pump—a system for cooling and heating a room by absorbing heat from a low-temperature heat source—is recognized as an energy technology that can provide significant CO2 emission reduction effects with a single device. In addition, the heat pump directly sends refrigerant from one outdoor unit to multiple indoor units installed in each air conditioning space, enabling indoor cooling and heating. With strengthening carbon-neutral national policies on the use of fossil fuels, the use of electric heat pumps is increasing. Correspondingly, heat pumps are considered a carbon-neutral core technology in the energy technology prospects of the International Energy Agency [1]. Unlike central air conditioning, when heating using a heat pump, only indoor air temperature is raised and recirculated. However, a problem exists in that the supplied air becomes drier. According to a survey conducted on occupants of buildings with installed heat pumps, more than 85% of all occupants answered that the room was dry [2].

As occupants are generally active in indoor spaces, a relative humidity of 40–60% is recommended because the activity rate of various viruses or molds varies depending on the humidity. Moreover, the indoor environment directly affects respiratory and skin diseases of the human body, with maintaining proper indoor humidity further emphasized during the spread of COVID-19. According to the American Society of Heating, Refrigerating, and Air Conditioning Engineers (ASHRAE), maintaining indoor humidity at 40–60% can reduce infectious particles in the indoor air; in winter, classroom conditions of 22 °C and 45–50% are recommended [3, 4]. In addition, according to the European Center for Disease Prevention and Control, in the context of COVID-19, heating, ventilation, and air conditioning systems with a relative humidity of 40–60% can help prevent the spread of the SARS-CoV-2 virus in an isolated indoor space. Given the above considerations, it is necessary to consider facilities for maintaining humidity in the design of air conditioning systems [5]. In general, humidifiers are used in buildings to increase indoor humidity in winter. However, existing humidifiers lead to problems such as air pollution by water because water or steam is directly sprayed into the air [6]. In addition, as a humidifier must be used separately from the room heater, it is difficult to respond to the humidification load required for a room.

In the HVAC field, little research has been done on using hollow fiber membranes for humidification. The following are previous studies on membranes of the air-to-liquid type. Cross-flow hollow fiber membrane contactor air humidification/dehumidification processes were studied experimentally and theoretically by Bergero and Chiari [7]. A computer model was developed to analyze the mass and heat movement across the membrane, and the results of the model were compared with the experimental results. The results showed that the model predictions matched the experimental results well, but there were some discrepancies. To determine the cause of these discrepancies, the authors conducted further experiments and analysis. The results of these experiments indicated that the discrepancies were caused by the pressure drop across the membrane, the temperature of the air in contact with the membrane, and the properties of the membrane material. As a result, Bergero and Chiari were able to refine their computer model and improve its accuracy. A comprehensive two-dimensional transient model is used to investigate the effects of membrane properties on the

effectiveness of hydrophobic membrane humidification /dehumidification processes. Experimentally and numerically, the effects of the hollow fiber membrane humidification module's parameters were evaluated and confirmed. In a study conducted by Zhang et al. [8], it was found that membrane properties and operating conditions affect the mechanisms for mass transfer within membrane pores. In conclusion, previous research on hollow fiber membranes has concentrated on performance enhancement of the materials or heat and mass transfer analysis. There need to be more studies on the characteristics of indoor behavior or the potential for energy reduction when the hollow fiber membrane humidification system is used in a building.

Therefore, in this study, a hollow-fiber-membrane-based humidification system applicable to a heat pump heating system was proposed and a prototype of the system was tested, with the test bed for the proposed system built in a laboratory in the Hanyang University Science and Technology Building. An air temperature and humidity sensor and flow sensor were installed to experimentally evaluate the thermal behavior characteristics of the air and the effectiveness of the sensible and latent heat.

System Overview

The proposed heat pump heating-integrated hollow fiber membrane humidification system consists of 1) a heat pump for heating indoor air using the condensation heat and heat of the refrigerant and 2) a membrane humidifier with a hollow fiber membrane (Figure 1). A prototype test was conducted before designing the entire system, with the heat pump heating part replaced with a positive temperature coefficient electric heater.

A heat pump uses the phase change reaction of a refrigerant to absorb indoor heat and release it outdoors to cool a room in summer or to heat the room by absorbing outdoor heat and discharging it into the room in winter. During heating, the indoor air passes through an evaporator and exchanges heat with the evaporation heat of the refrigerant, increasing the temperature (Figure 2) [9].

The humidification system proposed herein is based on a cylindrical hollow fiber membrane coated with a hydrophilic polymer. Water is supplied to the shell side inside the hollow fiber membrane, while indoor dry air is supplied to the tube side outside the hollow fiber membrane, enabling heat and material exchange across the hollow fiber membrane. At this time, in the hollow fiber membrane, moisture from the water with a relatively high vapor pressure moves to the air side owing to the difference in the vapor partial pressure between the water and air, thereby increasing the absolute humidity of the air (Figure 3).
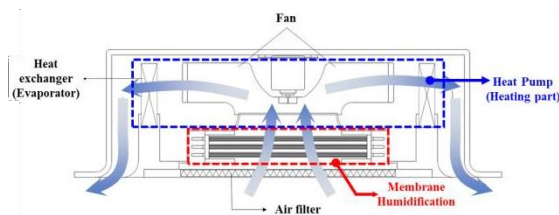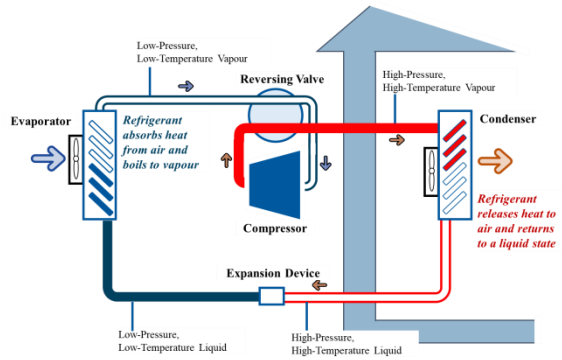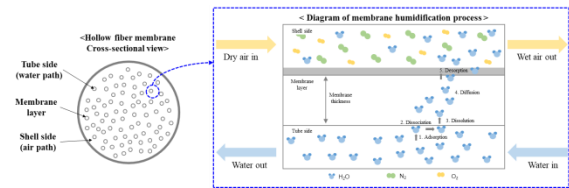

Figure 2. Schematic diagram of a heat pump

Figure 3. Cross-sectional view of the hollow fiber membrane and schematic diagram of the humidification process

As a result of humidification, the air temperature, and absolute humidity are determined using Equations (1) and (2). The temperature of the circulating water is determined using Equation (3) [10]. Equation (1) states that the temperature difference between the two fluids (dry air (T_a) and water (T_w)) affects the air temperature, and equation (2) states that the absolute humidity difference between the two fluids (dry air (ω_a) and water (ω_w)) affects the air temperature. In order to calculate the water temperature (Equation 3), the latent heat of vaporization of the flowing moisture and the temperature differential between the two fluids (water and dry air) must be considered. Considering that the amount of water lost from the circulating water flow is less than 1%, the temperature change resulting from moisture evaporation's latent heat is not considered. Consequently, variations in air and water mass flow rates are disregarded.

$$\frac{dT_a}{dx^*} = NTU_{sen}(T_w - T_a) \tag{1}$$

$$\frac{d\omega_a}{dx^*} = NTU_{lat}(\omega_w - \omega_a) \tag{2}$$

$$\frac{dT_w}{dx^*} = m^*{}_{sen}NTU_{sen}(T_w - T_a) + m^*{}_{lat}NTU_{lat}(T_w - T_a) \tag{3}$$

A humidification system based on a hollow fiber membrane differs from conventional humidifiers in that no water contamination problem occurs during humidification because water and air are not directly exchanged; moreover, no additional heat source (heating) is required. The humidification mechanism of the hollow fiber membrane has been confirmed through previous studies [11]. As described fallow, the performance of the proposed

Figure 1. Schematic diagram of the proposed system

integrated air conditioning system, comprising the heating system and humidification technology, was experimentally evaluated.

Experiment

The prototype test of the proposed system was conducted in a laboratory in the Hanyang University Science and Technology Building. As shown in Figure 4, the proposed system was largely divided into a membrane humidifier and heat pump heating unit, with indoor air conditions (20 °C, 50%, 0.065–0.075 kg/kg) created using a thermo-hygrostat chamber to control the inlet air. In addition, 20 °C water was obtained using a chiller to control the temperature of the water supplied to the humidifier. The room air was humidified by the membrane and then heated through the heat exchanger. The proposed all-in-one system prototype was configured such that the heating part was located at the rear end of the humidifying part, as shown in Figure 4.
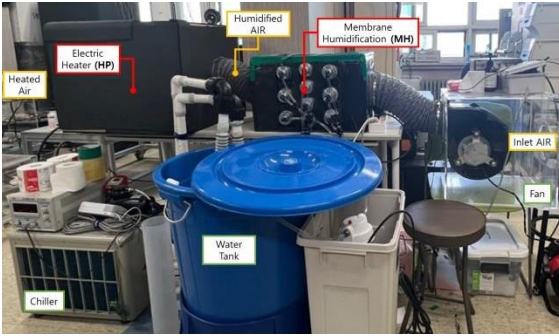
Figure 4.   Experimental setup

The system size of the humidifier in this study was 340 (W) × 330 (H) × 500 mm (L) and consisted of 10 modules with 220 strands per module. The inner diameter of the hollow fiber membrane used in the module was 0.85 mm, the outer diameter was 1.05 mm, and the effective contact area per module was 1.43 m². The system size of the heating part was 200 (W) × 215 (H) × 165 mm (L). A 2- kW capacity was calculated to satisfy the supply target temperature of 40 °C. Therefore, the final supply air temperature supplied to the room through the heat pump heater was set at 40 °C (±1.0), with indoor air conditions in winter set at 20 °C and 50% humidity (0.065–0.075 kg/kg) (Table I).

To evaluate the heating and humidification performance of the proposed system, the performance indices were selected from the humidification rate ($\dot{m}_{hum}$), sensible heat effectiveness (η_{sen}) and latent heat effectiveness (η_{lat}), respectively, as shown in Equations (4)–(6). The measurement device specifications shown in Table II were used to measure the variables of each evaluation index. Figure 5 shows each measurement point. In this case, we calculated the absolute humidity of water ($w_{w.eq}$) using the saturated absolute humidity of air ($w_{a.sat}$) at the same temperature as the water. The saturation pressure (P_{sat}) is the partial pressure of water vapor in saturated air. Using the relative humidity (RH) and saturation pressure (P_{sat}), the vapor pressure (P_v) can be calculated. The pressure of

saturated air at 100% relative humidity is equal to the vapor pressure of water.

$$\dot{m}_{hum} = \dot{V}_{a.in} \times (w_{a.out} - w_{a.in}) \qquad (4)$$

$$\eta_{sen} = (T_{a.out} - T_{a.in})/(T_h - T_{a.in}) \qquad (5)$$

$$\eta_{lat} = (w_{a.humid} - w_{a.in})/(w_{w.eq} - w_{a.in}) \qquad (6)$$

TABLE I.
PROTOTYPE SPECIFICATIONS.

	System size [mm]	340 (W) × 330 (H) × 500(L)
Mem brane humi difier (MH)	Membrane type (material)	Dense membrane (Polysulfone)
	Fiber inner diameter (ID) [mm]	0.85 mm
	Fiber outer diameter (OD) [mm]	1.05 mm
	Number of fibers [EA]	220 EA
	Number of modules [EA]	10 EA
	Effective contact area [㎡]	14.3 ㎡ (inner diameter)
Heat pump (HP)	System size [mm]	200 (W) × 215 (H) × 165 (L)
	Capacity [kW]	2.0 kW
	Target air temperature [°C]	40 °C (±1.0)
Inlet	Supply airflow rate [CMH]	150 ㎥/h
	Inlet air temperature [°C] and Relative humidity [%]	20 °C, 50% (0.065–0.075kg/kg)
	Supply water temperature [°C]	20 °C (±1.0)

TABLE II.
MEASURING DEVICE SPECIFICATIONS.

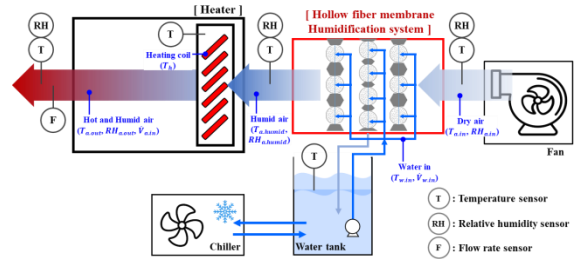| Parameter	Type	Range	Accuracy
Air temperature and humidity	Negative temperature coefficient of resistance	-20–60 °C 0%–100%	±0.5 °C ±2.0%
Air flow rate	Vane probe Ø 100 mm	0.1–15 m/s	±0.1+15 % of mv
Water temperature	Thermocouple type K	-50–400 °C	±1.0 °C
Water flow rate	LZT panel flow meter	5–50 L/min	±4.0%

Figure 5.   Schematic diagram of measuring sensor positions

Results and discussion

An uncertainty analysis, based on the method proposed by ASHRAE [12], was performed on the measured parameters and performance indicators of the experimental data. The total uncertainty (U_y) of the measurement data

was estimated using the propagation of the error (B_y) and random error (S_y) (Equations (7)–(9)). The propagation of the error was estimated using a fixed error for each variable (b_{x_i}) calculated by multiplying the sensor accuracy and standard deviations of the measurements. In contrast, the random error (S_y) was evaluated using the standard deviation of the measured data ($S_{(N)}$) and number of data sets (N). The total uncertainty values for the measured variables and performance indicators are presented in Table III. The uncertainty value for the absolute humidity was calculated based on a relative humidity indicator used in the sensor. The uncertainty of all variables satisfied a maximum of 5% because the experimental conditions remained stable during the measurements.

$$U_y = \sqrt{\overline{B_y^2 + S_y^2}} \tag{7}$$

$$B_y = \sqrt{\overline{\{\sum_{i=1}^{j}(\frac{\partial y}{\partial z_i} \cdot b_{x_i})^2\}}} \tag{8}$$

$$S_y = \frac{2 \cdot S_{(N)}}{\sqrt{N}} \tag{9}$$

TABLE III.
OVERALL UNCERTAINTY.

Parameter		Uncertainty [%]
Measured	$T_{a.in}$ [°C]	0.51
	$RH_{a.in}$ [%]	0.04
	$T_{a.humid}$ [°C]	0.14
	$RH_{a.humid}$ [%]	0.04
	$T_{a.out}$ [°C]	0.25
	$RH_{a.out}$ [%]	0.05
	$T_{w.in}$ [°C]	0.23
	T_h [°C]	1.47
	$\dot{V}_{a.in}$ [m^3/h]	0.17
	$\dot{V}_{w.in}$ [L/min]	0.97
Calculated	$\dot{m}_{hum}$ [kg/h]	0.02
	η_{sen} [%]	0.02
	η_{lat} [%]	0.01

As a result of the experiment, the average humidification amount ($\dot{m}_{hum}$) of the proposed system is 0.52 kg/h; the sensible heat effectiveness (η_{sen}) and latent heat effectiveness (η_{lat}) are 81.0% and 37.2%, respectively. Figure 6 shows the main thermal performance of the proposed system with integrated humidification and heating. As the water and inlet air temperatures are the same, only absolute humidity increases without a temperature change during humidification, with the humidified air heated up to 40 °C by the heater.

The reference system uses a heat pump and separate humidifier. Figure 7 shows the temperature and humidity behaviors of the air flows in the reference system under the assumption that the inlet, humidification, and outlet air conditions of the proposed system and reference system are

identical. As the target absolute humidity after humidification is the same as that of the proposed system, a similar latent heat effectiveness of $\eta_{lat.avg} = 36.7\%$ is shown. However, as heating and humidification are operated separately, the air temperature decreases during humidification, potentially leading to an increase in the indoor heating load. In addition, as the air flow rate is lower than that of the proposed system, the humidification volume (0.155 kg/h) decreases by 70.2%.
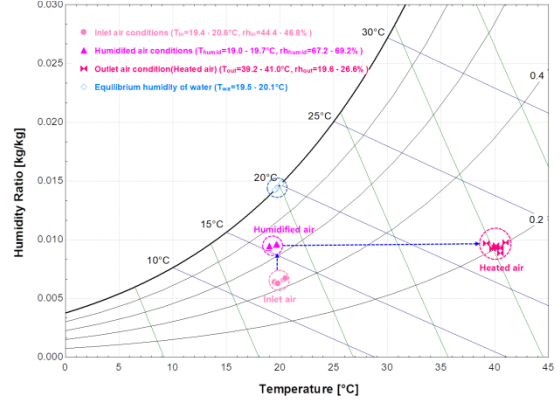

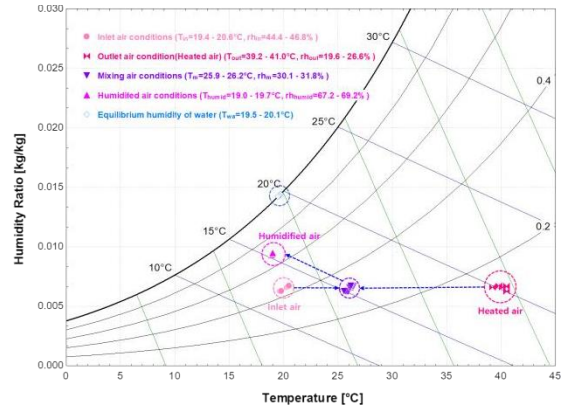Figure 6. Temperature and humidity behaviors of air flows in proposed system

Figure 7. Temperature and humidity behaviors of air flows in reference system

Finally, the humidification amounts of the commercial humidifier and proposed system were compared. The humidifier performances were compared based on the humidifier quality comparison test proposed by the Korea Consumer Agency [13]. As for the types of humidifiers selected here, a total of ten products were evaluated: eight natural evaporation types and two ultrasonic types. Figure 8 shows the results from the comparison of the humidification amounts (mL/h). The humidification performance of the proposed humidifier ranks third among the product groups, with a 1.4 times higher humidification amount than the average.
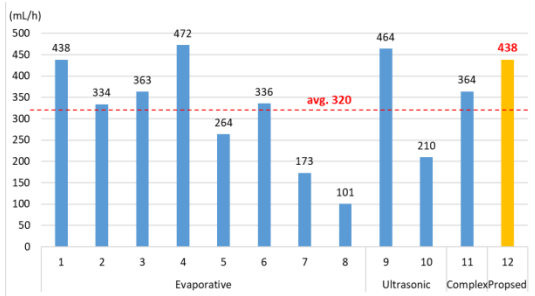
Figure 8.   Humidification amount comparison by humidifier

Conclusion

In this study, we fabricated a prototype of an integrated indoor humidification and heating system combining a heat pump heating system and hollow fiber membrane humidifier. A test bed was established to experimentally verify the thermal behavior characteristics of the air and the effectiveness of the sensible and latent heat.

As a result of the experiment, the average humidification amount of the proposed system was 0.52 kg/h and the sensible heat effectiveness and latent heat effectiveness were 81.0% and 37.2%, respectively. In addition, unlike existing humidifiers, the proposed system did not affect the reduction of indoor sensible heat load because it was integrated with the indoor heating system.

The proposed system exhibits a humidification amount (438 mL/h) approximately 1.4 times higher than the average humidification amount (320 mL/h) of individual humidifiers in use but does not have a water contamination problem.

The heat pump heating-integrated hollow fiber membrane humidification system proposed herein is expected to contribute to improving the indoor air environment and air quality in winter by overcoming the major issues in indoor air quality in the post-COVID-19 era using this new hollow fiber membrane technology.

References

1   International Energy Agency (IEA), World Energy Outlook 2022, 2022.

2   Y. Young Kwon, K. In Sung, C. Min Hee, M. Jin Woo, P. Jin Chul, " The Field Survey of Indoor Environment of the Office Building," *Korea Institute of Ecological Architecture and Environment (KIEAE) Journal,* vol. *16*, no. 3, 2016, pp. 71–76.

3   K B Washington, "ASHRAE Epidemic Task Force Releases Updated Building Readiness Guide," *American Society of Heating, Refrigerating and Air-Conditioning Engineers (ASHRAE) Journal,* 2022.

4   S Simmons, "ASHRAE Introduces Updated Reopening Guide for Schools and Universities," *American Society of Heating, Refrigerating and Air-Conditioning Engineers (ASHRAE) Journal,* 2020.

5   European Centre for Disease Prevention and Control (ECDC), Heating, ventilation and air-conditioning systems in the context of COVID-19: first update, 2020.

6   J Nam-Soon, "The Review on status of chemical safety management policies and limits through humidifier disinfectants accident," *Environmental Law and Policy (Env.L.P.),* vol. *11*, 2013, pp. 35–56.

7   Bergero, Stefano, and Anna Chiari. "Experimental and theoretical analysis of air humidification/dehumidification processes using hydrophobic capillary contactors." *Applied Thermal Engineering* 21, no. 11 (2001): 1119-1135.

8   Zhang, Li-Zhi. "Mass diffusion in a hydrophobic membrane humidification/dehumidification process: the effects of membrane characteristics." *Separation science and technology 41*, no. 8, 2006, pp. 1565-1582.

9   ENERGY STAR announcements, Heating and Cooling With a Heat Pump, modified 2022-08-09

10 Zhang, Li-Zhi, and Si-Min Huang. "Coupled heat and mass transfer in a counter flow hollow fiber membrane module for air humidification." *International Journal of Heat and Mass Transfer* 54, no. 5-6, 2011, pp. 1055-1063.

11 Jo, Su-Young, Hye-Jin Cho, and Jae-Weon Jeong. "Humidification performance of hollow-fiber membrane humidifier for air-conditioning applications." *Applied Thermal Engineering* 226, 2023

12 American Society of Heating, Refrigerating and Air-Conditioning Engineers (ASHRAE), Engineering Analysis of Experimental Data, ASHRAE Guideline 2-2010.

13 Korea Consumer Agency, Humidifier quality comparison test, 2.

REHVA
Student Competition
Other Participants' Contribution

Alzbeta Svobodova	Czec Republic
Aurore Toulou	France
Dună Andrei	Romania
Diana Țucu	
Yangmin Wang	Finland
Novak Popović	Serbia
Giulia Torriani	Italy
Sofia Vasman	Estonia

The Influence of Frost Formation on the Performance of Air-to-air Heat Exchanger

Alžběta Svobodová[1], Daniel Adamovský[2]

[1,2] Department of Indoor Environmental and Building Services, Faculty of Civil Engineering, Czech Technical University in Prague; Thákurova 7/2077, 166 29 Prague, Czech Republic

[1,2] Czech Technical University in Prague - University Centre for Energy Efficient Buildings; Třinecká 1024, 273 43 Buštěhrad

Abstract—**The subject of this paper is the experimental evaluation of the influence of frosting on the performance of a air-to-air heat exchanger used in ventilation, especially in relation to temperature, humidity and other changes. The presence of frost has a negative effect on the exchanger's ability to recover heat and, in extreme cases, can even do considerable damage because of the ice's large volume. Manufacturers generally address this problem with preventative measures, but these can result in a reduction of energy savings achieved by using a heat recovery exchanger in the first place. From the point of view of sustainable development, it is important to address this issue to maximize the energy-saving potential of heat recovery exchangers.**

A series of experimental measurements were performed using an enthalpy plate counter-current heat exchanger. First, the properties of the heat exchanger for standardized conditions, especially temperature and humidity conditions and internal leaks, were determined. The heat exchanger was then subjected to several frosting cycles. For each cycle, air temperature, relative humidity, air flow rate and static pressure difference were measured, and the obtained data were subsequently evaluated. Changes caused by the presence of ice were also monitored visually in real time using a camera probe. From the measured data, the possibilities of frosting detection were derived for the given exchanger, such as change in effectiveness and pressure difference across the exchanger, which were then compared with the methods reported in the literature. It is concluded that the method using change in effectiveness is the most reliable along with the visual detection method.

Index Terms— **enthalpy plate heat exchanger, experimental measurement, frosting, heat recovery**

Introduction

Heat recovery ventilation is currently an integral part of most residential ventilation systems. Use of heat recovery exchangers helps to significantly reduce the amount of energy that buildings consume. They allow the heat to be recovered from the extracted warm air, that would otherwise go unused, and subsequently pass it on to the outdoor air. In connection with heat exchangers in air handling systems, it is possible to encounter condensation of water vapor and the potential consequent formation of frost. This topic is significant because the frosting inside the heat exchanger has a negative effect on its operation. Not only does the presence of frost reduce the ability to recover heat, but in an extreme case it can also damage the heat exchanger, especially if large amounts of ice are produced.

Manufacturers often address the problem of frost formation with preventative measures, but this can result in a reduction of the energy savings that are achieved by using a heat exchanger for heat recovery in the first place. Therefore, it is important to know the boundary conditions for which frost is most likely to occur and apply them in practice. By doing so, premature initiation of preventative measures can be avoided, and the heat exchanger is used to the maximum.

Formation of frost in a heat exchanger

The use of heat exchangers significantly reduces the energy needed to heat up outdoor air to the required temperature. However, winter months bring the risk of condensation of water vapor inside the heat exchanger and the possible subsequent formation of frost. The combination of lower temperature of outdoor air and increased humidity in warm indoor air increases the risk of condensation. If the temperature of outdoor air drops even lower, there is a high risk of frost formation on the inside of the heat exchanger. The resulting presence of ice can result in pressure loss across the heat exchanger due to partial or complete blockage of the internal pathways and thus an increase in the required fan power to maintain the desired airflow. The risk of frost formation also depends on the type and design of the heat exchanger and whether it is able to transfer primarily sensible or latent heat. The material properties of the membrane inside the heat exchanger also play an important role, for example its ability to transmit water vapor. The more vapor can be transmitted, the lower is the risk of frost formation. [1]

If the material bypassed by the two air streams is covered by a layer of ice, its thermal resistance increases, reducing its ability to transfer heat between the air streams. The greater the thickness of the ice layer, the higher is the thermal resistance of the membrane [2]. Highly efficient heat exchangers are more susceptible to freezing because the transfer of heat energy between the two air streams is so effective that the temperature of the exhaust air drops lower than with a less efficient exchanger. Therefore, frost forms at higher outdoor air temperatures than using a less efficient exchanger [3].

The properties of the resulting ice layer, such as the density or thickness of the layer, are influenced by the inner surface temperature, indoor air temperature and indoor air relative humidity. A lower surface temperature will cause the ice layer to be more porous and therefore less dense. In this case the ice grows faster, and the layer is not as uniform as it would be at a higher temperature surface where the

growth of frost is slower [2]. It is important to have an idea of where frost is most likely to occur. Consensus on the location of frost in different types of heat exchanger has not yet been reached due to the limited number of publications on this topic. However, the exit of the already cooled exhaust air is considered as the most critical location in a plate heat exchanger. In this area the frost is generally first formed near the outdoor air inlet. This area is often referred to as the "cold corner" [4].

Several methods of frost detection exist. Visual inspection is by many considered as the most reliable way to detect the presence of frost. This method of detection is, however, unsuitable for normal operation. The visual state of the heat exchanger needs to be continuously monitored - either by artificial intelligence or by a human factor. Therefore, continuous measurement and evaluation of the pressure loss across the heat exchanger is mainly used and is considered to be relatively reliable. In the presence of frost on the heat transfer surface, the pressure drop increases while maintaining the air flow. However, by the time a large pressure drop is detected, the ice layer is already thick, and requires a significant amount of energy to melt it. [1]

The absolute humidity difference between indoor and exhaust air can also be monitored and if an increasing difference in humidity, while maintaining the same interior boundary conditions, is found, it can indicate the presence of frost. Even more accurate detection is achieved when combined with measurement of pressure drop across the heat exchanger. [5]

Methods

All measurements were performed on a test line in the Indoor environment laboratory at the University Centre for Energy Efficient Buildings CTU in Prague. The test line consists of two air handling units with which the desired air properties have been achieved. The properties at the exhaust of the units were continuously monitored using a combined humidity and temperature sensor, air flow velocity was measured using a hot-wire anemometer.

For the measurements, a crossflow plate energy exchanger with a membrane permeable to moisture was chosen. Several temperature and humidity sensors were available, as well as vane anemometers, unfortunately most of them were not regularly calibrated. To get closer to the real values, the measured values were compared with values from a calibrated sensor. For each sensor, an equation was found to convert the measurements of the uncalibrated sensors to a value that is closer to reality.

The selected heat exchanger was connected to the test line using custom 3D printed parts. To transfer the air prepared in the air handling units to the heat exchanger, a plastic pipe with a nominal diameter of 100 mm with a length of at least 1,2 m was used, in order to comply with the requirement for a straight pipe length in front of and behind the air flow measurement point of the vane anemometer. The supply pipe was fitted with polyethylene foam insulation to reduce heat loss in the warm air stream and heat gain in the cold air stream. The location of the sensors can be seen on Fig. 1 below. Temperature and moisture transfer efficiency were determined according to Czech technical standard ČSN EN 308 [6], the air flow rate was determined according to ČSN EN 16211 [7].

Data Presentation and Discussion

The initial properties of the measured exchanger were investigated, such as temperature and moisture transfer efficiency for different air volume flow rates (approximately from 35 m³/h to 75 m³/h), and internal air leakage (the magnitude of the mass flow rate which, under the conditions of [6], is blown from one air stream passing through the heat exchanger into another).

Frost begins to form inside the heat exchanger when the temperature of the internal surface drops below the freezing point of water, and the surrounding air contains water vapor. The amount of formed ice also depends on the temperature and humidity properties of the cooled air stream. It was anticipated that most of the frost would form in the part of the heat exchanger where the already cooled exhaust air exits. It was also assumed that there would be a visible increase in differential pressure during ice formation, with which the onset of frosting could be detected. Furthermore, the assumption was that it would be possible to detect water vapor condensation and subsequent frost formation visually by capturing the state of the exhaust air outlet with an endoscopic video camera.

The experiment consisted of several measurements for different boundary conditions. The temperature of the outdoor air during the measurement ranged from approximately - 4 °C to - 7 °C, for indoor air between 20 °C and 25 °C. Relative humidity of indoor air was also controlled, the value was in the range from 30 % to 65 %. Air velocity of both air currents was maintained at 1,8 m/s, which corresponds to a volume flow rate of approximately 50 m3/h. Air temperature, relative humidity, air velocity and static pressure difference were measured according to the schematic diagram in Fig. 1.
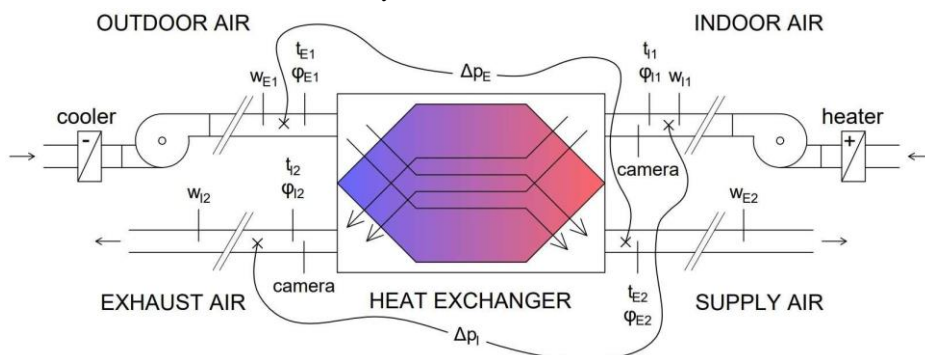
Figure 1. Schematic diagram of the measurement setup. (t) Air temperature. (φ) Relative humidity. (w) Air velocity. (Δp) Static pressure difference

Frost formed in the form of small ice crystals in the pathways of the heat exchanger, but more often the water vapor condensed first, formed larger droplets, and froze only after. Condensation and frosting did not always occur in the same place for different measurements and within a single measurement it appeared irregularly. Most of the droplets flowed to the lower part of the heat exchanger due to the gravitational force, where the largest amount of frost was formed. However, ice also formed in the upper part on the other side of the heat exchanger where the indoor air inlet is located. The volume of ice formed depended on the humidity content of the indoor air. The higher the humidity, the faster the ice formed and the bigger was the volume.

A. Visual changes

Among the first signs of the presence of frost in the heat exchanger were the reflections of the camera's LED light from the condensed water vapor on the internal surface. If the current boundary conditions were further maintained, it was possible to observe the water droplets enlarging and eventually moving downwards due to the gravitational force. The gradual growth of ice in the channels of the exchanger can also be observed in Fig. 3. The frost and condensate formed simultaneously, probably due to the turbulent air flow inside the exchanger, which causes the temperature of the plates to be different at all points.

The camera used was not small enough to be inserted into the channels inside the heat exchanger and due to this fact, it was only possible to monitor the state from the outside. Therefore, the visual method could only detect larger changes, which only appear when the frost is already widespread to the exhaust part of the exchanger. The determination of the onset of frost formation by this method is indicative, but because the exchanger being measured is relatively small and the frost spreads within a few minutes, it can be used as an estimate.

B. Air velocity and static pressure difference

Air flow of the required velocity was provided by fans in the air handling units of the test line. They were controlled by revolutions per minute, that remained constant during the measurements. It was assumed that the pressure difference would increase significantly with the spreading of the frost and thus the onset of frosting could be detected. However, the measured data show that the differential pressure does increase, but to a lesser extent than expected. This is probably because the air velocity decreased at the same time as the frost spread. If the fan speed was variable and it maintained a constant airflow, the flow rate would not change, and the pressure difference would probably increase more significantly.

Fig. 2 compares the static pressure difference for three measurements with different boundary conditions. During the measurement Z1 no frost was formed in the exchanger, therefore the pressure difference is approximately constant. In the other two measurements (Z3 and Z4) condensation and subsequent freezing of water were observed, differing from each other by the amount of moisture contained in the indoor air. The absolute humidity of indoor air was highest in measurement Z4, this resulted in greater increase in the pressure difference.
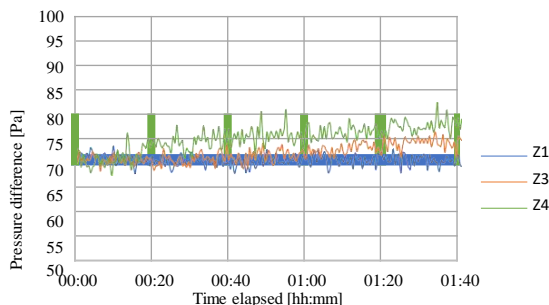

Figure 2. Chart comparing pressure difference changes in time for different boundary conditions of indoor air

C. Temperature and humidity changes

With the presence of frost on the inner membrane, changes in the temperature difference across the heat exchanger can also be observed. Since ice acts as an insulator, it reduces the efficiency of heat transfer. As frost develops, the exhaust air temperature will decrease (without changing the properties of indoor or outdoor air) because it will not receive as much heat as it would under normal conditions. Therefore, the difference between the temperatures of indoor and exhaust air increase in time.

A similar situation occurs when measuring absolute humidity. Since some of the water vapor remains inside the channels in the form of frost, it can be assumed that the difference in absolute humidity between indoor and exhaust air stream will gradually increase with increased frost production, while the difference between outdoor and supply will vary only slightly. The membrane between air streams is blocked by a layer of ice and is unable to transfer as much moisture.

The indoor air stream cannot transfer as much vapor to the outdoor air stream, which further contributes to an increase in the absolute humidity difference. Therefore, the indoor air humidity does not decrease as usual which furthermore contributes to the formation of frost.

Figure 3. The process of frost formation inside the measured heat exchanger

D. Changes in efficiency

Because the ice acts as an insulator, the amount of heat transferred between air streams is reduced with its presence. Therefore, the temperature transfer efficiency of the heat exchanger also decreases. However, the exact onset of frost formation cannot be determined from the immediate efficiency alone. There is no significant break in the time course of efficiency that would indicate the exact onset (see Fig. 4). Its value fluctuates over time, and it is impossible to determine when it moves out of the interval bounded by the measurement uncertainty.
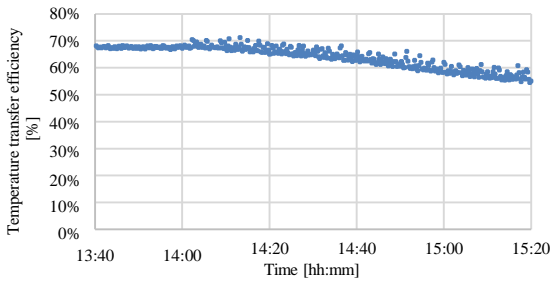
Figure 4. Change of temperature transfer efficiency in time

Hence, the method of converting the raw values of temperature transfer efficiency to standard score was used [8]. For steady air condition without frost, a temperature transfer efficiency was determined for which the measurement uncertainty was calculated. The standardized variable is then determined by the equation

$$\Phi_S = \frac{\Phi_{i,j} - \Phi_i}{u_i}. \tag{1}$$

The standard score equation. (Φ_S) Standardised temperature transfer efficiency [-]. ($\Phi_{i,j}$) Temperature transfer efficiency for the immediate state of the air [%]. (Φ_i) Temperature transfer efficiency for the steady state without frost [%]. (u_i) Measurement uncertainty of the temperature transfer efficiency [%].

When an immediate value of the temperature transfer efficiency is equal to the steady state value (state without the presence of frost), the standardized temperature transfer efficiency equals 0. When its value is greater than 1 (or less than -1), the immediate temperature ratio has left the interval bounded by the measurement uncertainty, and therefore frost related changes are most likely occurring in the heat exchanger. This is shown in orange in Fig. 5. The changes were then detected visually using an endoscopic camera with a ten-minute delay.
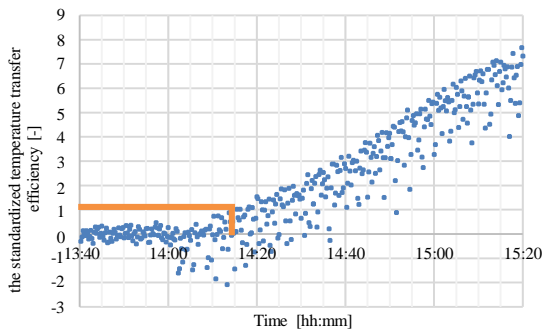

Figure 5. Time course of the standardized temperature transfer efficiency. The boundary where the uncertainty bounded interval is crossed is marked in orange.

Conclusions

There are several different methods of detecting frost in a heat exchanger. Visual inspection is generally considered a reliable method of detection, and this assumption has been confirmed in the experiment. Problems arise when only a small amount of frost forms or when it first forms inside the heat exchanger and only spreads into the camera's field of view after a certain period. As a rule, it was only possible to detect the first visual changes after a larger amount of frost formed. Nevertheless, this method was found to be more accurate than monitoring the static pressure drop. The static pressure difference method is best used in cases where the fans of the air handling units operate at variable speeds and maintain a constant flow rate through the heat exchanger. If the fan speed is constant, the flow velocity decreases as the amount of frost increases, and the increase in pressure differential is not noticeable in many cases.

From the obtained data, the method of standardizing the temperature transfer efficiency seems to be the most accurate. However, it is preceded by a rather complex calculation, especially the calculation of measurement uncertainties, and it is not very practical to apply this method in routine practice.

Alternatively, humidity-related changes, such as condensation or frost formation, could be monitored by taking continuous absolute humidity readings and observing changes in the difference between indoor and exhaust air streams. If the difference in the absolute humidity of the indoor and exhaust air stream increases over time, it can be concluded that condensation or possible freezing of water vapor is taking place. In combination with monitoring of the outdoor air temperature, it can be estimated whether frost formation is occurring.

Freezing in the heat exchanger in heat recovery is a still developing topic that can lead to further opportunities for saving energy. If boundary conditions, at which there is a high probability of frost formation, were specified by the manufacturer for each heat exchanger sold, frosting could be better prevented and there would be no need for the use of defrosting methods. Further research is still needed to make the use of heat exchangers more effective in practice.

REFERENCES

1 Rafati Nasr, Mohammad, Melanie Fauchoux, Robert Besant and Carey Simonson. A Review of Frosting in Air-to-air Energy Exchangers. Renewable and Sustainable Energy Reviews [online]. 2014, 30, 538-554 [cit. 2021-03-30]. ISSN 13640321. Available at: doi:10.1016/j.rser.2013.10.038

2 Bilodeau, S., P. Brousseau, M. Lacroix and Y. Mercadier. Frost Formation in Rotary Heat and Moisture Exchangers. International Journal of Heat and Mass Transfer [online]. 1999, 42(14), 2605-2619 [cit. 2021-03-30]. ISSN 00179310. Available at: doi:10.1016/S0017-9310(98)00323-8

3 Phillips, E. G. et al. A Model to Compare Freezing Control Strategies for Residential Air-to-Air Heat Recovery Ventilators. ASHRAE Journal. 1989, 95(2), 475-483. ISSN 0001-2505.

4 Liu, Peng et al. A theoretical model to predict frosting limits in cross-flow air-to-air flat plate heat/energy exchangers. Energy and

Buildings [online]. 2016, 110, 404-414 [cit. 2022-04-10]. ISSN 03787788. Available at: doi:10.1016/j.enbuild.2015.11.007

5   Anisimov, Sergey, Andrzej Jedlikowski and Demis Pandelidis. Frost formation in the cross-flow plate heat exchanger for energy recovery. International Journal of Heat and Mass Transfer [online]. 2015, 90, 201-217 [cit. 2022-04-02]. ISSN 00179310. Available at: doi:10.1016/j.ijheatmasstransfer.2015.06.056

6   ČSN EN 308. Výměníky tepla - Metody zkoušek pro ověření výkonnosti zařízení pro regeneraci tepla. 1. Praha: Úřad pro technickou normalizaci, metrologii a státní zkušebnictví, 1998, 20 s. Třídící znak 696308

7   ČSN EN 16211. Větrání budov - Provozní měření průtoku vzduchu - Metody. 1. Praha: Úřad pro technickou normalizaci, metrologii a státní zkušebnictví, 2016, 36 s. Třídící znak 127132

8   Z-Score: Definition, Formula and Calculation. (2022). Cit. 2022-11-18, from Statistics: How To: https://www.statisticshowto.com/probability-and-statistics/z-score/

Assessing the outdoor thermal comfort conditions in the Mediterranean climate, A case study in Seville, Spain

Aurore Toulou

Aurore Toulou [1,*], José Sánchez Ramos [2,**], Jean-Jacques Roux [1,***]

[1] CETHIL UMR 5008, Univ. Lyon, INSA Lyon, CNRS, 69621 Villeurbanne, France
[2] Grupo Termotecnia, Escuela Técnica Superior de Ingeniería, Universidad de Sevilla, 41092 Sevilla, Spain

* aurore.toulou@insa-lyon.fr, ** jsr@us.es, *** jean-jacques.roux@insa-lyon.fr

Abstract—Sanitary issues, combined with the effects of climate change, emphasize the comfort of outdoor spaces in cities. Numerous comfort models exist and can predict the state of the occupants of a space. However, these comfort indices need to be validated in Mediterranean climate regions. For this, the present study investigated the outdoor thermal comfort conditions of people living in the Mediterranean climate in Seville, Spain. Theoretical predictions provided by the COMFA thermal comfort model were compared with the subjective responses of the occupants given in the questionnaires of the field campaigns. The field campaigns were associated with on-site monitoring of local climate variables. They were conducted in a primary school where the occupants are mainly children. It was observed that during the survey period, the entire space was predicted uncomfortable by the COMFA model. On the contrary, the results of the questionnaires showed that one third or the respondents felt the space comfortable. Results also highlighted the tendency of the COMFA to overestimate the thermal sensations in an area where people is used to the heat, and thus led to the conclusion of a necessary calibration made specifically for the study space.

Index Terms— Field survey, Outdoor thermal comfort, Thermal sensation, Urban open spaces

1. Introduction

Global change combined with the expansion and densification of cities leads to the development of urban overheating, which impacts the health of populations and causes the progressive desertion of outdoor spaces. In this context, the evaluation of outdoor thermal comfort conditions is a major issue, especially in order to design relevant cooling solutions adapted to their implementation context. According to the American Society of Heating, Refrigerating and Air Conditioning Engineers (ASHRAE), human thermal comfort is a state of mind that expresses satisfaction with a thermal environment. While some factors are objective and measurable (climatic, personal, and environmental variables), others are subjective and depend on behavioral, physiological, and psychological adaptation.

This plurality of factors has led to the development of numerous thermal comfort models, which are distinguished primarily by the approach taken, i.e. physical, physiological, or psychological. Most studies investigating outdoor spaces use physiological models based on the human energy balance equation. While these theoretical models are rarely cross-referenced with field campaigns, several studies have demonstrated the variability of thermal comfort scales in different regions of the world [5, 12], which can be explained by differences in urban typo-morphologies, usage practices, or stress levels of populations. The challenge of assessing outdoor thermal comfort is thus to adapt the comfort model used to the space studied.

COMFA is a physiologically based thermal comfort model developed by Brown and Gillespie [3], which consists of calculating the heat load that must be brought or dissipated from the body to be in the comfort zone. Although its validity and usefulness have been demonstrated by several authors, such as Kenny et al. [6, 7] and Xie et al. [13], its applicability in different regions of the world remains to be evaluated. With a climate marked by hot and dry summers, increasingly frequent and intense heat waves, and a historical culture of "living outside", the city of Seville was a relevant case study for assessing the applicability of the COMFA model in the Mediterranean climate.

58

2. Materials and Methods

2.1. Description of the study area

The present study investigated the outdoor space of the Colegio de Educación Infantil y Primaria Arias Montano located in the urban center of Seville, Andalusia, Spain. The school is composed by three independent buildings, surrounded by a large courtyard which was the study area. This one counts an open-air space at the entrance and a huge playground in the middle composed by a football ground in the West side, two basketball grounds on the East side, and one last ground covered by a pergola. The vegetation in the area is sparse, only represented by six palm trees and various orange trees (Fig. 1).

Seville is characterized by a Mediterranean climate (Csa) as per Koppen-Geiger climate classification. It is one of the warmest cities in Europe [10], and it is impacted by the Urban Heat Island effect [11].

2.2 Field Study

2.2.1 Monitoring

In order to characterize the climatology of the study area and calculate the comfort indices, fixed monitoring, semi-mobile monitoring, and mobile monitoring were used. Based on ASHRAE 55 standards [1], four microclimate parameters were recorded: air temperature, relative humidity, wind speed, and radiation.

The fixed monitoring was carried out by a Watchdog 2700 Weather Station put on the roof of the school entrance building, and four fixed hygrothermal sensors OM-EL-USB-2-LCD Omega put in the open-air space at the school entrance, all recording data continuously since October 2021. The fixed monitoring allowed to measure the Urban Heat Island effect on the air temperature in the study area. Moreover, it recorded temperatures over 30°C in the

middle hours of half of the days, while October is a month qualified as intermediate weather in Seville. This highlights the serious climate problem faced by the school's pupils, and thus the need for a detailed study of human comfort in the school courtyard.

Semi-mobile and mobile monitoring were used to capture the spatial specificities of the site and obtain data with a higher temporal resolution during the survey sessions. The PCE-FWS20N station put on a tripod close to the interviews' space, and a temperature sensor carried out by the interviewer were used for this purpose.

2.2.2. Questionnaires

The survey methodology was established taking into account that most of the respondents were children. Both for keeping the survey time short and recording all the information needed for the subsequent comfort analysis, twelve questions were selected. They recorded personal details (age and gender), clothing (color and seasonality), activity, humor, food intake in the past hour, sensitivity to cold or heat, solar and time exposure, location of the children and their actual thermal sensation asked on a 5-point scale varying from "very cold" to "very hot", as defined by Nikolopoulou through the Actual Sensation Vote (ASV) [8].

2.3. Thermal comfort index

The thermal comfort model COMFA was used to predict the impact of the school outdoor conditions on the human body. The thermal load Q [$W/m2$] was calculated through (1). It is defined as the thermal load that needs to be brought (in winter) or dissipated (in summer) from the body to be in the comfort zone.
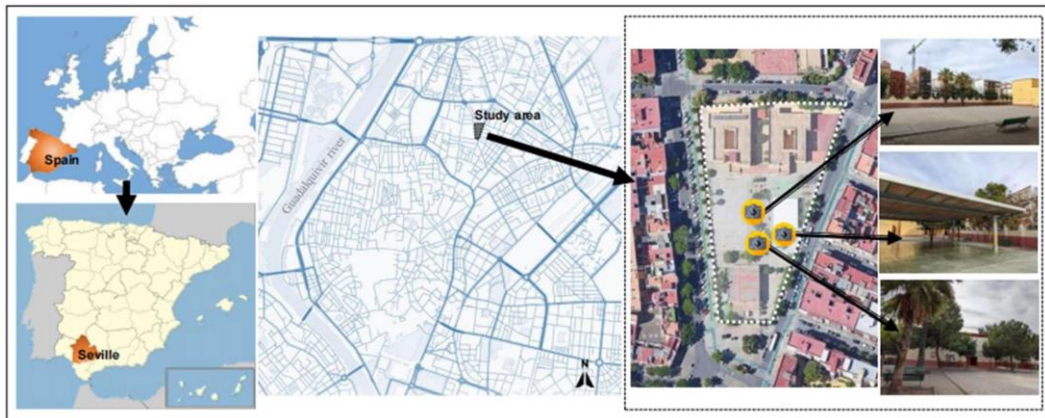
$$Q = (M - W) \pm (R + C) - Ereq \qquad (1)$$

Figure 1. Study area in Seville (Spain)

Where M [$W/m2$] is the heat generated by metabolism, W [$W/m2$] the mechanical work, $(R + C)req$ are the convective and radiant heat fluxes exchanged by the person but taking a required skin temperature $TSKreq$ to reach outdoor comfort conditions according to ISO 7933:2004 (Standard, 2004). Likewise, Ereq refers to the perspiration required by the body as defined by the same ISO 7933:2004 (Standard, 2004). Both terms are defined in (2) and (3).

$$TSKreq = 35.7 - 0.0274 - (M - W) \qquad (2)$$

$$Ereq = 0.42 - (M - W - 58.15) \qquad (3)$$

All of the above variables are defined in terms of a person's transfer area as defined by Du Bois D. and Du Bois E. F. [4], and to be adapted to a child. The definition and quantification of these variables has been defined in detail by ASHRAE [2]. For the present work, the acceptable thermal comfort conditions defined by the proposal of Pearlmutter et al. [9] for exteriors have been considered. The authors override the work value W and take a value of M of 2.5 met (116.3 W/m²), which is equivalent to an average activity between light (2 met) and moderate (3 met). Light activity refers to people at rest or walking slowly, and moderate activity to a walk at 1.3 m/s. According to the Q value a 5-point scale is defined for assessing people sensations as resumed in the Table 1.

Table 1. Sensation levels according to the thermal load of the COMFA model

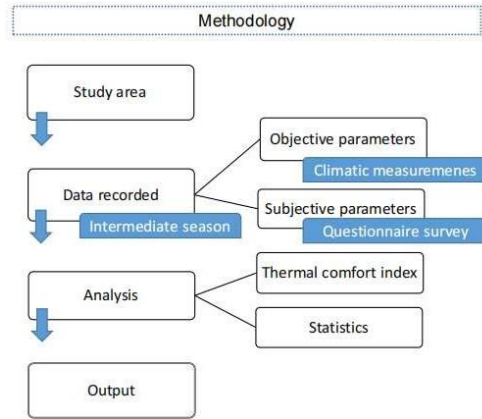| Sensation levels (COMFA)					
Level	1	2	3	4	5
Thermal load Q (W/m²)	>150	150 — 50	50 — -50	-50 — -150	< -150
Sensation	Very hot	Hot	Comfortable	Cold	Very cold

3. Methodology

Figure 2. Scheme of the methodology

The methodology carried out was divided into four steps (Fig. 2).

Previous to the survey and monitoring campaign, a mesh was defined over the study area aiming to distinguish between sunny and shaded areas (Fig. 3). It was sized so that a person in the center of each cell receives at least 70% of the incident radiation, which allows to conclude on its solar exposure as a function of time.

The field campaign was performed during October of the year 2021. This month was chosen for its intermediate weather. Moreover, summer months correspond to the summer holidays and so to a period where the school is not used. Surveys were carried out during twenty-two days, corresponding to the working days of the month of October, and each day from 12h30 to 13h30, corresponding to the hours where the sun is the hottest and the number of pupils in the study area is maximum.
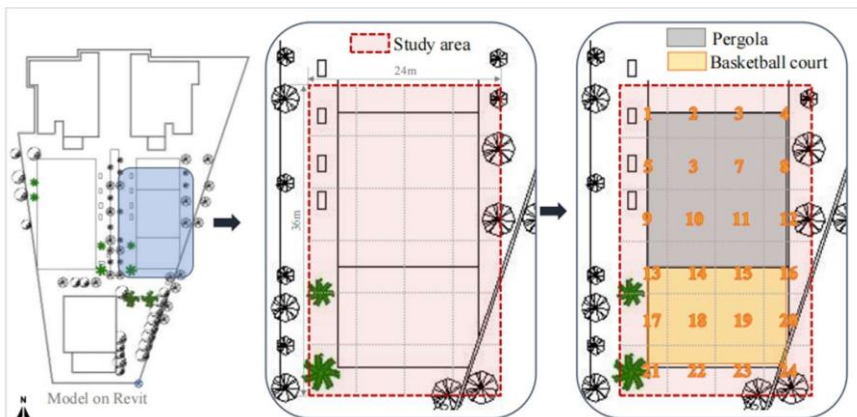

Figure 3. Study area and mesh (model on Revit)

Two types of data were recorded: climatic measurements providing by the monitoring (objective parameters), and responses to the questionnaire surveys (subjective parameters). A personalized comfort index for each respondent was generated using the climatic measurements, the respondent's location and personal characteristics - as defined in ASHRAE standards and according to the survey responses about clothing and level activity. Then, this index was compared to the real perception of the person.

4. Results

4.1. Survey results

A total of 537 questionnaires were conducted, with 48,38% of female respondents and 51,62% of male respondents. According to the results, the average age of the respondents (82,92%) is between 9 and 12 years old, most people have had a moderate food intake - which may influence later their thermal sensation response -, 47,28% defined themselves as heat-sensitive, preferring cold spaces, and the majority of people felt the space hot (39,3%) and 29,4% felt it very hot. Therefore, in total, more than two thirds of people would need an intervention on the space. However, 30,8% perceived the space as comfortable, highlighting the wide variation between people's perceptions.

4.2. Calculation of the comfort index

The thermal load (Q) was calculated by the COMFA model for all days studied in October and for each surface of the study area under the real climate conditions measured during the monitoring campaign. Four days in October were chosen for the representation of the results, corresponding to days with climatic characteristics that are representative of a typical October in Seville. The results were separated into three types of clusters. The first cluster includes all permanent shaded areas (Shadow Cluster). The second cluster corresponds to permanent sun areas (Sun Cluster). The last cluster includes surfaces which, depending on the time of day, can be shaded or sunny

(Intermediate Cluster). Fig. 4 shows the hourly results of the thermal load predicted by the COMFA comfort model.

On surfaces that are always in the shade, the thermal loads that the body needs to dissipate are one third of those needed on surfaces that are always in the sun. The majority of the time the COMFA model predicts thermal loads out of the comfort zone with values above 300W/m² in the middle of the day. More precisely, during the survey period, only the shadow cluster on the fourth day meets comfortable conditions. The air temperature at that time is 25.9ºC with zero incident radiation. On surfaces of the intermediate cluster the thermal load increases and lowers very quickly at the times of the day when it moves from shade to sun and back to shade. All of this shows the high influence of radiation on the human thermal comfort.

4.3. Comparison of the results given by the comfort model with the survey responses

The objective thermal loads, predicted by the COMFA comfort model, were compared to the subjective thermal sensations collected during the survey campaign, after they were translated into thermal loads. Fig. 5 shows the graph obtained for the four selected days on the three representative clusters. All the squares (whether green, yellow, or red) correspond to zones where the objective thermal sensations are identical to subjective thermal sensations.

Analysis of the results shows that 65% of the model's predictions match the actual feelings of the individuals. Furthermore, the model tends to overestimate people's feelings. When the results do not match, more than 45% of the model's predictions are associated with conditions worse than what people actually feel. Several explanations can be given, such as the acclimatization factor - Seville being a city where people are used to heat all year round - , the age of the individuals - who are children - and the usual practice of the space - as it is a courtyard, children are used to have a sustained physical activity.
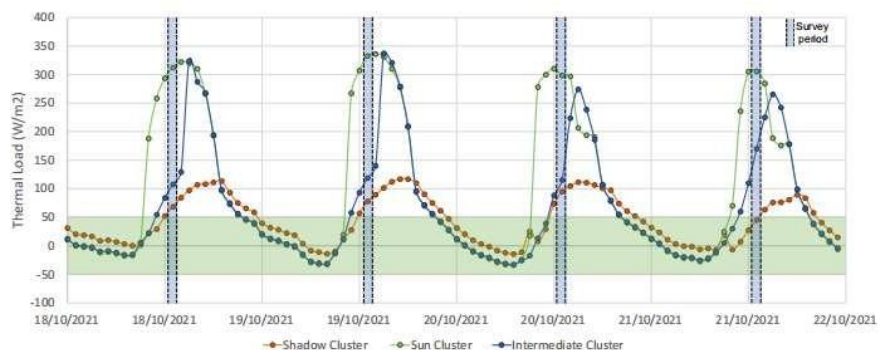

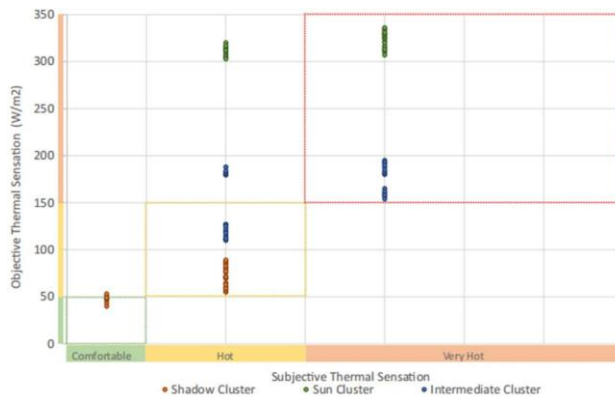Figure 4. Thermal load calculated by the COMFA model

Figure 5. Graph of comparison between the objective and subjective thermal sensations

5. Conclusion

The present investigation was conducted to determine the applicability of the thermal model COMFA for assessing the outdoor thermal comfort of a space in the Mediterranean climate. Microclimate parameters monitoring was carried out, in parallel of field surveys, both conducted in October 2021, in the courtyard of the Colegio de Educación Infantil y Primaria Arias Montano in Seville, Spain. COMFA model predictions were compared to subjective responses of the users of the space. The results highlight that the predictions of the COMFA model in spaces of Mediterranean climate like Seville are valid in the comfort zone but need to be corrected in the hot and very hot zones using field responses. More precisely, the comfort band should be considered higher, up to values of 70/80 W/m².

On the other hand, the study has highlighted the importance of field campaigns to properly assess the thermal comfort of a study area. First, they are necessary to use local climate variables as input data for the models, and thus obtain more realistic predictions. Secondly, field campaigns allow to study the applicability of these models on the concerned area. Finally, they can be used to calibrate the comfort scales in order to adapt them perfectly to the space and users.

Several ways to improve the methodology have been identified, such as increasing the accuracy of the location of the individual during the field campaigns, completing the calculation of surface temperatures with thermographic images, and measuring radiation more locally through the use of globes.

REFERENCES
1   ASHRAE, "ANSI/ASHRAE Standard 55: Thermal Environmental Conditions for Human Occupancy", 2017a

2   ASHRAE, "ASHRAE Handbook Fundamentals - Chapter 8 Thermal Comfort", In 2017 ASHRAE Handbook Fundamentals (2017th ed.). Atlanta., 2017b

3   Brown R. D., & Gillespie T. J., "Estimating outdoor thermal comfort using a cylindrical radiation thermometer and an energy budget model", *International Journal of Biometeorology*, 30(1), 43–52, 1986

4   Du Bois D., & Du Bois E. F., « A formula to estimate the approximate surface area if height and weight be known." 1916. *Nutrition (Burbank, Los Angeles County, Calif.), 5*(5), 303., 1989

5   Kántor, N.; Unger, J.; Gulyás, Á. Human bioclimatological evaluation with objective and subjective approaches on the thermal conditions of a square in the centre of Szeged. *Acta Climatol. Chorol.* 2007, *40*, 47–58.

6   Kenny, N.A.; Warland, J.S.; Brown, R.D.; Gillespie, T.G. Part A: Assessing the performance of the comfa outdoor thermal comfort model on subjects performing physical activity. *Int. J. Biometeorol.* 2009a, *53*, 415–428.

7   Kenny, N.A.; Warland, J.S.; Brown, R.D.; Gillespie, T.G. Part B: Revisions to the COMFA outdoor thermal comfort model for application to subjects performing physical activity. *Int. J. Biometeorol.* 2009b, *53*, 429–441

8   Nikolopoulou, M.; Steemers, K. Thermal comfort and psychological adaptation as a guide for designing urban spaces. *Energy Build.* 2003, *35*, 95–101.

9   Pearlmutter D., Jiao D., & Garb Y., "The relationship between bioclimatic thermal stress and subjective thermal sensation in pedestrian spaces", *International Journal of Biometeorology*, 58(10), 2111–2127, 2014

[10] Thomas A. H., Marcel S., Ewan D. D., & Fabio M., "Estimating average daytime and daily temperature profiles within Europe", *Environmental Modelling & Software,* vol. 21, 2006

11   Romero Rodríguez L., Sánchez Ramos J., Sánchez de la Flor F. J., & Álvarez Domínguez S., "Analyzing the urban heat Island: Comprehensive methodology for data gathering and optimal design of mobile transects," *Sustainable Cities and Society*, vol. 55, Apr. 2020, doi: 10.1016/j.scs.2020.102027

12   Ruiz, M.A.; Correa, E.N. Developing a Thermal Comfort Index for Vegetated Open Spaces in Cities of Arid Zones. *Energy Procedia* 2014, *57*, 3130–3139.

13   Xie, Y.; Huang, T.; Li, J.; Liu, J.; Niu, J.; Mak, C.M.; Lin, Z. Evaluation of a multi-nodal thermal regulation model for assessment of outdoor thermal comfort: Sensitivity to wind speed and solar radiation. *Build. Environ.* 2018, *132*, 45–56.

Clean and sustainable energy potential in Timisoara using piezoelectric power generators - GEMPT

Andrei Dună[1], Diana Țucu[1]

[1] Second year students, Bachelor's degree program in Construction Installations, Faculty of Constructions, Polytechnic University of Timisoara, Piața Victoriei Nr. 2, 300006 Timișoara, jud. Timiș, Romania
www.upt.ro, andrei.duna@student.upt.ro, diana.tucu@student.upt.ro, 2022
Coordinator: As. univ. dr. eng. Dănuț Tokar, *danut.tokar@upt.ro*

*Abstract-***The paper analyze and presents a solution for the realization of renewable, non-combustible energy sources by involving the citizens of Timisoara, from children to the elderly, and using this energy for urban purposes such as: public illumination, illumination of passenger stations, access to charging various devices. This clean energy is obtained by transforming the kinetic energy of pedestrians into electricity based on the piezoelectric effect.**

*Index Terms***- GEMPT generator, harvesting energy, piezoelectricity,**

1.Introduction

The Renewable Energy Directive (D 28/2009/EU) together with the Energy Efficiency Directive (D 27/2012/EU) and the Energy Performance of Buildings Directive (D 31/2010/EU) have activated a set of measures to enable propitious conditions for a significant and long-term improvement in the use of renewable energy sources and energy performance in Europe's built environment.

Today, EU legislation is increasingly promoting renewable resource projects and encouraging local settlement policies to find locally specific solutions.

Renewable energy sources are energy sources that are naturally replenished (or renewed). Typical examples are solar, wind energy and biomass.

1.1. Renewable energy sources, inventoried in this paper as feasible, are divided into:

a. Non-combustible renewable energy (or energy harvesting):

-*Hydroelectric energy*: electricity generated from the potential and kinetic energy of water through hydropower plants;
-*Energy produced by the motions of the seas and oceans:* the mechanical energy derived from tidal movements, wave movements or ocean currents and harnessed to generate electricity;
-*Geothermal energy*: energy available from the heat in the earth's crust, usually in the form of hot water or steam;
-*Wind energy*: the kinetic energy of the wind converted into electricity in wind turbines;

-*Solar energy*: solar thermal energy (radiation harnessed from solar heat by thermo-conversion effect) and solar energy for electricity generation by photovoltaic conversion.
-*Heat stored in air, water, ground:* heat pumps are used which are powered by electricity or other additional energy (mechanical work) to extract stored energy (heat) from air, ground or water and convert/transfer it into heat energy adapted as parameters for use elsewhere (e.g. to heat space through underfloor heating systems and/or water in domestic buildings). Heat pumps can be used by individual households as well as, on a larger scale, in industry and in commercial and public services. Energy flows related to heat pumps used for cooling are excluded, only heat pumps used for heating (hot water) are included.

b. Combustible renewable energies

-*Biofuels*: biomass fuels (including solid biofuels, biogas and liquid biofuels);
- Renewable urban waste.

1.2. Situation of energy sources in the city of Timișoara

The city of Timișoara is located at the intersection of the 45°47' north latitude parallel and the 21°17' east longitude meridian. It has a total area of 12,926.83 ha.

1.2.1 The potential of energy sources

Currently the energy sources and fuels secured for the city's consumption are:
Electricity: Timisoara is supplied with electricity from the national energy system, the basic sources being the Iron Gates hydroelectric power stations and the Mintia thermoelectric power station (fluctuating). Power is supplied by the 220/110 kV Timișoara and Săcălaz system stations. Annual electricity consumption averaged 736,000 MWh, of which domestic consumption 258,000 MWh, industrial consumption 291,000 MWh and building consumption 187,000 MWh.

Thermal energy: The thermal energy supply of the city of Timisoara is mostly centralized, through the urban heating system, supplied with primary thermal agent (hot water) produced in two thermal power stations (central-CET and southern-CET), managed by S.C. COLTERM S.A. The fuel used is coal, fuel oil and combustible natural gas, with a small proportion of biomass.

Combustible gases: The gases used as fuel come from either the Transylvanian Basin or the Banat Plain. The supply of natural gas to Timisoara from the national transport system is made from the main transport pipelines, through regulation stations - measurement - delivery, the most important of which are: SRM 1 Plopi, SRM 3 Sugar Factory, SRM 6 Calea Lipovei. These gases are delivered to the population and industries for food preparation, individual heating, and technological processes.

Solid fuels. The number of consumers of heat produced by burning solid fuels is currently unknown.

Solar energy. There are some residential buildings using solar energy. Some use it, by installing solar panels, for the preparation of domestic hot water, swimming pool water, others as an input to the heating agent, and others by installing photovoltaic panels which convert solar energy into electricity. The number of consumers using solar energy is still not identified. It should be noted that between 1979 and 1982, Timisoara benefited from the first large-scale project for the preparation of domestic hot water for an entire neighborhood. All that is left of that installation is the name of the neighborhood - Cartierul Soarelui. (the Sun's Neighborhood)

Geothermal energy. Timisoara is located on very rich deposits of thermo-mineral water, with excellent therapeutic properties, but also with high temperatures of 50 to 80^0 C, which would make it suitable for use in heating installations using heat pumps. In the 1980s, several boreholes were drilled to collect thermal water, and there were about 40 in Timis County. In Timisoara, for example, such old but unused wells exist in Alpinet Park, on Pârvan Boulevard (opposite the Thermal Spa), in Children's Park, in Bihor Square and in Ronaț, near Danube Street. Some of these were once used, but in recent decades their operation has been stopped, for various reasons, many unknown.

1.2.2. Timisoara's energy source policies

At present the city does not have an energy strategy that has been analyzed and outlined and publicly exposed.
 Some materials of the local administration highlight some general ideas and desires as strategic objectives, such as:
- energy security and independence;
- attracting the necessary capital for the development and modernization of Timisoara in the field of energy efficiency and "clean" energy production;

- to ensure the present and future energy needs, mainly from renewable sources, at the lowest possible prices, to reduce greenhouse gas emissions, provide energy sources for sustainable economic development and to ensure a high standard of living for all the inhabitants of Timisoara.

1.2.3 Research potential for renewable energies

In Timisoara there is the Research Institute for Renewable Energies (ICER), a project of the Polytechnic University of Timisoara, whose main objective is to develop new areas of research in the use and optimization of the use of renewable energies in line with international research trends and the requirements of the Romanian and European economy.
 ICER Research is carried out for:
- harnessing solar energy;
- production and use of biogas;
- development of micro-hydropower plants;
- harnessing wind energy;
- the use of geothermal energy;
- intelligent control of energy conversion and storage;
-development of advanced materials and their efficient energetic processing;
-analysis of the impact of climate change on the natural and built environment;
- the design of intelligent and energy-efficient buildings.
 However, so far none of the solutions developed at the institute have been applied locally.

2. Methods

We propose to carry out a project that we called *"Walk & Smile - generate and consume clean energy in your city"*.

The determination to carry out such a project aims:
-to narrow the gap between EU regulations and the situation in the city;
- to appearance of international inventions to be exploited;
-to identify the possibility of free involvement of the city's inhabitants without considerable effort;
- to involve young people and children in the production of clean energy through recreational and fun activities;
- to obtain clean energy with minimum investment.

What involves this project:

Mounting in the pedestrian structure a piezoelectric power generator activated by the pedestrians walking on it which we called GEMPT. Basically, the system converts the kinetic energy of pedestrians into piezoelectric energy. Optional optical batteries - BTOPT - can also be added.

2.1 Description of GEMPT

The proposed **GEMPT** system is based on several examples of technologies such as:

- technology that Kouhei Hayamizu developed at Keio University's Graduate School of Media and Governance. This technology uses "piezoelectricity", a property that certain materials must generate an electric current when pressed by an external force. Kouhei Hayamizu installed his system in a railway station. After 20 days, by passing 900,000 people a day through the area, he was able to generate enough energy to power 1,422 TVs for an hour. Another system was installed on the Goshiki Zakura Ohashi bridge in Tokyo. This system of piezoelectric generators uses the traffic on the bridge to power 108 of the bridge's LED light fittings.

-in a study Xiaofeng Li and Vladimir Strezov, obtained piezoelectric power in a central building of Macquarie University in Sydney, Australia by installing a pedestrian pavement on 3.1% of the total floor area, achieving 1.1 MW h/year, or 0.5% of the building's annual energy needs.

-in Israel, a company Innowattech has installed piezoelectric IPEGs under a congested highway. The energy generated powers street lighting, billboards, and traffic signs. When vehicle traffic is more than 600 per lane per hour, up to 400 kWh of electricity can be generated per lane kilometer, enough energy to power 600 to 800 homes. IPEGs are piezoelectric crystals that can take the mechanical energy created by changes in weight, motion, vibration, and temperature and convert it into electricity. This energy is stored in the electronic capacitors of the storage system.

- the State of California has passed a bill for a pilot roadway program. They estimate that 0.6 miles of a single-lane highway can create enough energy to power 30,800 homes a year.

GEMPT is based on piezoelectricity.

Piezoelectricity is the electrical charge that builds up in certain solid materials (such as crystals, certain ceramics and biological materials such as bone, DNA and various proteins) in response to the application of mechanical stress. For example, lead zirconate titanate crystals can generate measurable piezoelectricity when their static structure is deformed by about 0.1% of its original size. When mechanical pressure is applied to the piezoelectric element by means of electrodes, electrical charges will be created within the crystals. These positive and negative charges are also distributed on the faces of the crystals. A metal plate is placed on these ceramic elements which collects these positive and negative charges and is then used to generate voltage and supply electric current through the circuit. A piezoelectric generator is composed of one or more piezoelectric elements (Fig. 1).

The GEMPT system (Fig.2., Fig. 3., Fig. 4), **is suitable for installation in the following locations in Timisoara:**
- tram, trolleybus and bus stations;
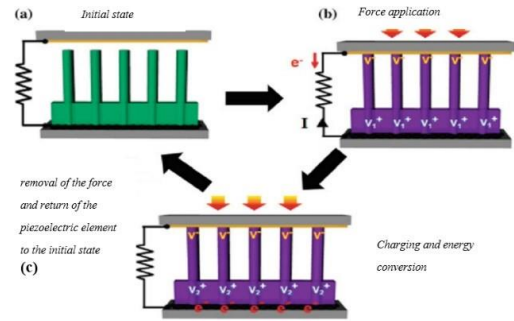- pedestrian crossings with high traffic at the targets;

Figure 1. Scheme of a piezoelectric generator in different states: a) initial state; b) under an externally applied force; c) charging with positive charge potential generated by the presence of electrons near the lower electrode. (*Source: https://www.researchgate.net/figure/ Schematic -of-a-piezoelectric-generator-in-different-states-a-initial-state-b-under_fig4_328700076*)

- playgrounds in parks and squares, sports grounds;
- access routes to railway stations;
- pedestrian bridges;
- cycle paths and the Bega canal promenade.

2.2 Biomechanics of the human body

To be able to calculate how much energy could be produced by a piezoelectric generator through the mechanical pressure exerted by the movement of the human body, we need to understand a few things about the biomechanics of the human body.

Bipedal locomotion (walking) is, from a biomechanical point of view, a process of displacement in which the human body, in motion, is supported cyclically and alternately by each lower limb (except for a transition period when both legs are on the ground) (Fig. 5).
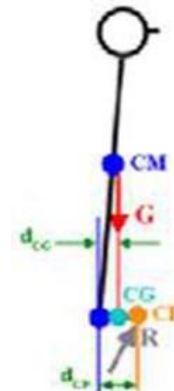

Figure 5. Positions in the human body of the Centre of Mass (CM), Centre of Weight (CG) and Centre of Pressure (CP) (Source: http://www.pt.ntu.edu.tw/hmchai/biomechanics/)

Walking, defined as 'alternating bipedalism', has as its unit of measurement the walking cycle (double step) represented by the distance between the point of contact with the ground (heel) of one foot and the next point of contact of the same foot.
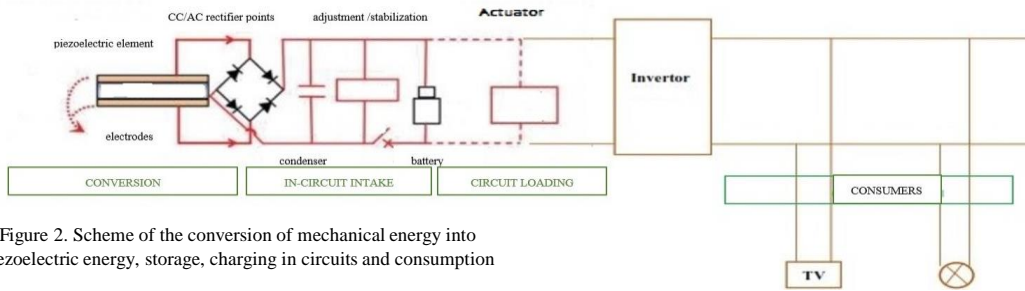
Figure 2. Scheme of the conversion of mechanical energy into piezoelectric energy, storage, charging in circuits and consumption
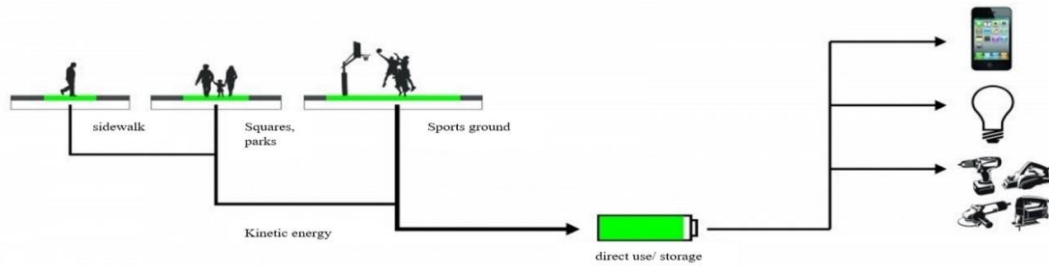

Figure 3. GEMPT layout scheme and interconnection to possible consumers
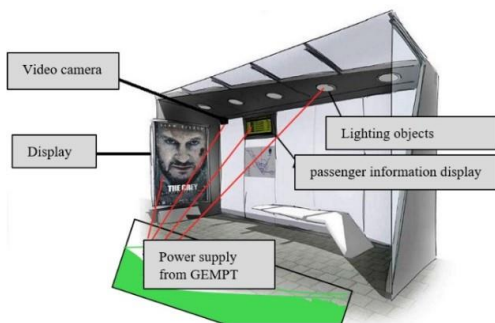

Figure 4. Schema of the proposed placement of GEMPT generators and possible consumers in Timisoara transport stations
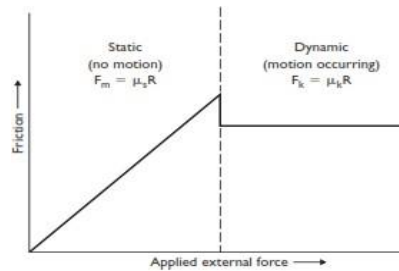

Figure 6. Diagram of static and dynamic frictional forces

(Source: https://ftramonmartins.files.wordpress.com/2016/09/basic-biomechanics-susan-hall-6th-edition1.pdf)

Stability and posture of the human body need to be described/modelled mathematically and mechanically by means of specific parameters and mathematical objects. Among these the most important are: Centre of Mass (CM), Centre of Weight (CG) and Centre of Pressure (CP). The center of pressure (CP) is the point at which the resultant of all reaction forces with the ground acts. From a biomechanical point of view the CG, due to inertia, cannot accurately follow the same trajectory as the CP. There is thus a gap between the two centers.

If a body is static (stationary position), the size of the frictional force developed is equal to that applied by the external force. Once a movement is initiated, the magnitude of the frictional force remains at a constant level below that of the maximum static frictional force (Fig. 6).

The coefficient of friction between two surfaces has different values depending on whether the bodies in contact are stationary (static) or moving (kinetic). The two coefficients are known as the coefficient of static friction (μ_s) and the coefficient of kinetic friction (μ_k).

The magnitude of the maximum static friction is based on the coefficient of static friction:

$$F_m = \mu_s R \qquad (1)$$

The diagram in Fig. 7 gives an average value of the static friction coefficient $\mu s = 0.5$.

The size of the kinetic friction force is based on the kinetic friction coefficient:

$$F_k = \mu_k R , \qquad (2)$$

from the diagram results an average value of the static friction coefficient $\mu s = 0.5$, $\mu k = 0.4$
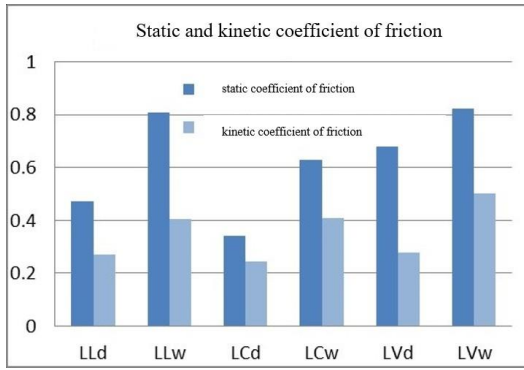
Figure 7. Diagram of friction coefficients for the materials from which the soles of travellers' shoes are made (leather, rubber) and the materials covering the GEMPT generator (copolymers, linoleum) (LLd - friction between leather - dry laminate; LLw - friction between leather - wet laminate; LCd - friction between leather - dry ceramic; LCw - friction between leather - wet ceramic; LVd - friction between leather - dry vinyl; LVw - friction between leather - wet vinyl).

(Source: https://www.researchgate.net/figure/Static-and-kinetic-friction-coefficient-values-LL-leather-laminate-LC-leather-ceramic_fig3_320069824)

The coefficient of friction describes the interaction between two surfaces in contact.

3. Data presentation and Discussions

3.1. Calculation of the energy that can be produced by GEMPT in public transport stations for trams, trolleybuses and buses in Timisoara

In 2020 Timisoara had 179281000 registered passengers (107417000 by tram, 36901000 by trolleybus, 34963000 by bus). This results in 498003 passengers per day.

Assuming an average mass of each passenger as $m = 75$ kg, moving at a speed $v = 1.2$ m/s, this gives a force :

$$F = 75 \text{ kg} \times 9.8 \text{ m/s}^2 \times 0.5 = 367.5 \text{ N} \qquad (3)$$

The power that compensates the resistance to kinetic friction is:

$$P = F \text{ x } v = 367.5 \text{ N x } 1.2 \text{ m/s} = 441 \text{ W} \qquad (4)$$

t is the charging time and is measured based on the length of the piezoelectric generator lp (assumed to be 0.50 m × 0.50 m) and the pedestrian speed $v = 1.2$ m/s :

$$t = lp/v = 0.5/1.2 = 0.4166 \text{ s} \qquad (5)$$

The mechanical energy is measured by considering power as an integral of time:

$$U_{in} = \int_0^t P \text{ dt} = \int_0^{0,4166} 441 \text{ dt} = 183.72 \text{ J} \qquad (6)$$

The energy generated by the piezoelectric generator is :

$$UE = 0.078 \times 183.72 = 14.33 \text{ J} \qquad (7)$$

If an area of 10 m² is allocated to each public transport station, 20 piezoelectric generators can be installed. Assuming that there are on average 20 passengers and that each passenger steps on a generator when getting on or off the vehicle, the energy generated by the generators will be:

$UE_{tot} = 14.33$ J x 20 generators = 286.6 J = 286.6 J x $2.77777778 \times 10^{-7} = 796.11111748$ x 10^{-7} kWh   (8)

A calculation for year 2020

179281000 registered passengers /146 stations x 365 days = 3364 passengers / station in one day

3364 passengers / station day / 20 passengers results = 168 boarding/ disembarking series / day

UE $_{station/day}$ = 168 x 796.11111748 x 10^{-7} kWh = 133746.667737 x 10^{-7} kWh

UE $_{day TM}$ = 146 station x 133746.667737 x 10^{-7} kWh = 19527013.49 x 10^{-7} kWh

UE $_{year TM}$ = 365 days x UE $_{day TM}$ = 7127359923.69 x10^{-7} kwh = 712.74 kWh

Based on previous assessment, we have shown, through mathematical determination, the opportunity to develop such a project on a city scale. Also, for the second stage, the team has already started the development of our own piezoelectric harvester element. The image below captures one of the various experiments conducted using three piezoelectric elements. (Fig.8), integrated in an harvesting element (Fig.9)
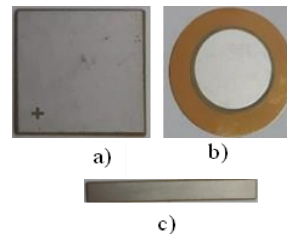

Figure 8. Types of piezoelements (a) Ceramic plate-2,85 MHz, PZT5 21x21x0,7 mm; b) Ceramic plate-21 KHz, PZT Φ30x0,27 mm; c) Ceramic plate-41,5 KHz, PZT5X 70x10x0,48 mm)
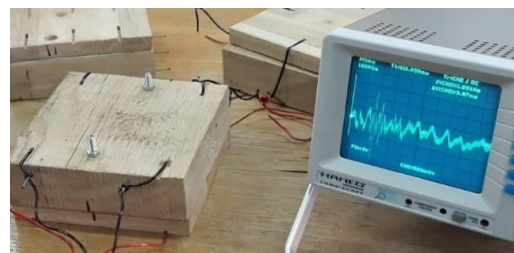

Figure 9 Harvesting element (left), and oscilogramma (right) for PZT5X in experimental tests, corresponding to charging at 30 N (maximum voltage 5,05V)

3.2. Calculation of the investment

In table 1 there are presented the results of investment calculation.

TABLE 1 CALCULATION OF INVESTMENT

System component, type, code	Price without taxes, EURO	Quantity	Total cost without taxes, EURO	Manufacturer
Bridge rectifier: braking rectifier assemblies; Urmax: 1,4kV | INFO | PDF Manufacturer: **IXYS** Manufacturer name: **VGB0124AY7A**	100	146 pieces	14600	https://www.tme.eu/ro/katalog/punti-redresoare
Capacitor or capacitor bank	110,00	146	16060	https://www.tme.eu/ro/katalog/punti-condensatoare
Piezoelectric generator: **1PC 50*50 power generation sheet PZT piezoelectric ceramic bending element** Product name: Piezoelectric ceramic bending element, 50*50 new energy power generation sheet, PZT piezoelectric ceramic power generation sheet, high-efficiency energy-saving power generation sheet Output voltage: 0-33v Output current: 0-26mA Resonance impedance: <66 oHm Static capacitance: 351-431 nF Substrate material: high beryllium copper #CW615N Piezoelectric ceramic material: PZT-5X $Kt = 0.51$ $eT33 = 1800$ $Qm = 800$ $Kp>$ 0.83% $D33> 880x10-12C/N$ $Kt33 = 4900$ $T=0.15mm$ $t1 = 0.20mm$, $t_2 = 0.20mm$	53 Euro x 20 piece/station	146	154760	Piezoelectric ceramics - Factory Direct PIEZO HANNAS is a global manufacturer of high quality piezoelectric ceramics
HDPE membrane for generator placement	100Euro/40 mp	146	14600	
Battery	150	146	21900	
Invertor	300	146	43800	
Electrical installation and switchgear for each passenger station	300	146	43800	
Workmanship			150000	

4. Conclusions

The paper presents a solution for the realization of renewable, non-combustible energy sources by involving the citizens of Timisoara, from children to the elderly, and using this energy for urban purposes such as: public illumination, illumination of passenger stations, access to charging various devices. This clean energy is obtained by transforming the kinetic energy of pedestrians into electricity based on the piezoelectric effect**.**

The advantage of the presented solution for this investment project, compared to the current existing solutions, as well as to other alternative systems, is that it produces cost free energy, making the modern concept of *"Walk & smile - generate and consume clean energy in your city"* a concrete reality and a real option for every city.

5. References

1https://www.sciencedirect.com/science/article/abs/pii/S0196890414005159?via%3Dihub
2 https://ourworld.unu.edu/en/lets_generate_electricity_by_walking
3https://www.offgridenergyindependence.com/articles/1589/energy-harvesting-roads-in-israel
[4] https://www.21stcentech.com/energy-update-heard-piezoelectricity-electricity-feet/
[5] https://link.springer.com/article/10.1007/s11595-014-1023-3
6https://www.steminc.com/PZT/en/piezo-ceramic-generator-40x11x17mm
7 https://en.wikipedia.org/wiki/Piezoelectricity
8https://greenbuildingelements.com/2011/06/24/piezoelectricity-elements/
9 https://www.steminc.com/PZT/en/piezo-plate?gclid=Cj0KCQiAyoeCBhCTARIsAOfpKxiYcU7a4t1Y_4Fy09O5a48P4bMn9D2ovyrDmRMrUmlWyq3IoV5uey0aAm3ZEALw_wcB
10 https://www.watelectrical.com/mcq/piezoelectric-transducer/
11http://www.pt.ntu.edu.tw/hmchai/biomechanics/
[12]https://ftramonmartins.files.wordpress.com/2016/09/basic-biomechanics-susan-hall-6th-edition1.pdf
13https://www.researchgate.net/figure/Static-and-kinetic-friction-coefficient-values-LL-leather-laminate-LC-leather-ceramic_fig3_320069824
14https://www.researchgate.net/figure/Schematic-of-a-piezoelectric-generator-in-different-states-a-initial-state-b-under_fig4_328700076
15 https://www.watelectrical.com/piezoelectric-generator-circuit-explanation-working-types-and-applications/
16https://www.electroniclinic.com/how-to-make-piezoelectric-generator/
17https://blog.piezo.com/four-steps-to-selecting-a-piezoelectric-energy-harvesting-device
18https://tomorrow.city/a/piezoelectricity-movements-generate-electricity

The Effects of Energy Renovations in Southern European Residential Buildings with Intermittent or Continuous Heating

Yangmin Wang [a], Risto Kosonen [a,b,c], Juha Jokisalo [a,c]

[a] Department of Mechanical Engineering, Aalto University, Espoo, Finland, Student: yangmin.wang@aalto.fi,
Supervisors: risto.kosonen@aalto.fi, juha.jokisalo@aalto.fi, Year when the work on which the submission is based has been approved: 2022.
[b] College of Urban Construction, Nanjing Tech University, Nanjing, China.
[c] FinEst Centre for Smart Cities, TalTech, Tallinn, Estonia.

Abstract—**Improving energy efficiency of residential stock by renovation is important for achieving carbon neutrality in the EU. This study aims at verifying several novel renovation technologies and their combinations' impact in southern European climate conditions through building level simulations. The technologies comprise bio-aerogel thermal insulation, photovoltaic vacuum window, phase change material, insulating breath membrane, room specific air handling unit with heat recovery, photovoltaic/thermal system and solar assisted heat pump. A Greek apartment building and a Spanish terraced house were chosen as the demo buildings and simulated with an intermittent or continuous heating schedule in IDA ICE, acting as the reference cases for renovation technologies simulations. The novel renovation technologies were classified into the passive, ventilation and generation packages, and then integrated into the building models to evaluate their impact on building energy consumption and indoor climate.**

The impact of renovation technologies on building energy consumption and indoor climate is significantly affected by heating schedules. The energy consumption reduction acquired by thermal insulation improvement under intermittent heating schedules is much lower than that under continuous heating schedules in both demo buildings since thermal insulation improvement led to an indoor air temperature increase when intermittently heated. Besides, when the intermittent heating schedule was switched to the continuous heating schedule, although the absolute energy consumption reduction brought by generation technologies increased, the relative reduction in percentage was diminished due to the increased backup energy demand for space heating.

Index Terms—**Energy conservation, Energy renovations, Indoor climate, Intermittent heating**

Introduction

The building sector is the largest single contributor to energy consumption and carbon emissions in the EU, which accounts for 40% of total energy consumption and 36% of greenhouse gas (GHG) emissions. Thus, buildings conserve a great potential for energy conservation and emission reduction. As the new buildings are commonly constructed based on the energy efficiency regulations and only account for around 1% of the EU building stock, it is more important to renovate the existing building stock, especially those built up without taking the energy efficiency as a priority [1]. Correspondingly, the EU commission published its Renovation Wave Strategy to accelerate building sectors towards climate-neutral levels by 2050 [2].

Following the renovation wave, SUREFIT project aims at finding sustainable solutions for affordable renovation of the EU residential buildings. A target of this project is to reduce heat loss of the building envelope and energy consumption of heating, cooling, ventilation and lighting, while increasing share of renewable energy in the building to achieve near zero energy consumption. To explain the sustainable renovation solutions intuitively, a Greek apartment building and a Spanish terraced house were chosen as the demo buildings to implement different energy-saving measures, including bio-aerogel thermal insulation, photovoltaic vacuum window, phase change material, insulating breath membrane, room specific air handling unit with heat recovery, photovoltaic/thermal system and solar assisted heat pump.

Although the performance of these renovation technologies has been proved in several studies [3,4], according to the authors' best knowledge, scientific research which combines them in different packages to assess their building level performance is still unavailable. The study focuses on comparing the impact of renovation technologies and their combinations on building energy consumption and indoor climate in southern European countries (Greece and Spain). Besides, based on the simulations with different heating schedules, this study can also present the impact of intermittent or continuous heating schedules on the energy conservation potential of renovation technologies.

Methods

Simulation setup

The demo buildings were modelled and simulated in a dynamic simulation tool IDA ICE, which is commonly used in Nordic countries. The building models were built up according to input data from building owners and online database TABULA WebTool [5]. They were simulated on an hourly timescale to obtain hourly energy demand and indoor climate profiles. These demo building models were

used as the reference cases for renovation technology simulation.

The SUREFIT renovation technologies were classified into different renovation packages including the passive package, consisting of bio-aerogel thermal insulation, PV vacuum window, and phase change material; the ventilation package, including insulating breath membrane and room specific air handling unit with heat recovery (RAHU); the generation package, comprising photovoltaic/thermal (PV/T) system and solar assisted heat pump (SAHP). As shown in Figure 1, they were integrated into the reference case models with intermittent or continuous heating and simulated separately by following the rule of starting from a single technology to all technologies in each package. Finally, the simulated final combinations contain all the technologies in the passive and ventilation package and either of the technologies included in the generation package.
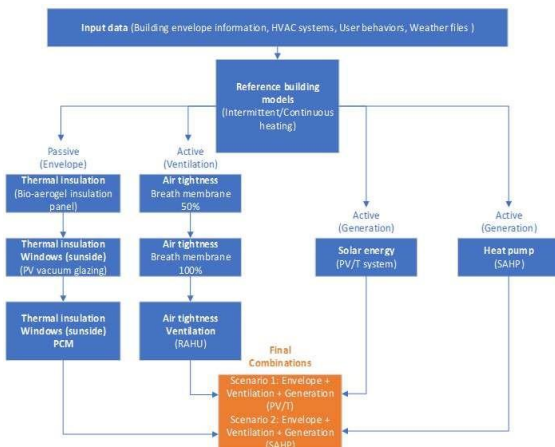

Figure 1. Simulation of renovation packages in IDA ICE.

Demo building descriptions

The Greek demo building located in Peristeri, Athens is a small apartment building constructed in 1980s. This apartment building consists of two apartments floors and a workshop. It is attached with two other buildings on the east and west sides. The apartment floors are heated with an oil boiler and water radiator system, and bedrooms and living rooms are equipped with electric air conditioners for cooling. Domestic hot water (DHW) is supplied by a solar thermal system.

The Spanish demo building is a terraced house in Valladolid. It consists of four apartments, and each apartment contains two residential floors and unheated basement floor. Each apartment is heated by an independent heating system, which are a mix of gas boilers and electric heaters.

Table 1 and Table 2 show the properties of the building envelope and properties of HVAC systems in each demo building before renovation. Most of the input data were provided by building owners, while the left unknown data were defined based on literature or TABULA WebTool. As field tests of airtightness were not implemented in the demo buildings, the air leakage rate at 50 Pa pressure difference used for simulation is an assumed value based on typical airtightness of residential buildings in southern European countries (e.g., Spain) [6].

Table 1. Properties of building envelopes in the demo buildings before renovation.

Demo building	Greek apartment building	Spanish terraced house
U-values of envelope [W/m²K]		
External wall	0.7	1.7
Roof	3.9	1.6
External floor	3.6	2.9
External door	1.1	2.2
Windows	5.9/3.0	5.8/2.8
Infiltration		
Air leakage rate, n_{50} [ACH]	6.7	6.7

Table 2. Properties of HVAC systems in the demo buildings before renovation.

Demo building	Greek apartment building	Spanish terraced house
Ventilation system	Natural ventilation	Natural ventilation
Space heating system	Oil boiler and water radiators	Gas boiler and water radiators/Electric heaters
Maximum heating capacity of boiler [kW]	65	65
Efficiency of boiler [%]	81	81
Power of electric heater [kW]	-	
Setpoint, living spaces [°C]	20	18-20
Setpoint, other rooms[°C]	20	18-20
Design temperature of water radiators [°C/°C]	90/60	70/40
Heating design outdoor temperature [°C]	1.8	-4.1
Cooling system	Split cooling units	No
Cooling capacity [kW]	2.6/7.0	-
Coefficient of performance	3.1/5.6/6.1	-
Setpoint [°C]	25	-
DHW	Solar collector and boiler	Gas boiler
Heating capacity [kW]	65.0	65.0
Efficiency [%]	81	81
Cold city water temperature [°C]	15	12
DHW outlet temperature [°C]	55	55
DHW use [L/day/person]	50	26
DHW recirculation loss [W/m²]	0.5	-

Heating schedules

In this study, the building level simulations were implemented with both intermittent and continuous heating schedules. The intermittent heating schedules used for simulation were defined based on the occupant's feedback to reflect energy consumption level in the existing demo buildings (see Table 3).

Table 3. Intermittent heating schedules for different demo buildings.

Demo building	Heated space	Intermittent heating schedule
Greek apartment building	The whole apartment area	From 1 Nov to 31 Mar, 20 °C [7:00-9:00, 19:00-22:00]
Spanish terraced house	Ground floor	All year round, 20 °C [14:00-23:00], 17 °C otherwise
	Top floor	All year round, 18 °C [14:00-23:00], 17 °C otherwise
	Attic	From 1 Oct to 30 Apr, 20 °C [14:00-23:00]

The same continuous heating schedule was applicable for both demo buildings. The continuous heating schedule

refers to that the living spaces are continuously heated to 20 °C from 1st September to 31st May.

Renovation technologies

Passive package

The passive package includes three technologies: bio-aerogel thermal insulation, PV vacuum window and phase change material (PCM). Bio-aerogel thermal insulation is an environmentally friendly insulating material that is made of starch-based aerogel. It was made into a prefabricated panel installed on the outside or inside of the external walls and roofs in the demo buildings. PV vacuum window is a daylight-management apparatus with photovoltaic solar cells embedded in a window [3]. It can not only generate electricity during the daytime but also decrease heat transfer through windows due to its low U-value. To maximize the electricity generation of PV vacuum windows, they were installed on the south façade of the demo buildings. PCM is a substance that releases/absorbs sufficient energy at the phase transition between solid and liquid to provide useful heat/cooling. PCM product S21, a salt hydrate, was chosen and treated as an independent PCM layer installed under the ceiling of the demo buildings. The melting process starts at 18 °C, reaches its peak at 27 °C, and ends at 36 °C [7]. Table 4 shows more detailed properties of these renovation technologies.

Table 4. Properties of the renovation technologies in the passive package.

Renovation technology	Properties
Bio-aerogel thermal insulation	Thermal conductivity [W/mK]: 0.037, Density [kg/m^3]: 43, Specific heat [J/kgK]: 2260, Thickness of insulation panel [m]: 0.05
PV vacuum window	Solar heat gain coefficient (SHGC): 0.42, Solar transmittance: 0.3, Visible transmittance: 0.65, U-value of glazing [W/m^{2}K]: 0.6, Efficiency of electricity generation [%]: 3.5, Area of PV vacuum windows [m^2]: 11.2 (Greece), 1.1 (Portugal), 19.6 (Spain)
PCM Product S21	Layer density (solid) [kg/m^3]: 1100, Layer specific heat (solid) [J/kgK]: 2300, Layer heat conductivity (solid) [W/mK]: 0.22, layer specific heat (liquid) [J/kgK]: 2300, Layer heat conductivity (liquid) [W/mK]: 0.22, Specific heat during reversing [J/kgK]: 300

Ventilation package

The ventilation package consists of insulating breath membrane and room specific air handling unit with heat recovery (RAHU). Insulating breath membrane could be seen as a thermal insulating measure which can also improve the airtightness of a building after renovation [8]. The breath membrane layer was installed over the external walls and roofs of the demo buildings. Since the air leakage rate of demo houses after installing insulating breath membrane was unknown, two cases with different assumed air leakage rates were simulated in this study: 50% airtightness improvement (the average value of the infiltration rate of the existing building and the tested air leakage rate of insulating breath membrane) and 100% airtightness improvement (the tested air leakage rate of insulating breath membrane). RAHU is an independent mechanical ventilation device installed above the windows, consisting of heat pipes and fans [4]. All rooms with windows except kitchens and bathrooms in the demo buildings were equipped with RAHU, and their ventilation

rates were defined based on the European standard for ventilation requirements. The efficiency of heat recovery depends on the airflow rate of ventilation systems. Detailed properties of insulating breath membrane and RAHU are shown in Table 5.

Table 5. Properties of the renovation technologies in the ventilation package.

Renovation technology	Properties
Insulating breath membrane	Thermal conductivity [W/mK]: 0.029, Density [kg/m^3]: 96.15, Specific heat [J/kgK]: 2260, Thickness of insulating breath membrane [m]: 0.026, Airtightness (50% improvement) at 50 Pa [ACH]: 3.4, Airtightness (100% improvement) at 50 Pa [ACH]: 0.07 (Greece), 0.11 (Spain)
RAHU	Supply & Exhaust airflow rate [L/s]: Greece: Living room: 15/14 Bedroom: 8/7/4, Spain: Living room: 8 Bedroom: 5, Efficiency of heat recovery: Greece: Living room: 0.64/0.66 Bedroom: 0.76, Spain: Living room: 0.76 Bedroom: 0.76

Generation package

The generation package comprises two technologies: photovoltaic/thermal (PV/T) system and solar assisted heat pump (SAHP). PV/T system can convert solar radiation into usable thermal and electrical energy [9]. As the most important component, the PV/T panel combines photovoltaic solar cells with a solar thermal collector. In this study, to maximize the energy return within limited installation space, the maximum available area for PV/T panel installation was used in the simulation to reduce the purchased energy as much as possible. Besides, the appropriate size of the water tank were defined according to the heating capacity. SAHP is a heat pump in which solar collectors act as the evaporator in a single integrated system [10]. The solar collector operates more like an ambient heat exchanger than a solar thermal collector because it also transfers heat from ambient air through convection. It was placed on the roof of demo buildings to maximize the utilization of solar radiation. In order to cover as much heating demand as possible, the SAHP with maximum thermal generation capacity and the largest available water tank was tested in the simulations. The existing boilers were reserved as backup heaters for PV/T system and SAHP. Table 6 presents the properties of the PV/T system and SAHP in both demo buildings.

Table 6. Properties of the renovation technologies in the generation package.

Renovation technology	Properties
PV/T system	Conversion factor of solar thermal: 0.486, Loss coefficient a$_1$ [W/m^{2}K]: 4.028, Loss coefficient a$_2$ [W/m^{2}K]: 0.067, Electricity generation efficiency: 0.13, Area of PV/T panel [m^2]: 26 (Greece), 10 (Spain), Volume of hot water tank [m^3]: 1 (Greece), 1 (Spain)
SAHP	Total heating capacity [kW]: 11, COP: 4, Dimensions of each solar collector panel [m]: 2.1×0.81, Panel number: 4, Conversion factor η_0: 0.7, Loss coefficient a$_1$ [W/m^{2}K]: 4, Loss coefficient a$_2$ [W/m^{2}K]: 0.005

Results

Greek apartment building

Table 7 presents the breakdown of purchased energy, indoor temperature, and CO_2 concentration in the Greek apartment building before and after renovation when it was intermittently heated. Regarding the passive package, bio-aerogel thermal insulation, PV vacuum window and PCM brought 16%, 7% and 2% reduction in total purchased energy, respectively. In terms of the ventilation package, installing insulating breath membrane over the building envelopes reduced the total purchased energy by 15% or 16% when 50% or 100% airtightness improvement was assumed. As only 1% difference exists between two cases, increased airtightness has only a minor effect on energy, implying that the main energy efficiency impact came from the thermal insulation improvement. The installation of RAHU increased the space heating demand, which led to 7% increase in total purchased energy, while it also brought the CO_2 concentration, which has increased significantly due to the airtightness improvement, back to below 1200 ppm again. Replacing the existing heating system with PV/T system or SAHP could reduce the total purchased energy by 24% or 38%. The final combination including PV/T system conserves a larger energy saving potential, which reduced the total purchased energy by 49%, than the final combination including SAHP, which reduced the total purchased energy by 46%.

Table 7 also shows the simulated energy consumption and indoor climate when the demo building was continuously heated. Due to the increased heating demand when it was continuously heated, the demo building consumed more than double the purchased energy under the intermittent heating schedule. The total purchased energy was reduced by 44%, 9% and below 1% after renovation with bio-aerogel thermal insulation, PV vacuum window and PCM, respectively. The installation of insulating breath membrane has similar energy saving potential as bio-aerogel thermal insulation, which reduced the purchased energy by 44% and 46% with 50% and 100% airtightness improvement, respectively. Nevertheless, it has a negative impact on indoor air quality. Indoor CO_2 concentration was above 1800 ppm for half of the year due to the improved airtightness. Thus, after installing insulating breath membrane, equipping the Greek demo building with RAHU could ensure the CO_2 concentration always lower than 1200 ppm at the cost of a 10% increase in purchased energy. As for the generation measures, installing SAHP had a larger impact on building energy consumption (14% reduction) than PV/T system (22% reduction). Finally, renovation with the final combination including PV/T system or SAHP led to 66% or 65% decrease in total purchased energy.

The technologies aiming at improving thermal insulation performance (e.g., bio-aerogel thermal insulation, insulating breath membrane) brought much higher energy saving potential when the intermittent heating schedule was switched to the continuous heating schedule. As shown in Table 7, when it was intermittently heated, around 44% of

Table 7. Simulated energy consumption and indoor climate of the Greek apartment building with intermittent or continuous heating.

	Energy consumption			Indoor climate				
	Fuel [kWh/m²]	Elec [kWh/m²]	Total [kWh/m²]	T < 20 °C [%]	T > 25 °C [%]	T_max [°C]	CO_2 < 1200 [%]	CO_2 < 1800 [%]
	Greek apartment building with intermittent heating							
Ref	36.8	14.8	51.6	44.2	20.7	28.7	20.3	79.6
Ins	30.6	13.0	43.6	40.2	19.8	27.8	20.6	79.9
Ins+Win	27.9	11.7	39.6	34.3	24.4	28.6	20.8	80.8
Ins+Win+PCM	27.2	11.5	38.7	34.3	24.6	28.6	20.7	80.6
Mem 50%	30.9	13.1	44.0	40.0	19.9	27.8	12.8	66.4
Mem 100%	30.2	13.1	43.3	39.2	22.0	27.8	8.4	46.2
RAHU	32.1	14.6	46.7	42.5	19.5	28.2	100.0	100.0
PV/T	29.6	9.4	39.0	44.1	20.7	28.7	20.2	79.6
SAHP	0.0	32.0	32.0	44.2	20.7	28.7	20.3	79.6
Pas+Ven+PV/T	17.7	8.4	26.1	33.5	25.1	28.7	100.0	100.0
Pas+Ven+SAHP	0.0	27.8	27.8	33.2	25.1	28.7	100.0	100.0
	Greek apartment building with continuous heating							
Ref	109.3	18.2	127.5	0.6	0.0	25.0	21.7	79.7
Ins	56.5	14.3	70.8	0.9	0.0	25.0	21.4	80.2
Ins+Win	46.6	13.4	60	0.1	0.0	25.0	23.9	81.9
Ins+Win+PCM	45.9	13.4	59.3	0.0	0.0	25.0	23.6	81.7
Mem 50%	57.3	14.4	71.7	0.6	0.0	25.0	13.3	67.2
Mem 100%	54.2	14.4	68.6	0.5	0.0	25.0	10.4	48.6
RAHU	64.8	16.3	81.1	0.5	0.0	25.0	100.0	100.0
PV/T	99.2	10.0	109.2	0.0	0.0	25.0	22.0	61.8
SAHP	61.7	38.2	99.9	0.6	0.0	25.0	21.7	79.5
Pas+Ven+PV/T	35.7	7.5	43.2	0.4	0.0	25.0	100.0	100.0
Pas+Ven+SAHP	13.1	31.3	44.4	0.4	0.0	25.0	100.0	100.0

*Ref: Reference case before renovation; Ins: Bio-aerogel thermal insulation; Win: PV vacuum window; Mem 50%/100%: Insulating breath membrane with 50% or 100% airtightness improvement; RAHU: Room specific air handling unit with heat recovery; PV/T: Photovoltaic/Thermal system; SAHP: Solar assisted heat pump; Pas: All the technologies included in the passive package; Ven: All the technologies included in the ventilation package; T < 20 °C/T > 25 °C: Proportion of time indoor temperature is lower than 20 °C or higher than 25 °C; T_max: Maximum air temperature; CO_2 < 1200/1800: Proportion of time CO_2 concentration is lower than 1200 or 1800 ppm.

the year the indoor temperature was lower than 20 °C before renovation, while this proportion became much lower after renovating the building envelopes. It means that thermal insulation improvement led to the indoor temperature increase. However, when the building was continuously heated, indoor temperature was kept at a similar level before and after renovation. In addition, if the intermittent heating schedule was switched to the continuous heating schedule, although the absolute energy consumption reduction value became larger, the relative energy conservation potential of generation measures in measures could not cover the increased heating demand due to the extended heating time. The backup heating demand increased dramatically to satisfy the heating demand. The share of backup energy in total energy consumption became much higher than that of the utilized energy from generation measures when the Greek apartment building was continuously heated.

Spanish terraced house

As shown in Table 8, the renovation technologies affected the purchased energy and indoor climate at different levels when the Spanish terraced house was intermittently heated. Regarding the passive package, bio-aerogel thermal insulation, the most effective measure for energy saving, resulted in 43% purchased energy reduction, while PV vacuum window and PCM only brought 5% and 1% reduction, respectively. In terms of the ventilation package, installing insulating breath membrane over the building envelopes could reduce the total purchased energy by 35% and 36% when 50% and 100% airtightness improvement was assumed. The installation of RAHU increased electricity consumption and space heating demand, which

led to 8% increase in total purchased energy, while it ensured the CO_2 concentration was below 1200 ppm almost all year round. Replacing the existing heating system with PV/T system or SAHP could reduce the total purchased energy by 18% or 36%. The final combination including SAHP conserves a larger energy saving potential, which reduced the total purchased energy by 71%, compared with the final combination including PV/T system, saving the purchased energy by 66%.

Table 8 also shows the simulated building energy consumption and indoor climate before and after renovation when the heating schedule was switched to continuous heating. In terms of the passive package, the energy conservation potential brought by bio-aerogel thermal insulation, PV vacuum window and PCM was 45%, 6% and less than 1% reduction, respectively. As for the ventilation package, installing insulating breath membrane over building envelopes could reduce the total purchased energy by 37% when the airtightness was improved by 50% and 38% when the airtightness was improved by 100%. The installation of RAHU ensured CO_2 concentration below 1200 ppm almost year-round at the expense of increased electricity consumption and space heating demand, 9% increase in total purchased energy. The total purchased energy was reduced by 14% or 36% when the existing heating system was replaced with PVT system or SAHP. The final combination including SAHP saved more energy, 73% reduction in total purchased energy, than the final combination including PV/T system, saving the purchased energy by 65%.

As the intermittent and continuous heating schedules applied in the Spanish terraced house were quite similar, the energy conservation potential of thermal insulation

Table 8. Simulated energy consumption and indoor climate of the Spanish terraced house with intermittent or continuous heating.

	Energy consumption			Indoor climate				
	Fuel [kWh/m²]	Elec [kWh/m²]	Total [kWh/m²]	T < 18 °C [%]	T > 25 °C [%]	T_max [°C]	CO₂ < 1200 [%]	CO₂ < 1800 [%]
Spanish terraced house with intermittent heating								
Ref	115.0	19.4	134.4	5.1	11.9	30.5	41.3	98.1
Ins	58.0	19.3	77.2	0.0	11.4	29.6	43.9	98.6
Ins+Win	51.1	18.2	69.3	0.0	10.1	29.1	44.6	98.8
Ins+Win+PCM	50.2	18.2	68.4	0.0	10.5	28.5	45.4	98.9
Mem 50%	68.1	19.3	87.4	4.6	12.4	29.9	35.8	97.9
Mem 100%	67.2	19.3	86.5	0.0	12.0	30.2	24.2	95.7
RAHU	77.5	19.8	97.3	0.2	9.9	30.2	99.5	100.0
PV/T	97.1	12.5	109.6	5.1	11.7	30.4	41.2	98.1
SAHP	45.6	39.8	85.4	5.1	11.8	30.4	41.2	98.1
Pas+Ven+PV/T	33.1	12.7	45.8	0.0	8.3	28.3	99.5	100.0
Pas+Ven+SAHP	5.9	33.3	39.2	0.0	8.3	28.3	99.5	100.0
Spanish terraced house with continuous heating								
Ref	145.5	19.4	164.9	0.0	9.9	30.5	43.8	98.2
Ins	72.2	19.3	91.5	0.0	9.3	29.6	47.0	98.8
Ins+Win	62.9	18.1	81	0.0	8.2	29.1	48.3	98.9
Ins+Win+PCM	62.1	18.1	80.2	0.0	8.4	28.5	49.4	99.0
Mem 50%	84.5	19.3	103.8	0.0	9.8	30.2	36.7	97.9
Mem 100%	83.6	19.3	102.9	0.0	9.9	30.2	24.5	96.5
RAHU	97.9	19.8	117.7	0.0	8.2	30.2	98.4	100.0
PV/T	128.6	12.4	141	0.0	9.9	30.4	43.9	98.2
SAHP	60.6	44.4	105	0.0	9.9	30.4	43.9	98.2
Pas+Ven+PV/T	45.6	12.7	58.3	0.0	6.7	28.4	98.4	100.0
Pas+Ven+SAHP	6.5	37.7	44.2	0.0	6.4	28.3	98.4	100.0

measures only increased by 1-2% when the intermittent heating schedule was switched to the continuous heating schedule. The space heating demand before renovation increased by 25%, which was much lower than that in the Greek demo building, if the continuous heating schedule replaced the intermittent heating schedule. Thus, the energy-saving potential of generation technologies in the continuously heated Spanish demo building was only up to 2% lower than their energy conservation potential in the intermittently heated Spanish demo building.

Discussion

In addition to the simulated impact of renovation technologies on energy consumption and indoor climate, whether a renovation technology is feasible for the actual plan also depends on the economical analyzation of the technologies. However, the investment analysis and life cycle cost calculation of renovation technologies are not included in the study.

The renovation technologies chosen according to the simulation results and economical analyzation will be implemented in the real retrofit of the demo building later. Real-time monitoring will be utilized to evaluate simulation accuracy and improve operational performance by using advanced control algorithms. The measurements will be used for model validation and development in the future.

Conclusions

The recommendation priority of renovation measures was concluded based on the simulation results under the same heating schedule. In terms of the passive package, insulating the external walls and roof with bio-aerogel is the most recommended measure for energy conservation, while the installation of PV vacuum windows and PCM only has a slighter impact on energy consumption (up to 10% reduction). As a passive technology included in the ventilation package, insulating breath membrane has a similar energy saving potential to bio-aerogel thermal insulation and a negative impact on indoor air quality due to the improved airtightness. Considering about the indoor air quality issue, it is necessary to install RAHU after renovating the building envelopes with insulating breath membrane. Regarding the generation measures, the energy saving potential of PV/T system and SAHP varied considerably across different southern European demo buildings, which was 14-24% and 22-38%, respectively. The choice of generation measure depends on the actual conditions of the demo buildings. Finally, the maximum energy saving with the final combinations was up to 66% and 73% in the Greek and Spanish demo buildings when continuously heated.

The energy conservation potential of renovation technologies was effectively affected by the heating schedules applied in the demo buildings. Commonly, the building energy efficiency achieved with thermal insulation improvement measures (e.g., bio-aerogel thermal insulation, insulating breath membrane etc.) was diminished when the continuous heating schedule was switched to the intermittent heating schedule. When the demo buildings were continuously heated, most of time indoor temperature was basically maintained at heating setpoint before and after improving thermal insulation performance. However, when they were intermittently

heated, considerable proportion of time indoor temperature was lower than the heating setpoint due to the short heating period before renovation. Thus, although thermal insulation was improved significantly after renovation, the heating system still works at a high power to approximate the heating setpoint which means the space heating demand was not reduced as much as that in the continuously heated building. In brief, partial of the energy conservation potential brought by thermal insulation improvement was sacrificed for the improved indoor air temperature.

If the intermittent heating schedule was switched to the continuous heating schedule, the absolute energy consumption reduction brought by generation technologies increased, while the relative energy conservation potential in percentage became lower. The space heating demand is much higher under a continuous heating schedule than that under an intermittent heating schedule. The higher the space heating heat demand the lower the proportion of demand covered by generation measures and higher the proportion of backup heating demand. The energy conservation potential of generation measures lowered down following the increased ratio of backup heating demand.

REFERENCES

1   EURIMA - New and Existing Buildings, 2018. Eurima.

2   Renovation Wave, 2020. European Commission.

3   H. Jarimi et al., "Performance Analysis of a Hybrid Thin Film Photovoltaic (PV) Vacuum Glazing", *Future Cities and Environment*, vol. 6, no. 1, Art. no. 1, March 2020.

4   G. Barreto, K. Qu, Y. Wang, M. Iten, and S. Riffat, "An innovative window heat recovery (WHR) system with heat pipe technology: Analytical, CFD, experimental analysis and building retrofit performance", *Energy Reports*, vol. 8, pp. 3289–3305, November 2022.

5   TABULA WebTool, 2015.

6   J. Feijó-Muñoz, R. A. González-Lezcano, I. Poza-Casado, M. Á. Padilla-Marcos, and A. Meiss, "Airtightness of residential buildings in the Continental area of Spain", *Building and Environment*, vol. 148, pp. 299–308, January 2019.

7   Thermal_storage_catalogue, 2021. PCM Products.

8   Skytech-Pro-XL-Non-combustible-and-insulating-breather-membrane, 2021. Winco-Tech.

9   D. Das, P. Kalita, and O. Roy, "Flat plate hybrid photovoltaic-thermal (PV/T) system: A review on design and development", *Renewable and Sustainable Energy Reviews*, vol. 84, pp. 111–130, March 2018.

[10] B. J. Huang and J. P. Chyng, "Performance characteristics of integral type solar-assisted heat pump", *Solar Energy*, vol. 71, no. 6, pp. 403–414, December 2001.

Modeling and Simulation of the Operation of Photovoltaic System for Meeting Electricity Consumption of Residential House Consumers, Including Electric Vehicle

Novak Popović, novakpopovickg4@gmail.com (menthor: Novak Nikolić, novak.nikolic@kg.as.rs)
Faculty of Engineering, University of Kragujevac, presented: September 2022.

Abstract— **In this paper, the sizing of the solar photovoltaic (PV) system which would meet the total yearly electricity needs of the existing single-family residential house in the territory of the city of Kragujevac (Serbia), was carried out. Two cases were considered. In the first case (case 1), the solar system would produce electricity that corresponds to the actual yearly electricity consumption of the existing electricity consumers in the house. On the other hand, in case 2, the basis for the system sizing would be the sum of the consumption of existing consumers and electricity consumption of the electric vehicle (EV). The energy and economic performance of the house with and without EV load were evaluated. Its energy behavior was simulated for real weather data by using EnergyPlus software. According to the simulation results, the shortest payback period for the installation of the PV system in case 1 is 6 years, and in case 2, for the installation of the PV system and purchasing an EV is 19 years.**

Index Terms— **PV panel, electricity, electric vehicle, EnergyPlus, simulation**

Introduction

Electric vehicle (EV) will become an important component of household energy consumption globally under the plans to replace cars based on internal combustion engines [1]. The vehicle electrification is conceived as vehicle efficiency improvement [2]. The EV usage gives new hope that they can represent an alternative that is more likely to support not only the development of sustainable transport, but sustainable development in the broadest sense [3]. Well-built infrastructure for recharging the EV batteries is considered as one of the key issues for the success of the EV, in addition to their price [4]. Many studies indicate that the most important location for EV charging is at home, followed by work, and then public locations. [5]. According to Ref. [6] 45% of the private EV owners say they would charge their EV using renewable energy source either via rooftop solar panels (PV panels) and household battery (31%) or via an electricity contract which utilises green power or carbon offset (14%). The demand of PV panels and EV is expected to increase in the future. An example of their simultaneous growth is represented by the Californian market, where about 40% of EV owners also own solar PV systems [7]. Kobashi and Yarime [8] found that the integration of PV and EV technology would reduce yearly energy costs by 68% and CO_2 emissions by 92% in 2030 of households in Japan.

Manns [9] conducted a techno environmental analysis of the German multi-family buildings with rooftop PV systems and EV charging stations. He revealed that 2 to 4 tonnes of CO_2-equivalent emissions can be saved annually per residential home, depending on the building size (number of flats). Chowdhury et al. [10] optimized the operation of the existing PV system installed in the Institute of Energy of Dhaka University that would be integrated with the EV. It was concluded that 21% of the total electricity production can be used for EV charging thus reducing greenhouse gas emissions by 52,944 kg/year. The EV charging substantially affects the optimal size of the PV system for self-production and self-consumption of electricity. Piazza et al. [11] considered the impact of the electric mobility on the optimal design of a PV system. The developed optimization model applied to the campus building of the University of Genova demonstrates that the presence of EV increases the optimal size of the PV system from 15% to 25%. Munkhammar et al. [12] studied the impact of the EV charging on the size of a PV system within a net-zero energy building (NZEB) in Sweden. It was revealed that the integration of EV and residential house caused the increase of the yearly household electricity load and PV system size by 37%. Two existing single-family houses located in Netherlands and Belgium that meet NZEB standards (PV system installed) were used to analyze the energy and environmental performance of the building with and without EV load [13]. It was shown that the house with EV load can have 27 to 95% higher energy demands but lower total emissions by 11 to 35%. The effect of EV home charging and PV electricity production on the household electricity use as a future scenario in the city of Westminster was investigated in [14]. According to the obtained results the EV charging leads to the increase of the household electricity use by 14% to 61% depending on the number of occupants. Also, it was pointed out that the EV charging hours should be synchronized with the hours of PV electricity production. A small-scale PV system could be profitable if its investment costs are low or subsidies are provided [15]. The territory of the Republic of Serbia has quite satisfactory conditions for the exploitation of resources obtained from the Sun, with yearly solar radiation reaching around 1400 kWh/m2 [16]. Low electricity prices in Serbia extend the simple payback period (SPB), making investing in the solar PV system a questionable decision. The incentive in the form of a state subsidy made this procedure more affordable by lowering investment costs and reducing the SPB.

Preradović [17] compared the solar energy potential of six different cities, in six different countries, Freiburg (Germany), Graz (Austria), Maribor (Slovenia), Banja Luka (Bosnia and Herzegovina), Niš (Serbia), and Athens (Greece). The results show that Athens has the highest potential for solar energy production with 2108.31 kWh/m2 of yearly solar radiation, and that Niš stands second with 1662.62 kWh/m2. It was concluded that SPB is the shortest for the countries where the electricity price is the highest and vice versa. In other words, in Germany the SPB for installed PV system is the shortest, and in Serbia the longest.

Unfortunately, there are no publications concerning the energy and economic viability of a system consisting of the grid-connected rooftop PV and EV within the residential house in the Serbian climatic conditions. The contribution of this paper refers to the answer to the question of whether a small-scale PV system is profitable in the current conditions of the Serbian electricity and EV market. As an example, a household in the city of Kragujevac was chosen. This analysis was carried out for two cases. Case 1 implies the installation of a PV system for a household without EV charging, while case 2 will provide the calculation for the chosen household but which includes EV load. For both cases the size of the PV system and SPB were determined.

1. Methodology

The software used in this paper enabled the realization of all the necessary tasks. For the creation of the 3D model of a residential building the software "SketchUp2016" was selected [18]. Using the tools of the "Open Studio" software, a 3D model from the "SketchUp2016" was inserted into the "EnergyPlus" software, in which the sizing and simulation of the PV system were carried out [19]. Geometric models of the household buildings were made on the basis of already existing buildings, located on the territory of the city of Kragujevac. They are two separate buildings (Fig. 1), a residential house and an auxiliary building, both consisting of two floors and an attic, and representing the home of a family of five. The position of the surface on which the PV panels should be installed (roof of the auxiliary building) is determined by orientation of 200° and tilt angle of 39.1°. This angle approximately corresponds to the yearly optimal tilt angle of the solar collector, of 37.5°, for the city of Kragujevac. The average monthly household electricity consumption, calculated on the basis of the actual electricity bills, is about 500 kWh.
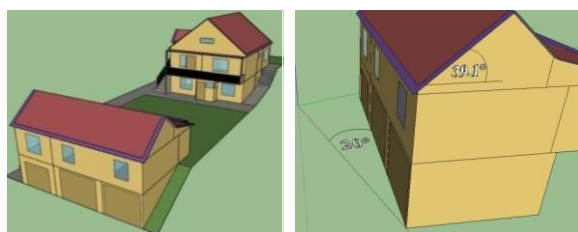

Figure 1. Isometric view of the analyzed residential and auxiliary building (left) and position of the auxiliary building selected for PV system installation (right)

When choosing the EV, an analysis of the entire market was carried out. Preference was given to those with the highest possible range, the highest possible efficiency and the lowest possible price. The analysis was performed for new vehicles that can serve as a car for a family of five. The vehicle currently owned by the household is "Citroën C4", whose dimensions served as a reference value when choosing an EV. It was decided that the electric car most suitable for this household is the "Volkswagen ID.3 Pro S". The specifications of this car are given in Table 1 [20], while in Fig. 2 its appearance and dimensions are shown.

Table 1. Specifications of the adopted EV [20]

Battery capacity (100%) (kWh)	Useful battery capacity (60%) (kWh)	Average efficiency (Wh)	Range (km)
82	49.2	171	450
Top speed (km/h)	Power (kW)	Charging time (100%) (h)	Charging time - fast charger (70%) (h)
160	150	8h 15min	71 min

The price of the vehicle is 43,603.00 €.

Figure 2. Appearance and dimensions of the adopted EV [21,22]

In order to make the investigation results as comprehensive as possible, the investigation will be conducted in two cases. Case 1 represents a case in which the calculation will be based on the existing current electricity consumption of the residential building without an EV. In Case 2, the total electricity consumption of residential building consumers, which include an EV, is considered.

For the purposes of the PV system sizing, it is necessary to determine the amount of electricity that the system should cover. In order to be able to carry out this procedure, the PV panel was first selected.

The PV panel, adopted after market analysis, is a panel from the German manufacturer "LUXOR" under the name "Solar ECO Line HC BF M120 375W" [23]. The adopted average panel efficiency is based on the information provided in the technical documentation. The specifications of the selected PV panel, are presented in Table 2.

After choosing the PV panel, it is necessary to draw a surface corresponding to the dimensions of that PV panel (1.755 m × 1.038 m) within the 3D building model. This model is imported into the EnergyPlus software, in which the simulation of the PV panel operation for the period of one year is carried out. To simulate weather conditions of the city of Kragujevac (latitude of 44.02˚N, longitude of 20.92˚E) the EnergyPlus weather file was used. Through simulations, it was obtained that the total yearly produced electricity of the selected panel is 664.57 kWh. This data affects the size of the PV system.

Table 2. Specifications of the adopted PV panel [24]

Power (W)	Efficiency (%)	Average efficiency (%)	Lifetime (years)
375	20.94	19.09	25
Warranty (years)	Temperature range (˚C)		Area (m²)
15	-40 to 85		1.82

Unlike case 1, in case 2 the total electricity consumption also depends on the consumption of electricity necessary to charge the battery and drive the EV. Its consumption is determined on the assumption that the vehicle is used for half of the year, i.e. in the winter and summer months, in harsh operating conditions when the heating and air conditioning system is used (ambient temperature lower than -10˚C (winter) and higher than 26˚C (summer)), and the rest of the year in ideal conditions. Due to the lack of data, it was assumed that the behavior of the car battery in winter and summer operating conditions is the same. Ideal conditions imply vehicle operation at an outdoor temperature of 23˚C without operation of the heating and air conditioning system. Car battery capacity is recommended never to be charged above 80% and never discharged below 20%, which reduces the battery capacity by 40% [25]. Also, on the basis of the household needs, it was adopted that the daily distance travelled by car is 40 km (Table 3). The value of the average yearly consumption for case 2 is calculated according to the data taken from [20]. Data on consumption per kilometer for both harsh and ideal conditions are multiplied by the daily travelled distance, whereby the average daily consumption of the vehicle in these conditions is obtained. The number of days in harsh and ideal conditions is obtained by summing the number of days in the months for which these operating conditions apply. The product of the number of days in certain conditions with thedaily consumption for those conditions gives a number that represents the total consumptionfor part of the year in those conditions, so

the sum of consumption in ideal months and consumption in harsh months gives the total yearly consumption in case 2. If the yearly consumption is divided by the number of months, the average monthly consumption of an EV is obtained. Dividing this value by the battery capacity gives the number of charges per month, that is, the time spent on the charger during one month. It is possible to calculate the car range if the battery capacity is divided by the average efficiency of the battery. The average efficiency is determined by dividing the yearly consumption of an EV by the product of the number of days in a year and the distance travelled on a daily basis (Table 3).

Table 3. Calculation of the vehicle operational characteristics (case 2)

Battery capacity (100%) (kWh)	Battery capacity (60%) (kWh)	Daily distance traveled (km)	Consumption per km in ideal conditions (kWh/km) [20]
82	49.2	40	0.148
Daily consumption in ideal conditions (kWh)	Consumption per km in harsh conditions (kWh/km) [20]		Daily consumption in harsh conditions (kWh)
5.92	0.203		8.12
Number of days in ideal conditions	Number of days in harsh conditions	Yearly consumption (kWh)	Average monthly consumption (kWh)
183	182	2561.2	213.43
Number of battery charges during a month	Average consumption per km (kWh/km)		Range with full battery (km)
4.34	0.175		280.46

3. Results and discussion

3.1. Size of the PV system

As already explained, the size of the PV system is determined by the total yearly consumed electricity of the considered residential building (for the appropriate case) and the total yearly produced electricity of one PV panel (Table 4). For case 1, it was found that the required number of PV panels is 10 (Fig. 3 (left)). The required number of PV panels in case2, calculated according to the values of the parameters shown in Tables 3 and 4, is 13 (Fig. 3 (right)) (Table 4). Based on the number of PV panels, the appropriate power of the inverter is adopted, which efficiency is also taken into account during the simulation of the PV system operation (Table 4).

Table 4. Size of the PV system for both cases

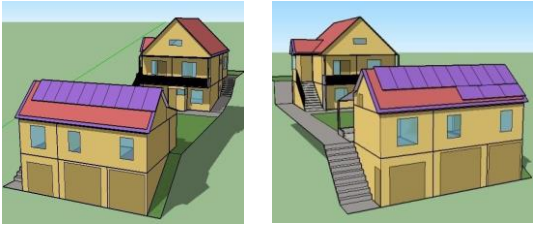| Case	Yearly electricity production of one PV panel (kWh)	Total electricity consumption (kWh)	Number of PV panels
1	664.57	6027.96	9.07
2	664.57	8591.23	12.93
Case	Adopted number of PV panels	Inverter power (W)	Inverter efficiency (%)
1	10	4200 [26]	97.60% [26]
2	13	5000 [27]	97.50% [27]

Figure 3. 3D models of a residential house with the required number of PV panelsfor case 1 (left) and case 2 (right)

Figure 4 shows a diagram of the electricity production and consumption in both cases.As a reminder, electricity consumption was adopted on the basis of the actual household bills, and it can be concluded that it is the lowest during the summer months and the highest during the winter months. The difference between consumption in case 2 and case 1 corresponds to the amount of electricity needed to charge the EV battery, while the difference in production between these two cases exists because of the higher number of PV panels adopted in case 2. Electricity production in both cases has a completely opposite pattern of behavior in relation to its consumption during the year. The highest production occurs during the summer months, when the intensity of direct solar radiation is high and the share of diffuse radiation in the total radiation is small, while the lowest production is during the winter months. The total amount of produced electricity is 6645.65 kWh, which exceeds the needs for the same by about 600 kWh, while in the second case it is equal to 8639.35 kWh, with a surplus of about 50 kWh.

hands over the surplus to the network, is called a prosumer. Before becoming a prosumer, the buyer of electricity can apply for a subsidy for the PV system installation. Subsidies represent financial assistance from the state for investments by citizens in which the state has an interest. Subsidies for the installation of PV systems, provided by the Republic of Serbia, cover 50% of the total investment costs, with the condition that the maximum power of the system for which these privileges can be realized is 6 kW [28]. It is also important to note that in case 2, the right to a subsidy for purchasing an EV, which amounts to €5,000.00 for the fully EV, can be earned, too [29].

In Table 5 the yearly costs of electricity after the PV system installation are given. Based on the actual consumption bills, total household electricity costs amount to 40,208.00 RSD. These costs are calculated without including additional costs in the form of fees to the supplier. As they do not disappear after the installation of the PV system and it is impossible to predict them, for the purposes of this work, their influence is not considered. Theprinciple of calculating electricity costs after installing a PV system is as follows. In months when consumption exceeds production, electricity costs will be calculated based on the amount of electricity consumed under the lower tariff increased by the difference between the electricity consumed under the higher tariff and the electricity produced.

The electricity prices of the corresponding zone in the corresponding tariff are adopted according to [30]. In months when production exceeds consumption, or they are equal, electricity costs will be calculated based on the electricity consumed within the lower tariff.
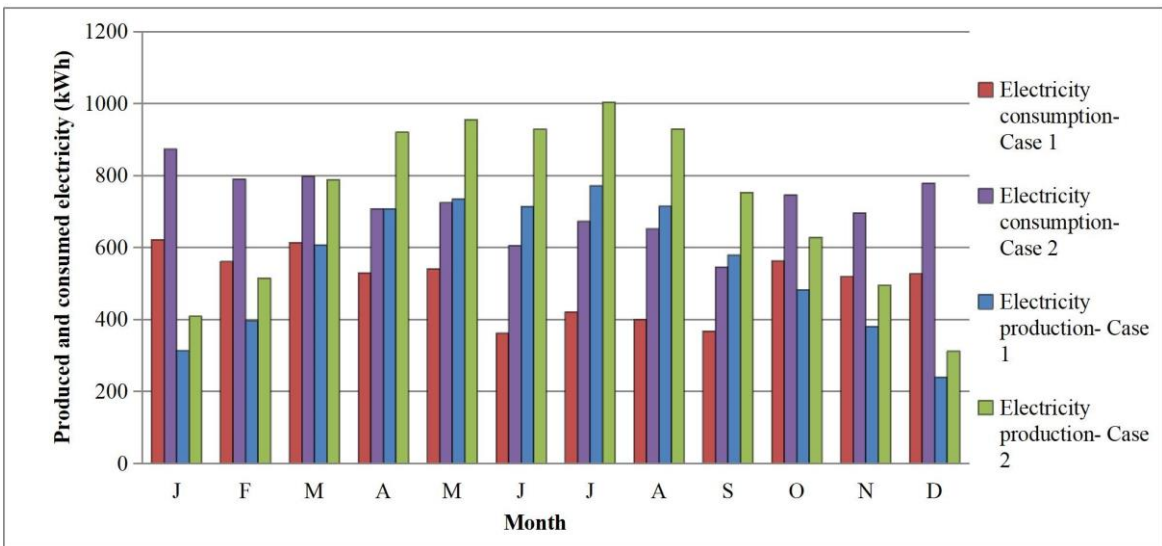

Figure 4. Monthly electricity consumption and production in both considered cases

3.2. Cost-effectiveness analysis

Before analyzing the profitability of installing the system, a couple of terms should be defined. First of all, it is necessary to clarify what is behind the term prosumer. A buyerof electricity who produces electricity from renewable energy sources within his facility, uses the produced electricity to meet his own needs, and

According to [31], the unused part of electricity can be carried over to the next month and used in months when the production does not meet the consumption until 1st of April of the next year.

Table 5. Monthly electricity costs in both considered cases (1 € = 118 RSD)

Month	Production (kWh)		Consumption- higher tariff (kWh)		Consumption- lower tariff (kWh)		Difference between produced and consumed electricity at the end of the month (kWh)		Cost of electricity for both cases (RSD)
	Case 1	Case 2	Case 1	Case 2	Case 1	Case 2	Case 1	Case 2	
A	708	920	406	584	124	124	302	337	267.22
M	735	955	404	588	137	137	633	704	295.24
J	714	929	276	520	86	86	1071	1113	185.33
J	772	1004	400	652	21	21	1443	1466	45.26
A	715	930	326	578	74	74	1832	1818	159.47
S	579	753	302	480	66	66	2109	2092	142.23
O	483	628	450	634	113	113	2142	2086	243.515
N	381	495	403	581	116	116	2120	2001	249.98
D	240	312	395	647	132	132	1965	1666	284.46
J	314	409	486	738	136	136	1793	1337	293.08
F	396	515	439	668	122	122	1750	1184	262.91
M	607	789	464	648	150	150	1893	1325	323.25
Sum	6646	8639	4751	7314	1277	1277	1893	1325	2,751.95

From Table 5 and Fig. 4, it can be concluded that electricity production meets consumption in all months. The calculation results also indicate a problem related to the system oversizing. Guided by the idea that the system should have as many solar panels as necessary to meet the yearly electricity consumption, a mistake is being made. Since the produced electricity can be used only in the tariff in which it was produced, which is certainly only within the higher tariff, the electricity consumed in the lower tariff should then be excluded from the calculation. Also, according to [20], after 1st of April all the unused electricity is actually "gifted" to electricity provider, which further complicates the system sizing. From the table above, it can be concluded that the system is oversized in the first case by almost 3 PV panels and in the second by almost 2 PV panels. Investment costs for both cases are given in Table 6.

Table 6. Investment costs for both considered cases in thousands of RSD (1 € = 118 RSD)

PV panel price (in 000 RSD) [24]		Inverter price (in 000 RSD) [26][27]		Roof truss price (in 000 RSD) [32]	
Case					
1	2	1	2	1	2
220.66	286.86	75.00	118.80	38.72	52.34
Price of other elements and system mounting (in 000 RSD) [33]		Price of smart electricity meter (in 000 RSD) [34]		Price of EV with subsidy (in 000 RSD) [20]	
Case					
1	2	1	2	1	2
65.00		44.35		0	5,113.52

According to Table 6, the total cost of installing the PV system for case 1 is 443,735.00 RSD without subsidy and 221,867.50 RSD with subsidy. In case 2, the installation cost without subsidy amounts to 5,094,493.92 RSD, and with the subsidy for the installation of the PV system, 4,810,821.42 RSD. The subsidy for buying the

selected EV is 586,372.68 RSD [29]. A few more things need to be emphasized. As the EV is charged using electricity produced within the home, its charging is free (if the vehicle is charged within a higher tariff). Therefore, the fuel savings are equal to the yearly fuel costs for the currently used household car, which are 190,530.00 RSD. Also, the price of the EV, which is a replacement for the mentioned vehicle, can be reduced by the market value of that car, which is 410,789.00 RSD. When all the necessary parameters are calculated, the SPB can be determined. For case 1, the SPB without the participation of the state in the form of subsidy for the installation of solar PV system is 11 years, 10 months and 4 days, while with the subsidy it is 5 years, 11 months and 2 days. For case 2, the SPB without the subsidy amounts to 20 years, 6 months and 15 days, while with the subsidy it amounts to 19 years, 3 months and 18 days.

4. Conclusion

In this paper, the sizing of the solar PV system which would meet the total yearly electricity needs of a residential house in the territory of the city of Kragujevac, was carried out. Two cases were considered. In the first case (case 1), the solar system would produce electricity that corresponds to the actual yearly electricity consumption of the existing electricity consumers in the house. On the other hand, in case 2, the basis for the system sizing would be the sum of the consumption of existing consumers and electricity consumption of the EV. Sizing was preceded by the creation of a 3D house model in the software "SketchUp2016" and a PV panel model in the software "EnergyPlus", in which its energy behavior was simulated for real weather data for the city of Kragujevac. According to the simulation results, the shortest payback period for the PV system installation in case 1 is 6 years, and in case 2, for the installation of the PV system and purchasing an EV is 19 years. Certain assumptions were adopted before making the calculations. The efficiency of the solar PV panel of 19.09% is adopted

as average and constant for 25 years, which means that in the first half of its life time the efficiency of this panel will be slightly lower, while in the second half it will be higher. In reality, it will be lower and variable due to operating conditions that differ from the test conditions of the PV panel. In this regard, the influence of temperature and soiling of the receiving surface of the panel on its efficiency was neglected. Also, it was adopted that the habits of the householders do not change. After installing the PV system, using the large electricity consumers within the lower tariff becomes the most unprofitable option. Regarding case 2, it can be noticed that EV prices still are not low enough, or in other words, the efficiency and range of cheaper ones are not yet satisfactory. Since it is a still rising technology, a drop in the price and an improvement in the car characteristics can be expected. Also, the PV panel technology development is on the rise, so in the future their profitability for both cases could be shorter. According to the currently available data on electricity bills, recently sent to households that received the status of prosumer, it seems that the sizing of the PV system according to the total yearly electricity needs is wrong, that is, the system is oversized. The reason for this lies in the calculation of electricity consumption within the lower tariff and the fact that the prosumer loses the possibility of using "accumulated" electricity produced from previous months after 31st of March. The solution to this problem would be a purposeful increase in electricity consumption by installing electric heating systems (heat pump…), where the investment would pay off in another field. On the other hand, a potential solution to the problem would be the possibility of calculating the "accumulated" produced electricity in the next accounting period or meeting the electricity consumed in a lower tariff (at night), with the cancellation or reduction of the corresponding fees. Due to the impossibility of determining the amount of fees and charges that increase the amount of the bill, there was not much to say about it.

5. References

1 International Energy Agency. Global EV Outlook 2020. (2020). Available: https://www.iea.org/reports/global-ev-outlook-2020 (accessed 10.07.2022.)

2 Belingardi, G., Amati, N., & Bonfitto, A.: ELECTRIC AND HYBRID VEHICLES: ARE WE READY FOR THE NEW MOBILITY ERA?; vol. 47, no. 2, Mobility & Vehicle Mechanics, 2021.

3 Kjosevski, S., Kochov, A., Kostikj, A.: AN INDICATORS BASED APPROACH TOWARDS DECISION MAKING AND POLICY MAKING REGARDING INTRODUCING ELECTRIC VEHICLES; vol. 45, no. 4, Mobility & Vehicle Mechanics, 2019.

4 Gruden, D.: WILL ELECTRIC MOTOR SUBSTITUTE INTERNAL COMBUSTION ENGINE?; vol. 45, no. 4, Mobility & Vehicle Mechanics, 2019.

5 Hardman, S., Jenn, A., Tal, G., Axsen, J., Beard, G., Daina, N., ... & Witkamp, B.: A review of consumer preferences of and interactions with electric vehicle charging infrastructure.; vol.62, 508-523, Transportation Research Part D: Transport and Environment, 2018.

6 Electric Vehicle Council. State of Electric Vehicles. (2020). Available: https://electricvehiclecouncil.com.au/reports/state-of-electric-vehicles-2020/ (accessed 12.06.2022.)

7 Buonomano, A.: Building to Vehicle to Building concept: A comprehensive parametric and sensitivity analysis for decision making aims.; vol. 261, 114077 Applied Energy, 2020.

8 Kobashi, T., & Yarime, M.: Techno-economic assessment of the residential photovoltaic systems integrated with electric vehicles: A case study of Japanese households towards 2030.; vol. 158, 3802-3807, Energy Procedia, 2019.

9 Manns, P. (2019). A techno-environmental analysis on the effect of combining EV charging stations with PV tenant law systems and subsidies on the reduction of greenhouse gas emissions. Available: https://www.researchgate.net/publication/341151178 (accessed 18.07.2022.)

[10] Chowdhury, N., Hossain, C. A., Longo, M., & Yaïci, W.: Optimization of solar energy system for the electric vehicle at university campus in Dhaka, Bangladesh. vol. 11(9), 2433. Energies, 2018.

11 Piazza, G., Bracco, S., Delfino, F., Di Somma, M., & Graditi, G.: Impact of electric mobility on the design of renewable energy collective self-consumers.; 100963 Sustainable Energy, Grids and Networks, 2022.

12 Munkhammar, J., Grahn, P., & Widén, J.: Quantifying self-consumption of on-site photovoltaic power generation in households with electric vehicle home charging. vol. 97, 208-216, Solar energy, 2013.

13 Rehman, H. U., Diriken, J., Hasan, A., Verbeke, S., & Reda, F.: Energy and Emission Implications of Electric Vehicles Integration with Nearly and Net Zero Energy Buildings. vol. 14(21), 6990, Energies, 2021.

14 Munkhammar, J., Bishop, J. D., Sarralde, J. J., Tian, W., & Choudhary, R.: Household electricity use, electric vehicle home-charging and distributed photovoltaic power production in the city of Westminster. vol. 86, 439-448, Energy and Buildings, 2015.

15 Koskela, J., Rautiainen, A., & Järventausta, P.: Using electrical energy storage in residential buildings–Sizing of battery and photovoltaic panels based on electricity cost optimization. vol. 239, 1175-1189, Applied energy, 2019.

16 Pavlovic, T. (Ed.).: The Sun and Photovoltaic Technologies. Springer Nature, 2019.

17 Preradović, M.: Solar energy potential in Freiburg, Graz, Maribor, Banja Luka, Niš, and Athens. vol. 35(3), 393-403 Facta Universitatis, Series: Electronics and Energetics, 2022.

18 https://www.sketchup.com/try-sketchup (accessed 20.08.2022.)

19 http://nrel.github.io/OpenStudio-user-documentation/ (accessed 20.08.2022.)

20 https://ev-database.org/car/1534/Volkswagen-ID3-Pro-S---5-Seats (accessed 23.08.2022.)

21 https://insideevs.com/news/401952/more-details-vw-id3-revealed/ (accessed 23.08.2022.)

22 https://vrelegume.rs/prva-voznja-i-utisci-volkswagen-id-3/ (accessed 23.08.2022.)

23 https://www.suncica.co.rs/solarni-paneli-i-oprema/solarni-paneli/solarni-monokristalni-panel-luxor-410w-hlafcut.html (accessed 23.08.2022.)

24 https://www.suncica.co.rs/pub/media/wysiwyg/Luxor_375W.pdf (accessed 22.08.2022.)

25 https://dmotion.rs/2021/03/10/koliko-su-izdrzljive-baterije-u-elektricnim-automobilima/ (accessed 23.08.2022.)

26 https://www.solar-shop.rs/proizvodi/solarni-on-grid-inverter-growatt-mic-3000-tl-x/ (accessed 22.08.2022.)

27 https://www.solar-shop.rs/proizvodi/solarni-on-grid-pretvarac-growatt-min-5000tl-xe/ (accessed 22.08.2022.)

28 https://balkangreenenergynews.com/rs/raspisan-konkurs-za-subvencije-za-solarne-panele-za-domacinstva-u-deset-gradova-u-srbiji/ (accessed 29.08.2022.)

29 https://plutonlogistics.com/drumski-transport/subvencije-za-kupovinu-elektricnih-i-hibridnih-vozila-i-u-2022-podsticaji-do-5-000-evra/ (accessed 29.08.2022.)

30 https://www.eps.rs/cir/snabdevanje/Documents/20220722_Odluka%20o%20ceni.pdf (accessed 30.08.2022.)

31 https://balkangreenenergynews.com/rs/srbija-usvojila-uredbu-o-prozjumerima-u-tri-koraka-do-struje-iz-solarnih-panela/ (accessed 24.08.2022.)

32 https://www.solarni-paneli.co.rs/pdf/cenovnik-solarnih-panela.pdf (accessed 22.08.2022.)

33 https://www.suncica.co.rs/solarni-sistemi/on-grid-solarni-sistemi.html (accessed 30.08.2022.)

34 https://qubino.com/products/3-phase-smart-meter/#buy3phasesmartmeter (accessed 30.08.2022.)

Thermal comfort and indoor air quality in schools: analysis of students' perception and impact of perceived control on their satisfaction

Author: Giulia Torriani[1,2] (giulia.torriani@eurac.edu)
Supervisors: Fabio Fantozzi[1](fabio.fantozzi@unipi.it), Giulia Lamberti[1](giulia.lamberti@phd.unipi.it),
Francesco Babich[2] (francesco.babich@eurac.edu)
2021/2022

In educational buildings, ensuring indoor comfort is crucial in guaranteeing pupils' health and high learning. Only a few studies have simultaneously investigated all educational stages and considered schools and universities in different areas. In this Master Thesis work, data collected from 24 classrooms in the winter and 1548 questionnaires were used to analyse thermal comfort and Indoor Air Quality (IAQ) perception in all the educational stages in one region, thus minimising the possible bias associated with the climate zone and cultural adaptation. The results showed that adaptive capacities, such as clothing insulation and window operation, decrease at lower educational stages. Neutral, comfort and acceptable temperatures are largely dependent on the educational stage and increase with it (e.g. 20.6, 21.7, 23.1, and 23.6 °C for primary school, middle school, high school, and university, respectively). These differences in thermal comfort expectations were reflected in the variable predictive capability of the Predicted Mean Vote (PMV) method (the greatest difference between predicted and actual thermal sensations in primary schools). Furthermore, the study demonstrates that students with the perception of control express better subjective judgments regarding thermal comfort and IAQ. Overall, this study provides evidence of the necessity for standards that can capture variations depending on the educational stage. Furthermore, it highlights the importance of guaranteeing perceived control to the students to improve indoor comfort and decrease the energy demand for heating.

Index terms: thermal comfort, indoor air quality, perceived control, school buildings.

I. INTRODUCTION

Students spend a considerable amount of time in schools, which implies that they can be exposed to unfavorable Indoor Environmental Quality (IEQ). Providing thermal comfort and Indoor Air Quality (IAQ) without compromising energy consumption is therefore fundamental.

Current thermal comfort standards, such as ISO (International Organization for Standardization) 7730 [1], EN (European Norm) 16798-1 [2], and ASHRAE (American Society of Heating, Refrigerating, and Air-Conditioning Engineers) Standard 55 [3], determine the design values for operative temperatures and comfort equations based on two main approaches: the heat balance [4] and the adaptive [5,6] ones. The first approach involves the Predicted Mean Vote (PMV) – Predicted Percentage of Dissatisfied (PPD) model, which is based on the heat exchange between the human body and the surrounding thermal environment and does not consider the hypothesis that people can adapt to their surroundings for achieving comfort (e.g. opening a window or changing clothing insulation). The second approach involves an adaptive model, which assumes that indoor comfort depends on the relationship between indoor operative temperature and outdoor temperature.

In these standards, different perceptions at diverse educational stages are not considered. However, students' thermal preferences cannot be generalised but should be investigated based on age. At different educational stages, students exhibit different metabolic rates, perform different activities, and have different adaptive capacities. Since the age of students is an important aspect to evaluate, researchers have analysed indoor comfort in school buildings based on the educational stage, where the peculiarities of primary, secondary, or university levels were evaluated. However, only a few studies investigated all the educational stages simultaneously and, generally, the different schools and universities were located in different areas, thus limiting the possibility of distinguishing between the effects of the educational stage and other aspects such as climate or cultural habits.

Furthermore, the combined effect of IAQ and thermal comfort is still being debated, and IAQ can be particularly critical in classrooms when ventilation is only provided by opening windows.

Another critical aspect is the lack of perceived control in school buildings. Perceived control is a form of psychological adaptation: occupants with more means of control think they have more chances to adapt to their surroundings and therefore are less likely to complain of discomfort than those with a lower level of perceived control [5]. Yet, too little is known about the impact of perceived control on indoor comfort in the context of

---

school buildings, as these kinds of studies were mainly conducted in residential buildings.

All these considerations show that addressing IAQ and thermal comfort issues in educational buildings is particularly challenging, and that is not fair to consider all students equally, regardless of their educational stage.

Thus, the aim of this study is to (1) develop a better understanding of students' perception of the thermal environment at different educational stages; (1.2) evaluate whether the predictive performance of the PMV-PPD model varies with the educational stage; (2) investigate any possible correlation between the perceived control over the parameters of the surrounding indoor environment and the students' thermal comfort, and their perception of IAQ. For the first time buildings from all educational stages (from primary to university level) were investigated under the same climate so that all differences in the perception of the indoor environment are more likely to be due to only the educational stage.

II. Methods

The survey included a field study involving 11 school buildings from different educational stages in Pisa province during the heating period (From October to December 2021). Field environmental measurements and questionnaire surveys were conducted simultaneously.

A. School buildings

In total, 11 schools and 24 classrooms were surveyed, which included: 5 classrooms in 3 primary schools (6–10 years), 8 classrooms in 2 middle schools (11–13 years), 2 classrooms in one high school (14-18 years), and 9 classrooms in 5 university buildings (18+ years).

The buildings are located within a 14 km distance from Pisa and fall all into the same climatic zone ('group Csa' in the Köppen–Geiger classification).

B. Environmental measurements

The air temperature (T_a), globe-thermometer temperature (T_g), relative humidity (RH), and air velocity (V_a) were measured using a microclimate data logger (DeltaOhm HD 32.3) equipped with the following probes: a globe-thermometer TP3275, a hot-wire anemometer AP3203 and a temperature and humidity probe HP3217R. A PCE-HT110 instrument was used to monitor the outdoor air temperature and relative humidity. The CO_2 concentration was measured with PCE-AQD 10 probes and used as an indicator of IAQ.

The probes were positioned 1.1 m from the ground to simulate the sitting position of the students, and at least 1.5 m from the external walls and doors. The instruments were shielded from direct solar radiation, cleaned and periodically calibrated.

C. Questionnaire

Students were instructed to fill out a questionnaire while objective measurements were performed. The questionnaire was composed of five sections, and the questions complied with the ISO 28802 and ASHRAE 55 standards [3,7].

In the first section, the students' information, such as age, gender, height, weight, and location occupied in the classroom, was enquired.

The second section was used to assess each student's clothing insulation based on ISO 9920 [8].

The third part was intended for evaluating the thermal environment and included the following questions:

- Thermal Sensation Vote (TSV): "With reference to the temperature, how are you feeling now?" – From [-3] "very cold" to [+3] "very hot";
- Thermal Preference Vote (TPV): "Please state how you would prefer to be now:" – From [-3] "much colder" to [+3] "much warmer";
- Thermal Acceptability Vote (TAV): "On a personal level, this environment is for me:" - From [1] "perfectly acceptable" to [5] "unacceptable".

The fourth part asked for the perceived control level:

- Perceived Control (PC): "How do you evaluate your control of comfort parameters at this moment? (e.g. opening and closing windows, thermostatic control, adjustment of blinds and other screens)" – From [−3] "no control" to [+3] "full control".

The fifth part evaluated the air quality:

- Indoor Air Quality Vote (IAQV): "How do you judge the air quality in the room at the moment?" – From [−3] "terrible" to [+3] "excellent".

D. Data processing

The indoor operative temperature (T_{op}) and mean radiant temperature (T_{rm}) were calculated according to the ISO 7726 standard [9]. Clothing insulation (I_{cl}) and PMV-PPD indices were calculated according to the ISO 7730 standard [1]. The students' metabolic rate (Met) was initially estimated to be 1.2 met, based on the ISO 8996 standard [10]. Subsequently, the value was corrected by considering the different body surfaces of each student. The metabolic rate provided by the international standard was multiplied by the ratio between the body surface of each student and the surface area of an average adult, which was estimated to be 1.8 m^2. The running mean outdoor temperature (T_{rm}) was calculated from the seven days before the measurements based on EN 16798-1 [2].

The values of the environmental parameters were combined with the subjective responses. The questionnaire sample was divided into two groups based on the perceived control vote. The students were divided into the ones who perceived to have control over the environmental conditions (PC>0) and others that did not (PC<0). The ones who voted PC=0 were excluded from the analysis, as they were considered neutral and therefore not aware of the possibility to control the conditions.

III. Data Presentation and Discussion

A. Evidence of adaptation at each educational stage

A negative correlation has been identified between the indoor operative temperature and the clothing insulation (Fig.1); as the indoor operative temperature increased, clothing insulation decreased for all the educational stages.

A clear difference has been demonstrated among the four groups of samples. When the indoor temperature

became hotter, the primary school students were less responsive in adjusting the insulation level of their clothes (slope of the regression curve = -0.0056 in Table I.).

Logistic regression analysis was used to analyse students' behaviour in the window operation. The probability that the windows are opened (p_c) as a function of the temperature index can be defined as follows [11]

$$p_c = \frac{\exp(c+d\cdot T)}{1+\exp(c+d\cdot T)}, \qquad (1)$$

where the temperature index T is T_{op} for indoor and T_{rm} for outdoor, c is the intercept, and d is the slope of the logit line.

Fig. 2 shows the proportion of windows opened and the probability of windows being opened (p_c) as a function of T_{op} and T_{rm}.
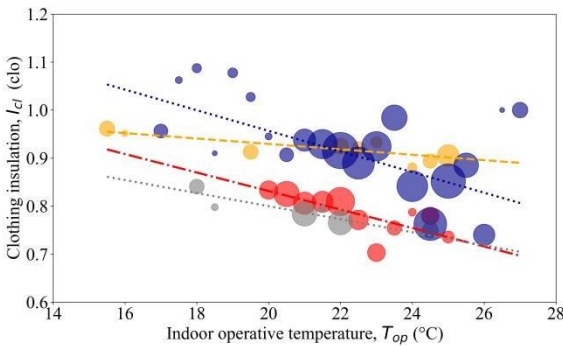
Figure 1. Relationship between clothing insulation and operative temperature for primary (in orange), middle (in red), high (in grey) schools, and university (in blue)

TABLE I.
REGRESSION ANALYSIS, R^2 AND P-VALUE FOR PRIMARY, MIDDLE, HIGH SCHOOLS AND UNIVERSITY

Educational stage	Regression	R^2	p-value
Primary school	$I_{cl} = -0.0056 \cdot T_{op} + 1.0421$	0.70	< 0.05
Middle school	$I_{cl} = -0.0193 \cdot T_{op} + 1.2165$	0.55	< 0.05
High school	$I_{cl} = -0.0136 \cdot T_{op} + 1.0718$	0.88	< 0.05
University	$I_{cl} = -0.0215 \cdot T_{op} + 1.3862$	0.34	< 0.05
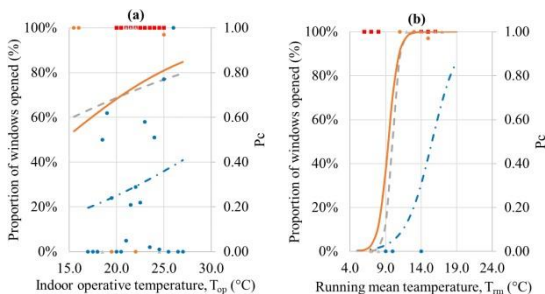
Figure 2. Proportion of windows opened as a function of T_{op} (a) and T_{rm} (b) for primary (in orange), middle (in red), high (in grey) schools, and university (in blue). Proportions of 0% and 100% imply that the windows were closed and opened, respectively. No relationship could be derived in the case of middle schools.

The slope of the regression curve turned out to be rather low for Primary Schools, since in that case the only occupants to open the windows are teachers and, therefore, it is difficult to talk about this type of adaptation for younger students.

The model was validated using a confusion matrix and parameters such as precision, recall, F1-score, and accuracy.

B. Calculation of neutral, preferred, and acceptable temperatures according to the educational stage

The neutral (T_n), preferred (T_p), and acceptable (T_{ac}) temperatures were calculated via the weighted regressions shown in Fig. 3. T_n and T_p were calculated by setting TSV and TPV to zero, respectively. T_{ac} was derived based on the TAV by considering occupants who voted 'perfectly acceptable' or 'slightly unacceptable'. In particular, T_{ac} was derived as the maximum of the quadratic regression, i.e. the point at which the percentage satisfied was the maximum.

An analysis of the neutral, preferred, and acceptable temperatures showed that they generally increased as a function of the educational stage (Table II.). Indeed, the results of this study indicate that younger students show higher tolerance than older students.
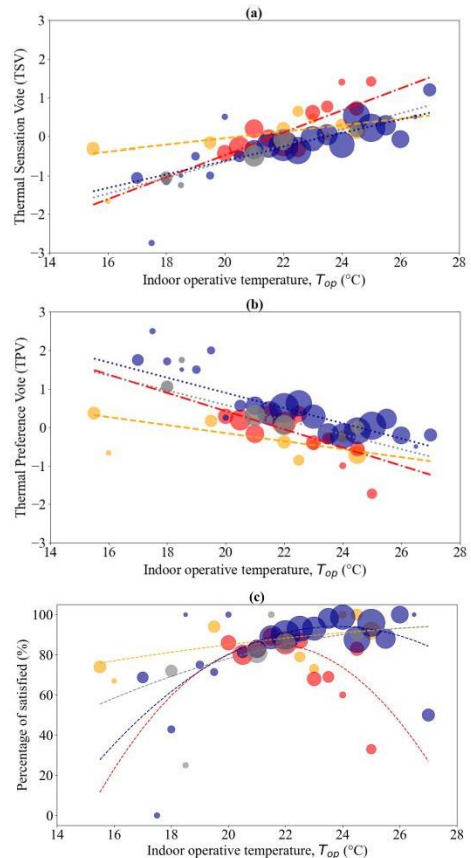

Figure 3. Relationship between indoor operative temperature and students' perception (TSV chart (a), TPV chart (b), Percentage of satisfied chart (c)) for primary (in orange), middle (in red), and high (in grey) schools, and university (in blue)

The relationship between neutral temperatures and student age was analysed. To calculate T_n, Griffiths' method was applied to the responses of individuals (1548 samples) as follows [12]

$$T_n = T_{op} + \frac{TSV}{G}, \qquad (2)$$

where G is the Griffiths' constant.

Once T_n was derived for each of the 1548 samples, the data were binned by the student's age. The discovered linear relationship between age and neutral temperature is ($R^2 = 0.60$, p-value < 0.05):

$$T_n = 0.1139 \cdot \text{Age} + 20.5146. \qquad (3)$$

A. Failure of the PMV-PPD model to predict thermal comfort at different educational stages

The variability in comfort temperatures at different ages might be caused by physiological (i.e. different metabolic activity) and psychological (i.e. different perception of the thermal environment) adaptations. These differences are not considered in the PMV–PPD model, which showed different accuracy degrees in the prediction of thermal comfort at different educational stages.

The ability of the PMV–PPD model to evaluate the thermal sensation of students was analysed. The relationship between thermal sensation and satisfaction was different at each educational stage and, in general, not perfectly symmetrical compared with the original PMV-PPD relationship (Fig. 4). For the primary schools, the minimum percentage of dissatisfaction exceeded 5% but included towards cold sensations, which implies that the children were more accepting of cold than warm sensations. The middle school students presented a very asymmetrical curve, with a higher percentage showing dissatisfaction with cold sensations. The high school students exhibited a quite symmetrical relationship between thermal sensation and satisfaction. By contrast, the curve for the university students was asymmetrical, with the minimum region shifting towards warm sensations, indicating that university students prefer warmer environments.

It is interesting to note that younger students are generally more satisfied, despite the temperature. The older students showed the lowest percentual of dissatisfaction.

Subsequently, the Mean Absolute Error (MAE) was calculated to assess the performance of the PMV model in predicting thermal sensation. This index was calculated as follows

$$MAE = \frac{\sum_{i=1}^{n} |p_i - a_i|}{n}, \qquad (4)$$

where p_i is the predicted value (PMV), a_i is the target value (TSV), and n is the number of samples.

The prediction error based on the MAE between the TSV and PMV decreased with the educational stage (1.02 for primary schools, 1.11 for middle schools, 0.90 for high school, and 0.72 for university), which implies that, in general, the prediction of thermal sensation for university students and high schools is more accurate. This may be because the PMV was developed for adults and, even if the correction developed for children for the metabolic rate is applied, the prediction error remains large.
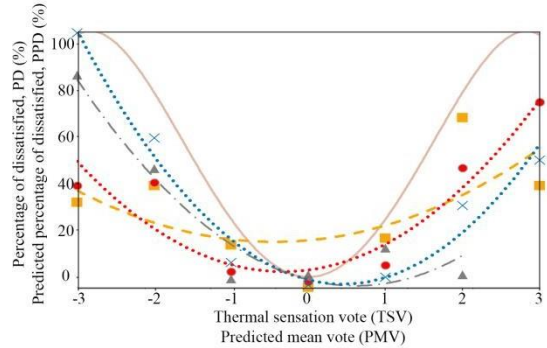

Figure 4. Relationship between occupants' thermal sensation votes (TSV) and percentage of dissatisfied (PD) for primary (dashed orange line), middle (dotted red line), and high schools (dash-dotted grey line), and university (dotted blue line), compared with the classic PMV–PPD curve (solid brown line)

TABLE II.
REGRESSION EQUATIONS, NEUTRAL, PREFERRED, AND ACCEPTABLE TEMPERATURES FOR PRIMARY, MIDDLE, HIGH SCHOOLS AND UNIVERSITY

Educational stage	Regression	R^2	p-value	T_n (°C)	T_p (°C)	T_{ac} (°C)
Primary school	TSV = 0.0835 · T_{op} - 1.7225	0.47	<0.05	20.6	18.5	21.9
	TPV = -0.1044 · T_{op} + 1.9364	0.61	<0.05			
	% = -0.0067 T_{op}^2 + 0.2822 T_{op} - 2.0494	0.69	<0.05			
Middle school	TSV = 0.2850 · T_{op} - 6.1742	0.64	<0.05	21.7	21.8	21.2
	TPV = -0.2368 · T_{op} + 5.1575	0.52	<0.05			
	% = -0.0215 T_{op}^2 + 0.9266 T_{op} - 9.0754	0.74	<0.05			
High school	TSV = 0.2059 · T_{op} - 4.7649	0.91	<0.05	23.1	23.0	22.2
	TPV = -0.1913 · T_{op} + 4.4049	0.73	<0.05			
	% = -0.0226 T_{op}^2 + 1.019 T_{op} - 10.516	0.88	<0.05			
University	TSV = 0.1751 · T_{op} - 4.1234	0.63	<0.05	23.6	24.1	25.0
	TPV = -0.2454 · T_{op} + 6.0165	0.79	<0.05			
	% = -0.0076 T_{op}^2 + 0.3659 T_{op} - 3.402	0.60	<0.05			

B. Impact of perceived control on thermal comfort

The impact of perceived control on thermal comfort and IAQ was studied including students of all educational stages without distinction. This was done not to fragment the sample and because the purpose of this work was to first understand whether the perceived control had any influence on the students' comfort, regardless of the educational stage. Indeed, this study was the first to investigate the influence of perceived control over indoor comfort in school buildings.

The relationship between thermal sensation and the operative temperature was calculated for PMV and TSV with and without perceived control. Weighted linear regressions between the two variables were obtained and the neutral temperatures were calculated by imposing the conditions TSV=0 and PMV=0. The regression equation, R^2, p-value, and $T_{neutral}$ calculated from the predicted and observed thermal sensation with and without perceived control are reported in Table III.

Fig. 5 shows the PMV and the TSV of subjects with and without perceived control. The TSV of subjects with and without perceived control suggests that subjects with perceived control were on average in a situation of thermal neutrality. On the other hand, at the same indoor operative temperatures, subjects without perceived control were more sensitive to temperature changes.

Furthermore, regarding neutral temperature, it was 0.6 °C lower in case the students perceived to have personal control. This difference in neutral temperature is lower than others found in studies in different building type which showed differences of 1.9°C [13] or even 2.6°C [14] This can be related to a higher possibility to control the environmental conditions in residential buildings rather than in schools. However, this difference is still relevant in terms of providing comfort and reducing energy consumption as a lower neutral temperature means a lower set-point temperature and less energy demand for heating.

The impact of perceived control on the thermal sensation vote is inversely proportional to the indoor temperature. As the indoor operative temperature increases in winter, the positive effect of the perceived control decreases. This trend is in line with previous studies conducted in residential buildings during the winter season [13,15].

Furthermore, to analyse the impact of perceived control on satisfaction, weighted polynomial regressions between operative temperature and the rate of satisfaction were calculated thanks to the TAV. Subjects with perceived control showed greater acceptance of the thermal environment, especially for more severe thermal conditions (Fig. 6). Even at neutral temperatures, there was greater acceptability of the environment by subjects with perceived control. Indeed, the percentage of satisfied occupants with perceived control never decreased below 70%. This is in line with previous studies conducted in climate chambers which showed that perceived control can alleviate subjects' thermal discomfort [15,16].
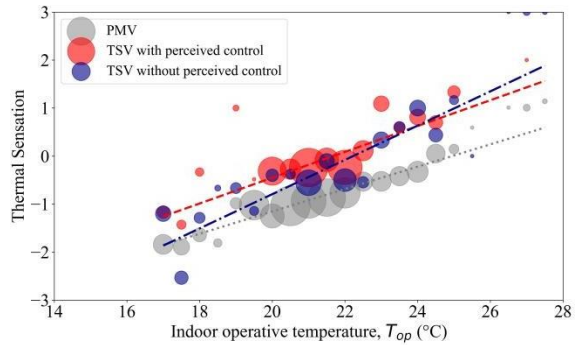

Figure 5. Relationship between indoor operative temperature and students' thermal sensation with and without perceived control

TABLE III.
REGRESSION EQUATIONS, R^2, P-VALUE, AND NEUTRAL TEMPERATURE CALCULATED FROM THE PREDICTED AND OBSERVED THERMAL SENSATION WITH AND WITHOUT PERCEIVED CONTROL

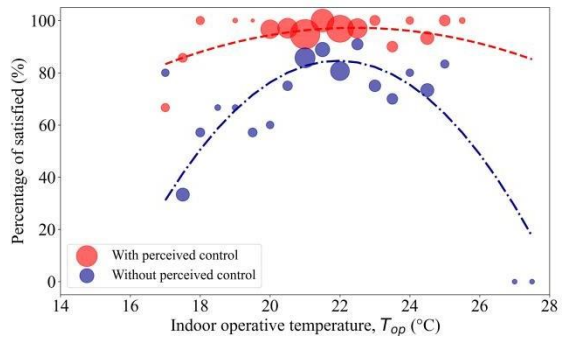|	Regression equation	R^2	p-value	T_n (°C)
PMV	$PMV = 0.26 \cdot T_{op} - 6.50$	0.95	<0.05	24.6
TSV with perceived control	$TSV = 0.25 \cdot T_{op} - 5.58$	0.82	<0.05	21.7
TSV without perceived control	$TSV = 0.32 \cdot T_{op} - 7.13$	0.88	<0.05	22.3

Figure 6. Relationship between indoor operative temperature and percentage of satisfied students, with and without perceived control

C. Impact of perceived control on indoor air quality perception

The relationship between the perception of IAQ and the operative temperature was calculated for the IAQV with and without perceived control (Fig.7). The weighted regression equation, R^2, and p-value calculated from the IAQV with and without perceived control is reported in Table IV. Subjects with perceived control expressed better IAQV.

The relationship between the perception of air quality and CO_2 concentration was also investigated. The results showed that there is not a strong correlation between the two parameters ($R^2 < 0.1$ and p-value > 0.9 for both subjects with and without perceived control).
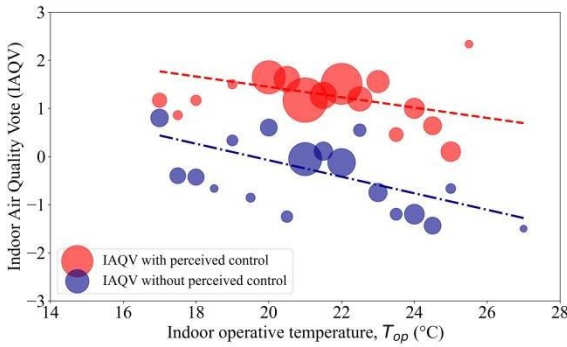
Figure 7. Relationship between indoor operative temperature and students' indoor air quality vote, with and without perceived control

TABLE IV.
REGRESSION EQUATIONS, R^2 AND P-VALUE CALCULATED FROM THE INDOOR AIR QUALITY VOTES WITH AND WITHOUT PERCEIVED CONTROL

	Regression equation	R^2	p-value
With perceived control	IAQV = -0.159 · T_{op} + 4.336	0.45	<0.05
Without perceived control	IAQV = -0.119 · T_{op} + 2.488	0.29	<0.05

IV. CONCLUSIONS

In this study, the effect of the educational stage on the perception of the thermal environment and IAQ is investigated. This is the first study that involves all educational stages (from primary schools to universities) under the same period and geographical area. This aspect is particularly relevant as it finally allows the research to understand the different perceptions more clearly by reducing other confounding parameters. Furthermore, this is the first work investigating the impact of perceived control on indoor comfort in school buildings. The main conclusions of this study are as follows:

- The ability to adapt to the environment increased with the educational stage.
- Younger students are more tolerant and satisfied than older ones, despite having less adaptive capacities.
- Neutral, preferred, and acceptable temperatures increase with students' age (e.g. the neutral temperature increases by 1 °C on average at every educational stage).
- Current comfort standards, which are based on the PMV–PPD method, are not accurate in predicting the thermal sensations of students, and correcting the metabolic rate is insufficient to achieve a better agreement between the actual and predicted thermal sensation. Adjustment coefficients should be formulated based on students' age.
- In this sense, the derived relationship between neutral temperatures and students' age seems very promising.
- In winter, the neutral operative temperatures of students with and without perceived control are 21.7 °C and 22.3 °C, respectively. Students should be aware of the possibility to control the environment, which is conducive to reducing the comfort temperatures, setting lower setpoint temperatures, and lowering the energy demand for heating.

- Subjects with perceived control are also more satisfied with IAQ than subjects without perceived control.

REFERENCES

[1] ISO 7730, "Ergonomics of the thermal environment — Analytical determination and interpretation of thermal comfort using calculation of the PMV and PPD indices and local thermal comfort criteria", 2005.

[2] EN 16798-1, "Energy performance of buildings - Ventilation for buildings - Part 1: Indoor environmental input parameters for design and assessment of energy performance of buildings addressing indoor air quality, thermal environment, lighting and acoustics", 2019.

[3] ASHRAE, "Standard 55 - Thermal environmental conditions for human occupancy", 2020.

[4] P. O. Fanger, *Thermal comfort. Analysis and applications in environmental engineering*. Copenhagen: Danish Technical Press, 1970.

[5] J. F. Nicol and M. A. Humphreys, "Adaptive thermal comfort and sustainable thermal standards for buildings", *Energy Build*, vol. 34, no. 6, pp. 563–572, Jul. 2002, doi: 10.1016/S0378-7788(02)00006-3.

[6] R. de Dear and G. S. Brager, "Developing an adaptive model of thermal comfort and preferences", *ASHRAE Transactions*, pp. 145–167, 1998.

[7] ISO 28802, "Ergonomics of the physical environment - Assessment of environments by means of an environment survey involving physical measurements of the environment and subjective responses of people", 2012.

[8] ISO 9920, "Ergonomics of the thermal environment. Estimation of thermal insulation and water vapour resistance of a clothing ensemble", 2009.

[9] ISO 7726, "Ergonomics of the thermal environment - Instrument for measuring physical quantities", 2001.

[10] ISO 8996, "Ergonomics of the thermal environment - Determination of metabolic rate", 2005.

[11] F. Nicol, M. Humphreys, and S. Roaf, *Adaptive Thermal Comfort: Principles and Practice*. Routledge, 2012. doi: 10.4324/9780203123010.

[12] I. Griffiths, *Thermal Comfort Studies in Buildings with Passive Solar Features. Field Studies.* 1990.

[13] C. Xu and S. Li, "Influence of perceived control on thermal comfort in winter, A case study in hot summer and cold winter zone in China", *Journal of Building Engineering*, vol. 40, p. 102389, Aug. 2021, doi: 10.1016/J.JOBE.2021.102389.

[14] M. Luo *et al.*, "Can personal control influence human thermal comfort? A field study in residential buildings in China in winter", *Energy Build*, vol. 72, pp. 411–418, Apr. 2014, doi: 10.1016/j.enbuild.2013.12.057.

[15] M. Luo, B. Cao, W. Ji, Q. Ouyang, B. Lin, and Y. Zhu, "The underlying linkage between personal control and thermal comfort: Psychological or physical effects?", *Energy Build*, vol. 111, pp. 56–63, Jan. 2016, doi: 10.1016/j.enbuild.2015.11.004.

[16] X. Zhou, Q. Ouyang, Y. Zhu, C. Feng, and X. Zhang, "Experimental study of the influence of anticipated control on human thermal sensation and thermal comfort", *Indoor Air*, vol. 24, no. 2, pp. 171–177, Apr. 2014, doi: 10.1111/ina.12067.

[17] G. Torriani, G. Lamberti, F. Fantozzi, and F. Babich, "Exploring the impact of perceived control on thermal comfort and indoor air quality perception in schools", *Journal of Building Engineering*, p. 105419, Oct. 2022, doi: 10.1016/J.JOBE.2022.105419.

[18] G. Torriani, G. Lamberti, G. Salvadori, F. Fantozzi, and F. Babich, "Thermal Comfort and Adaptive Capacities: Differences Among Students at Various School Stages", unpublished.

The Impact of Usage of Heating and Cooling Systems' Circulation Pumps in the Smart Grid on Building's Electricity and Heat Consumption Profiles

Sofia Vasman [a], Martin Thalfeldt [a], Eduard Petlenkov [b]

[a] Nearly Zero Energy Buildings Research Group: Department of Civil Engineering and Architecture, Tallinn University of Technology, Estonia
[b] Centre for Intelligent Systems: Department of Computer Systems, Tallinn University of Technology, Estonia
Corresponding emails: sofia.vasman@taltech.ee, martin.thalfeldt@taltech.ee, eduard.petlenkov@taltech.ee
This work has been defended at the home university in May 2022.

Abstract — **As the EU shifts towards more alternative energy sources, maintaining the energy generation and consumption balance becomes increasingly important. The Smart Grid allows two-way communication between the generation and consumption sides of the energy system. Such communication can help initiate energy consumption reduction at times of potential grid overload sending demand signals. Additionally, financial incentives encourage the grid's secondary side to reduce consumption. To respond to a demand signal, the consumption side must offer a possible amount of shredded energy or a -regulation amount. This study evaluates the potential of reducing electrical and heating energy consumption in Tallinn University of Technology campus through indoor climate control systems in response to Smart Grid demand. The evaluation included gathering selected circulation pump characteristics, calculating the maximum possible electrical energy reduction under different response strategies, modeling heating energy consumption to avoid causing overcompensation in heating energy consumption after circulation pumps OFF periods and verifying that electrical energy consumption reduction does not harm the indoor climate. The study found that there are 48 circulation pumps on university campus with the total power of 43.6 kW at dimensioning flow rate, equating to 7.7 W/m² with specific power per each buildings' service area. Additionally, it is possible to reduce electrical energy consumption without causing overcompensation in heating energy consumption after circulation pumps OFF periods, at least in buildings similar to the test building. In addition, the study revealed a financial benefit from bidding prices and reduced electricity costs.**

Index Terms — **Building management systems, circulation pumps, demand response, energy consumption, smart grid.**

Introduction

The EU's green revolution has rapidly changed its power system by integrating alternative energy sources into the grid [1]. Simultaneously, the power grid has been expanding, increasing the number of participants. As a result, such mutual grid changes may cause grid overload, instability, and operational challenges. One way to ensure grid stability is to maintain the balance between energy generation and consumption. Modern info- and communication technologies allowed to create a whole integrated network to support the balance [2], [3]. The Smart Grid enables multi-way communication between operational levels and encourages the involvement of all the network participants.

The Smart Grid concept can help with reducing energy consumption using different strategies (Fig. 1). Demand signals from the primary side trigger incentive-based Demand Response (DR) strategy, and the participants are required to reduce power consumption, and rewarded for decreasing their energy consumption. The price-based DR strategy program provides participants with power prices in advance, reflecting the network state for a certain following period. This allows participants to make decisions about when to reduce energy consumption. It is important to note that the grid load and power costs are correlated, thus the power price becomes a means of consumption regulation [4], [5].

The secondary side of the energy grid consists of various consumer types, including buildings. Buildings use a significant portion of the overall grid-generated energy for a variety of operational needs [6]. These needs differ depending on building type and time periods. A building's electrical and heating energy consumption peaks and profiles mirror its operation and become a foundation for energy consumption management and optimization. Building energy consumption optimization and peak shaving are possible due to flexibility within buildings. This flexibility comes from the ability to shift energy consumption to different time periods for various reasons,
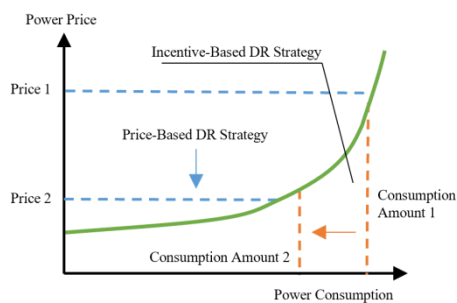

Fig. 1 Demand Response strategies

such as local energy generation, building envelope heat capacity, energy storage systems, and changes in Building Management Systems' (BMS) schedules [7].

One of the main BMS functions is to maintain the required indoor climate quality level. Indoor climate system solutions are based on buildings' architecture and building physics properties and are designed to keep the required indoor environment even under the most extreme outdoor conditions. In generally cooler regions, building envelopes are thermally insulated, creating a delayed effect of outdoor conditions on the indoor environment. Based on this, indoor climate thermal flexibility potential comes from utilizing energy stored in building envelopes due to materials' thermal capacity.

Additionally, since indoor condition requirements are set in the form of different intervals for various parameters and indoor climate quality levels, there is also flexibility potential in using these intervals, for example stopping technical systems' operation as long as the indoor conditions allow to do so. A similar approach has already been implemented in indoor climate automation design, where the concept of a dead zone is used. The dead zone refers to a deviation in temperature or any other parameter relative to the setpoint without any actions from the controllers [8].

To participate in flexibility services using technical system algorithms previous years' data from electrical systems, building performance and external environment are utilized. The aim of this works is to evaluate the reduction of energy consumption and operational costs for circulation pumps within the context of flexibility service using data required for flexibility service algorithms development, as well as evaluate the impact of changes in circulation pump operation on indoor conditions.

METHODS

The research integrates descriptive and experimental methods to examine the current state of heating and cooling pumps' control potential and develop flexibility service control strategies or DR strategies variations, using Tallinn University of Technology (TalTech) campus as a case study for experimentation.

A. Building and systems

Building construction projects and heating and cooling systems' information provided by the TalTech property department and campus BMS were analyzed to compile the overview of the campus' heating and cooling systems' circulation pumps.

To determine electrical power, it is necessary to know the pumps' operating points. In terms of pump flow rate, either the system power and operational temperatures or the system flow rate were known. In case of unknown system pressure, it was decided to find a correlation between system pressure and the building service area (Pa/m²). As the system expands, the pressure drop in the main components remains, yet the friction pressure drop changes. A function (1) was drawn through the known specific pressure points (Fig. 2) and the constants of the functions were found using the least squares method implemented as a Python function [10]. The pumps' power at the dimensioning, as well as 30% flow rate parameters, were based on each pumps' technical sheet from the

manufacturer selection program after identifying the operational points.

$$f(x) = a \cdot e^{-b \cdot x} \qquad (1)$$
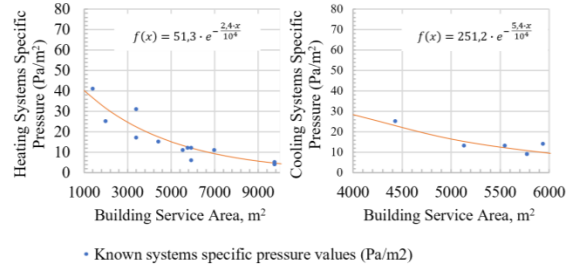
where x building service area (m²)

Fig. 2 Relationship between system specific pressure and building service area [Pa/m²] for estimating missing pressure values

To calculate the power consumption of the pumps over a certain period, it is necessary to determine the pumps' operational limits, which can be accessed through the BMS. The operation of circulation pumps is dependent on the set-points of the ambient air temperature. When the air temperature falls below a set threshold, heating circulation pumps are activated, yet cooling circulation pumps are activated when the ambient air temperature is greater than the set-point value. These ambient air temperature set-points were gathered from the campus BMS.

B. Response strategies

Two regulation principles maintain the balance between generation and consumption in the grid: up-regulation and down-regulation. Down-regulation occurs when the system operator (SO) sells additional electrical energy due to low consumption, higher-than-estimated production, or endangered power system supply security. Up-regulation, on the other hand, occurs when the SO purchases an additional amount of energy due to higher consumption, lower-than-estimated production, unexpected changes in production capacity, or, similarly, endangered power system supply security [12].

This study examines several half-hour long up-regulation bids throughout each day during year 2021. DR strategy variations are based on pump operation permission, which depends on ambient air temperature [13], demand response activation (Estonia Upward [MWh] [14]), balancing energy prices (Estonia Upward [EUR/MWh] [15]), and electricity price (NordPool data archives, hour average price [EUR/MWh] [16]).

In summary, four DR strategy variations were tested: two advised by a consultant with fixed pauses between reactions (Fig. 3), and two price-based strategies (Fig. 4). The DR consumption reduction potential for up-regulation or balancing was calculated based on the pumps' power at dimensioning and 30% flow rate, (as the BMS at the time of the study lacked the option to log pump power consumption, representing changes at a 30% flow rate consumption demonstrates the minimum potential of the systems), with all pumps receiving operation prohibition during each DR activation. Calculations for both pump power consumption variations were performed using Python functions and libraries, such as Pandas and Numpy.
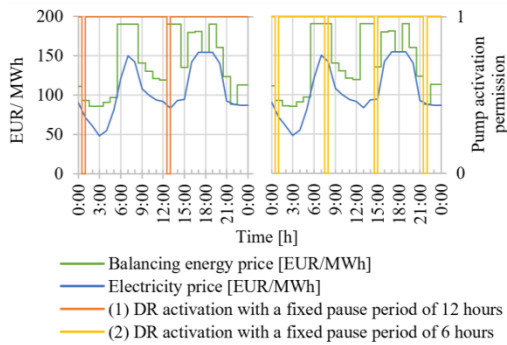
Fig. 3 DR strategies based on the consultant's advice. (1) DR strategy activation is set for 12-hour interval and (2) DR - 6-hour interval
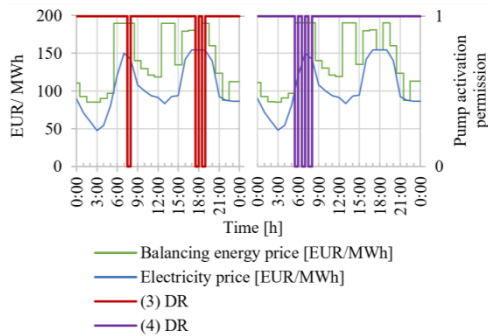

Fig. 4 Price-based DR strategy variations. (3) DR activation is based on 3 the highest electricity prices and (4) DR activation is based on 3 the highest balancing prices of the day

C. Test building

TalTech "Ehituse Mäemaja" or Constriction Building (CON) is a nearly zero energy university laboratory building, with the area of 3500m², that was renovated in the beginning of 2021. As a relatively new building, CON is a suitable testing ground. Three tests were conducted between March and April 2022. The first test, on 09.03.2022 (10:45AM – 11:38AM), aimed to evaluate the indoor air temperature recovery rate, with ambient air temperature changing from -3.2 ºC to -2.6 ºC and overcast sky. The second and third tests, on 14.04.2022 (9:15AM – 10:15AM and 3:00PM – 4:10PM), evaluated heating power consumption dynamics when circulation pumps were stopped multiple times a day, simulating participation in flexibility service, with ambient air temperature being of +4.1 ºC and +4,5 ºC, respectively and the sky transitioning from overcast to clear conditions.

During the tests, only the radiator heating system was evaluated, and only two parameters were logged: the indoor air temperature of radiator-heated rooms with a 10-minute interval and the heating energy consumption of sub-system's heating meter with a 3-minute interval. Cooling systems' dynamics were not evaluated due to outdoor conditions.

D. Technical systems modeling

Building systems' energy consumption reflects their usage and dynamics and can be represented graphically through consumption profiles. A mathematical model can describe building energy consumption profiles and can be used for consumption estimation.

Consumption modeling was used to quantify the overcompensation in heating energy, which might occur upon pumps' activation after the test. While turning off circulation pumps has financial potential, overcompensation in heating energy consumption upon restarting may negatively impact these financial benefits.

RESULTS

E. Flexibility potential of the TalTech circulation pumps

In total, 18 campus buildings were reviewed, and based on their circulation pumps information, the overview table was created (TABLE I). There are 48 circulation pumps on TalTech campus: 20 radiator heating systems pumps, 4 floor heating system pumps, 16 room cooling system pumps, and 8 cooling coil system pumps for air handling units. The total power of the circulation pumps at dimensioning flow rate is 43.6 kW, equating to 7.7 W/m² with specific power per each buildings' service area and 21.9 kW, 3.94 W/m² respectively at a 30% flow rate. Although the number of cooling circulation pumps is equal to that of heating systems' pumps, their power consumption makes up a significant part of the total consumption (Fig. 5).

Having the ambient air temperature set-points gathered, it was possible to determine circulation pumps active periods. A logic function using the local climate file with 1-hour interval data was developed to calculate the total active period for each pump during the year 2021. By multiplying the hours by pump power, the total power consumption for the campus' circulation pumps was obtained. To calculate the power costs for the same period, the timestamps of active circulation pumps were saved, and electricity prices for the same timestamps were retrieved, summarized, and multiplied by the pumps' power [W/m²]. The total energy consumption of the pumps at the dimensioning flow rate for the year 2021 was 29.6 kWh/m²a with an operational cost of 253 €cent/m²a and 29.6 kWh/m2a and 173 €cent/m2a at 30% flow rate pump power (Fig. 6).

TABLE I

An extract from TalTech Campus circulation pumps overview table

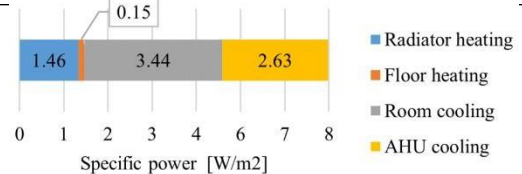| Building	Type	Pump	System Power	System Flow Rate	System	Preset Motor Power at Dim.Flow
			Q (kW)	G (L/s)	Δp (kPa)	P_Gf (W)
CON	Floor	MAGNA3 32-100	70	1.11	105	246

Fig. 5 Specific pump power at dimensioning operation point, totaling to 7.7 W/m2
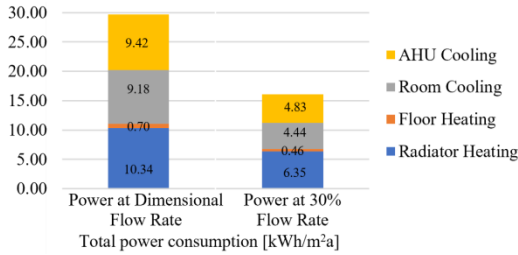
Fig. 6 Pump power consumption at various settings in the year 2021

To estimate the pumps power consumption reduction and the financial benefits for the year 2021, the following sets of rules were implemented in a Python code. This approach simplified the process of evaluating multiple conditional statements simultaneously.

(1) DR strategy variation, 12-hour interval applied to each pump separately:

1. Check if the ambient air set-point rule is true for the pump operation
2. If true, check if there is a DR activation signal during that hour
3. If there is a DR activation signal, add +1 to total operational hours variable, save the timestamp and check the next timestamp after 12-hour window following steps 1-3
4. If there is no activation signal check the next timestamp after 12-hour window following steps 1-3
5. Continue these steps throughout the entire year data
6. Determine the electricity and balancing energy prices at the saved timestamp. Add the prices to the pricing variable
7. Calculate power reduction using pump power at different setting and half of total operational hours variable to describe consumption reduction in case of 30-minute activation
8. Calculate financial benefit using the pricing variable and dividing it by 2 and converting to the desired unit

The same steps are applicable to (2) DR strategy variation, only the interval window has to be set to 6 hours.

(3) DR strategy variation, 3 highest electricity prices. Applied to each pump separately

1. Determine the 3 highest electricity prices during the day, save the timestamps
2. Check if the ambient air set-point rule is true for the pump operation at the saved timesteps
3. If true and the pumps can stop operating upon receiving the DR activation signal, add the total number of signals to operational hours variable
4. Determine the balancing energy price at the saved timestamps. Add the electricity and balancing energy prices to the price variable
5. Move onto the next day and continue these steps throughout the entire year data
6. Calculate power reduction using pump power at different setting and half of total operational

hours variable to describe consumption reduction in case of 30-minute activation
7. Calculate financial benefit using the pricing variable and dividing it by 2 and converting to the desired unit

The same steps are applicable to (4) DR strategy version, in which the activation signal is based on the highest balancing energy price.

Fig. 7 and Fig. 8 represent the impact of the tested DR strategies' variations. The strategies (3) DR and (4) DR had a significant impact both on consumption as well as financial benefits, by reducing pumps' operational costs. The consumption reduction in both power setting cases was around 6% (6.34% for dimensioning flow setting and 6.28% for 30% flow setting) and the financial benefit was around 19% (19.82% for dimensioning flow setting and 19.71% for 30% flow setting). Such impact suggests that price-based DR strategies are a good choice of flexibility service response strategy.
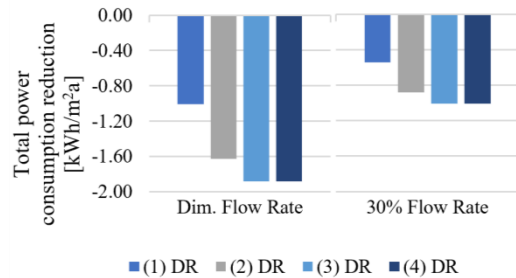

Fig. 7 Pump power consumption reduction using suggested DR strategy variations, baseline 29.64 and 16.08 kWh/m²a respectively
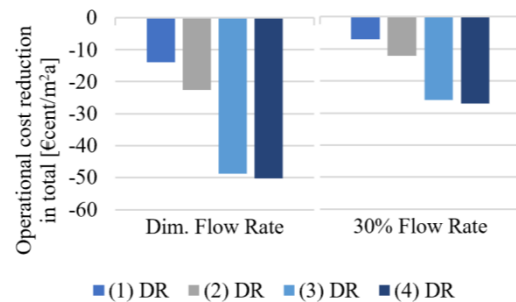

Fig. 8 Pump operational costs reduction, including saving due to absent electric energy consumption during DR activations and received incentives, baseline 253 and 173 €cent/m²a respectively

F. Test building and systems modeling

FigureFig. 9 was created using data logged during the tests, illustrating the indoor air temperature changes when the heating system was turned off. The figures show no decrease in air temperature values in response to the shut-down heating system during all the tests. Moreover, the data from the second and third tests indicate that there was no delayed indoor air temperature reduction even after two periods of stopped heating systems. Additionally, the values remained within the required limits according to winter period norms and BMS set-points for each room.
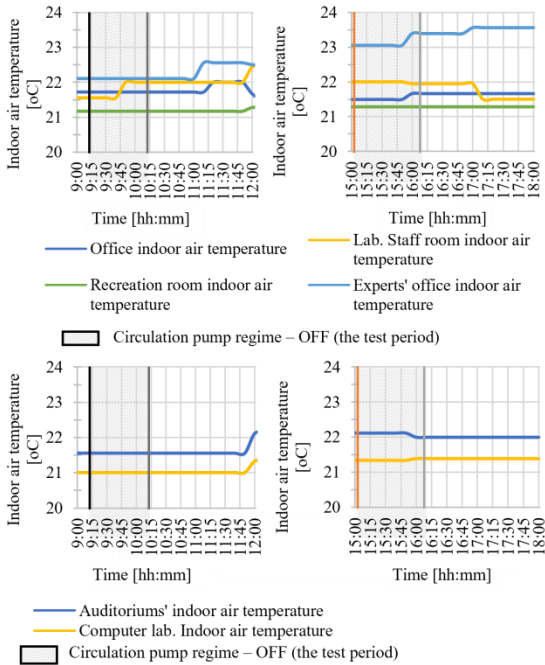
Fig. 9 CON building indoor air temperature [°C] in various rooms on 14.04.2022 during the second and the third tests

The next step aimed to evaluate heating energy consumption. Five working days from two weeks, including the test days, were selected to represent CON building energy consumption profiles (Fig. 10, Fig. 11) and to model the consumption based on the data from the sub-systems' heating meter Q1.1. To highlight the test days' and following days' similarities, the values were normalized to a baseline consumption (Fig. 12, Fig. 13).
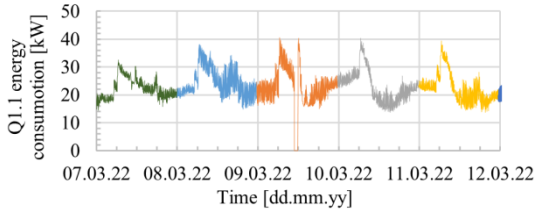
Fig. 10 Heating energy consumption for the test building during a workweek including the first test day (09.03.2022)
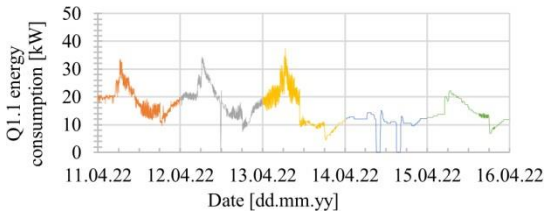
Fig. 11 Heating energy consumption for the test building during another workweek including the second and third test day (14.04.2022)
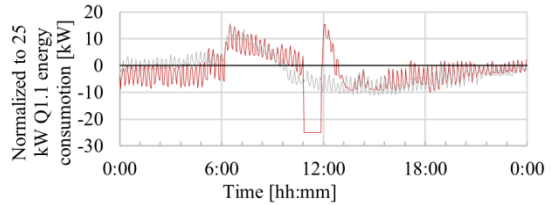
Fig. 12 Test building's aggregated profile of days with similar consumption including the first test day (workweek Fig. 10)
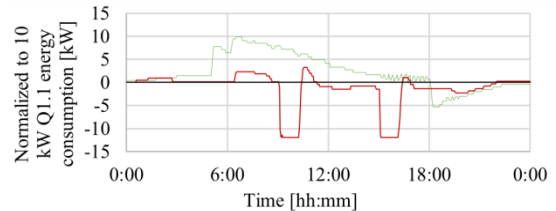

Fig. 13 Test building's aggregated profile of days with similar consumption including the second and third test day (workweek Fig. 11)

Using test data and models can help determine whether it is reasonable to include a certain sub-system in DR program from a heating perspective. After conducting the test, it is necessary to compare the reduced or saved energy amount (Q_s) with the energy amount needed to recover indoor conditions (Q_r). Comparing energy amounts from a certain period of time, which includes the test time as well, is more convenient since it is difficult to determine when energy consumption returns to normal. To avoid overcompensation in heating energy amount, the following condition must be true: $Q_s > Q_r$.

Q_s is calculated by integrating the consumption mathematical model. Python functions were used to find the constants for both model equations. Equation (2) describes a cubic polynomial that was chosen to model the first test day consumption (Fig. 14).
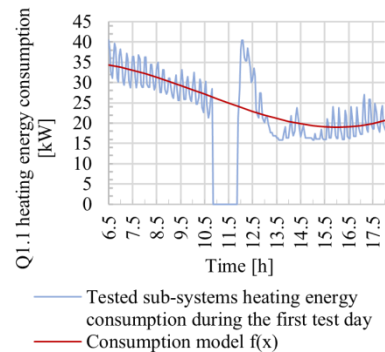

Fig. 14 The first test day heating energy consumption model

$$f(x) = 0{,}024 \cdot x^3 - 0{,}77 \cdot x^2 + 5{,}992 \cdot x + 21{,}687 \ (2)$$

$$Q_s = \int_{10.75}^{17.5} f(x)\, dx = 143.6\ kWh$$

$$Q_r = 107.6\ kWh$$

FigureFig. 15 shows the second and third tests' day with a linear consumption model (3) due to the relatively steady heating energy consumption in the sub-system.
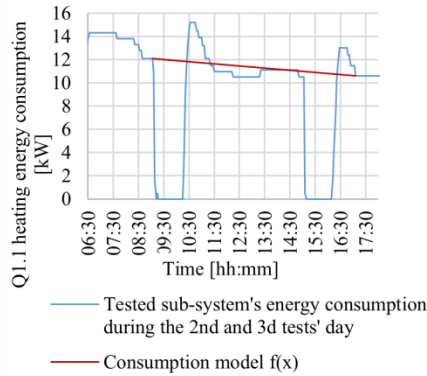
Fig. 15 The 2nd and 3rd tests' day heating energy consumption model

$$f(x) = -0.17 \cdot x + 13,6 \qquad (3)$$

$$Q_s = \int_{9.25}^{17.5} f(x)\, dx = 93.4\, kWh$$

$$Q_r = 23.6\, kWh$$

The condition $Q_s > Q_r$ is true in both cases, indicating that no overcompensation in heating power consumption occurred on the test days.

DISCUSSION

The results of this study demonstrate the potential for reducing electrical and heating energy consumption in the Tallinn University of Technology campus through HVAC systems' circulation pumps in response to the Smart Grid demand. The analyzed campus buildings have 48 circulation pumps in total, providing an opportunity for energy consumption reduction. This study's findings show that a reduction in electrical energy consumption can be achieved without causing overcompensation in heating energy consumption following circulation pump OFF periods, at least for the buildings similar to the test building. Additionally, the price-based demand response strategies are potentially effective in achieving energy consumption reduction and financial benefits. This suggests that these strategies could be implemented in similar settings to optimize energy consumption and reduce cost.

However, one limitation of the present study is the absence of the cooling consumption analysis due to weather conditions during the research period and the tests being conducted in a well-insulated building. Future research should fill this gap by evaluating the potential for energy consumption reduction in cooling systems, as these systems also contribute significantly to overall energy use in buildings. This could enhance the understanding of the potential for energy consumption reduction in the context of the Smart Grid and provide a new set of possibilities for energy optimization in university campus as well as in a similar setting.
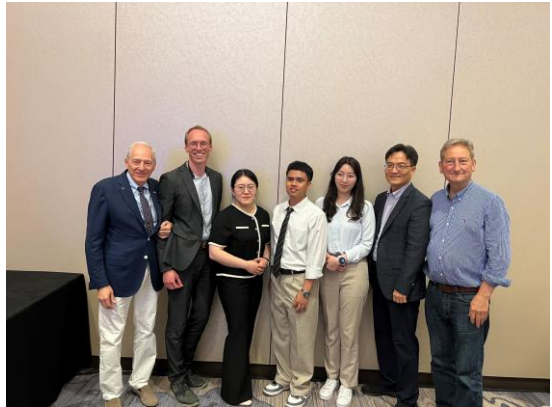
CONCLUSION

This research demonstrates the potential of utilizing indoor climate systems' circulation pumps to provide flexibility in response to Smart Grid demand, while also reducing electrical and heating energy consumption. The tests conducted in one of the Tallinn University of Technology buildings have revealed potential for consumption reduction without compromising the indoor climate quality. Additionally, the implementation of price-based DR strategies has proven to be an effective way to achieve energy consumption reduction and financial savings. The findings of this study could be applied to other campuses and building with similar characteristics located in the similar climatic zone, contributing to the overall sustainability and efficiency of the energy systems. Future research should also evaluate the potential for energy consumption reduction in cooling systems using only circulation pumps' control to provide a new set of opportunities for energy optimization.

REFERENCES

[1] "Statistics | Eurostat." https://ec.europa.eu/eurostat/databrowser/view/t2020_rd330/default/line?lang=en (accessed May 11, 2022).

2 L. Morales and J. Hanly, "European power markets–A journey towards efficiency," *Energy Policy*, vol. 116, pp. 78–85, May 2018, doi: 10.1016/j.enpol.2018.01.061.

3 "Tarkvõrgu arendamine | Elering." https://elering.ee/tarkvorgu-arendamine (accessed May 09, 2022).

4 P. Palensky and D. Dietrich, "Demand side management: Demand response, intelligent energy systems, and smart loads," *IEEE Trans Industr Inform*, vol. 7, no. 3, pp. 381–388, Aug. 2011, doi: 10.1109/TII.2011.2158841.

5 Department of Energy, "Benefits of Demand Response in Electricity Markets and Recommendations for Achieving Them," 2006.

6 "Electricity and heat statistics - Statistics Explained." https://ec.europa.eu/eurostat/statistics-explained/index.php?title=Electricity_and_heat_statistics (accessed May 11, 2022).

7 F. Mofidi and H. Akbari, "Intelligent buildings: An overview," *Energy Build*, vol. 223, p. 110192, Sep. 2020, doi: 10.1016/J.ENBUILD.2020.110192.

8 HVAC&R Nation, "SPACE TEMPERATURE SET POINT AND CONTROL BANDS," 2015, p. 1. [Online]. Available: www.hvacrnation.com.au

9 Teet-Andrus Kõiv and Aivar Rant, "Hoonete küte," 2013. https://www.digar.ee/arhiiv/nlib-digar:388794

[10] "Least Square Regression for Nonlinear Functions — Python Numerical Methods." https://pythonnumericalmethods.berkeley.edu/notebooks/chapter16.05-Least-Square-Regression-for-Nonlinear-Functions.html (accessed May 07, 2022).

11 R. Robinson, "Pumping Control Methods and Their Impact on System Efficiency."

12 ENTSO-E, "Rules on Balancing," Jan. 01, 2022. https://transparency.entsoe.eu/balancing-domain/r2/rulesOnBalancing/show?name=&defaultValue=true&viewType=TABLE&areaType=MBA&atch=false&dateTime.dateTime=01.01.2022+00:00|UTC|YEAR&dateTime.endDateTime=01.01.2022+00:00|UTC|YEAR&biddingZone.values=CTY|10Y1001A1001A39I!MBA|10Y1001A1001A39I (accessed May 16, 2022).

[13] "Ajaloolised ilmaandmed |Keskkonnaagentuur." https://www.ilmateenistus.ee/kliima/ajaloolised-ilmaandmed/

14 "Normal activations - mFRR - BTD." https://baltic.transparency-dashboard.eu/node/36

15 "Balancing energy prices - BTD." https://baltic.transparency-dashboard.eu/node/41

[16] "Data downloads | Nord Pool." https://www.nordpoolgroup.com/en/Market-data1/data-downloads/historical-market-data2/

Event Pictures

The REHVA Community of Young Professionals brings together participants from past editions of the student competitions to share knowledge and best-practices .

This Book of Papers aims at concentrating the knowledge of each edition of the competition and serve as a way to commemorate the occasion.

REHVA warmly thanks all the people involved in the organisation and participation to the event.

Join the discussion on the @RCYP Linkedin group!